



Doctoral Dissertation
Doctoral Program in Energy Engineering (30th Cycle)

# Development of innovative TCT saw blades for high speed cutting of metallic alloys

**Federico Simone Gobber**

* * * * * *

**Supervisor**
Prof. Mario Rosso

**Doctoral Examination Committee:**
Prof. Emanuela Cerri, Referee, Università degli Studi di Parma
Prof. Gian Luca Garagnani, Referee, Università degli Studi di Ferrara
Prof. Daniele Ugues, Politecnico di Torino
Prof. Sara Biamino, Politecnico di Torino
Prof. Nora Lecis, Politecnico di Milano

Politecnico di Torino

I hereby declare that, the contents and organisation of this dissertation constitute my own original work and does not compromise in any way the rights of third parties, including those relating to the security of personal data.

…….....

Federico Simone Gobber

Turin, 25 July 2018

# Summary

The subject covered in this thesis concerns the development of an innovative PVD coated multipoint cutting tool with cemented carbide brazed inserts for high-speed cutting of ferrous alloys. The aim of the research was to optimize the properties of the constituent materials in order to maximize their durability and provide a constant level of surface finishing of the machined parts. Fast cutting technologies are nowadays spreading because of the high productive rate that they guarantee, but on the other side wear is more severe with high speed cutting. Tungsten Carbide Tipped (TCT) saw blades are typically used in wood cutting but since 30 years are gradually taking the place of traditional band saws due to the higher cutting speed that are possible to reach and thanks to a better surface finishing on machined surfaces. The research work that was part of an industrial project was divided into three steps:

1. characterization of cemented carbide grades for application in machining
2. optimization of the cutting geometry
3. development of a tailored CAE – PVD coating.

The first part of the research work involved the study of literature in order to define the most suitable grades of cemented carbide for experimentation and to define some possible coating composition and architectures. Both plain grades and mixed grades with secondary Ti and Ta carbides were chosen, the relations among hardness, toughness, grain size and wear resistance were investigated through microstructural and mechanical characterization; finally discs made of cemented carbide were tested against pins of steel to characterize the resistance to sliding wear. From this characterization a mixed grade cemented carbide with 12% cobalt binder and micrometric grain size was chosen due to the best toughness properties

shown from characterization. Saw blades work under interrupted cutting conditions so toughness was required as the most important feature. In the second part of this study the cutting geometry of the cemented carbide inserts was optimized via experimental cutting tests and CAE methods. After a set of benchmark cutting tests on an industrial sawing station, the experimental cutting forces were calculated analytically and than used to calibrate a FEM 2D numerical calculation model. Two cutting geometries were then tested among those simulated: -15° and -25° rake angles. Thanks to the use of an hard metal with increased toughness ($K_{IC}$> 15 MPa), a tool with a rake angle of -15 ° has been designed to guarantee lower cutting forces (less than 90 N in the first cuts), friction and temperature on the surface of the tool's rake face. By experimental validation of the simulated geometries the cutting model gained predictive power. In the second phase of the work, three CAE - PVD coatings of the Al - Ti - Cr - N system were studied. Two of them were monolayer and one multilayer. The aim of this part of the work was to investigate the mechanical and microstructural properties of the analyzed coatings using different experimental methods to describe their behavior. The coatings were characterized not only from the mechanical point of view (hardness, toughness and adhesion) but also from the morphological (defective), and microstructural point of view. From the tests carried out, a multi-layered coating with improved toughness for use in interrupted cutting was designed.

# Contents

# List of Tables

# List of Figures

# Chapter 1

# Cutting tools and circular saw blades: materials and production

Sawing is a metal cutting procedure in which the multi-edged tool carries out both the cutting and the feed motions. The most essential function of the sawing methods is parting off or cutting off rods and profiles to length. Higher performances are requested to innovative cutting tools in terms of production rate and life. These targets are of paramount interest for many industrial fields and pass through the optimization of cutting geometries, the enhancement of materials and coatings. In the next chapters a literature – based description of the state of the art of cutting tools will be given in order to introduce the reasons for developing a new cutting tool for high speed cutting.

The tools are those parts of the processing machine that come into contact with the workpieces, therefore they must be very specific and therefore numerous and equipped with different shapes, in order to better respond to the different geometries, materials and efficiencies required. They are always equipped with at least one cutting edge, the sharp part intended to engrave the work piece.

Each tool has one or more cutting edges, each characterized by a particular geometric shape, identified by three fundamental angles whose sum is always 90 ° (Figure 1):

- Lower rake angle (usually known as relief) angle:

  It is the angle formed by the back of the cutting edge (main flank) with the machined surface of the piece. The values of the lower rake angle α are about 8 ° ÷ 10 ° for machining of soft materials, for which the friction is greater, and 3 ° ÷ 6 ° for the hard materials.
- Wedge angle β:

  is the angle formed by the rake and the main flank (back). The

penetration of the tool into the material is facilitated as the cutting angle becomes more acute. However, a sharp cutting edge is not very resistant and tends to deteriorate faster. The angle β varies from 40 ° for machining light alloys up to 84 ° for very hard cast iron.

- Upper rake (usually known as rake) angle γ:

  It is the angle formed by the face of the tool on which the chip (rake) flows with the plane passing through the cutting edge and normal to the machined surface of the piece. The angle γ can vary from very small values for the processing of very hard cast iron, to about 40 ° for light alloys but it can have negative values for the processing of even harder materials and / or the speed of very high processing.

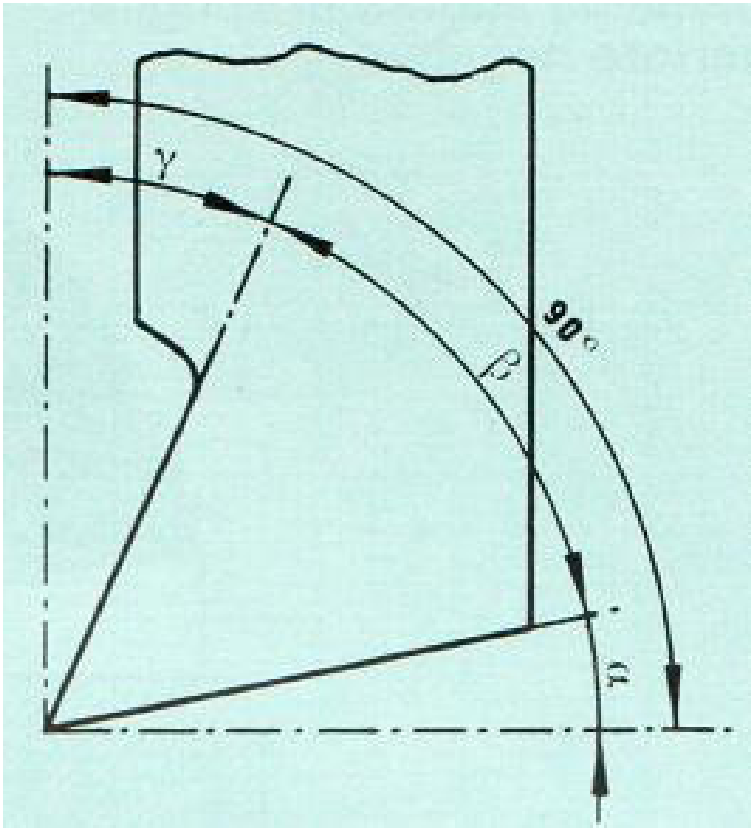


**Figure 1.** Characteristic cutting angles in a machining tool.

The main part of the cutting tool interested from this study is the blade insert, called tooth. With respect to conventional lathe/milling inserts the teeth are brased to a steel disc called “saw body” and not fixed to it mechanically. Despite the common thinking, a tungsten carbide tipped (TCT) saw blade is a complex tool composed of different materials (mainly steel for the body and hard metal for the teeth kept together by a brazing alloy). The production cycle of these cutting tools starts from the laser cutting stage where a cold rolled steel sheet usually made of high carbon steel (i.e. 75 Cr1, 80 CrV2). In this form the saw body has in its profile

the appropriate grooves for the subsequent brazing of the teeth already provided with the inserts in hard metal, produced by powder metallurgy.

**Figure 2.** Coated TCT sawblade for cutting metallic alloys.

The inserts are then placed in the appropriate grooves, arranged in the order of an alternating chip breaker and then brased-soldered by alloy with low-melting elements (49Ag 16Cu 23Zn 7.5Mn 4.5Ni). The use of this type of low temperature – melting alloys will inevitably influence the temperatures of subsequent treatments, above all the PVD coating which cannot exceed temperatures up to 300 – 350°C to avoid the evaporation of the zinc contained in the brazing alloy and the subsequent weakening of the brazing. The positioning and welding process is automated, but slight changes in the angles of positioning of the various teeth are inevitable, with respect to the radial direction of the blade. The subsequent sharpening process can bring back into tolerance the tool, and provides the distinctive sharpening geometry, different for each material to be machined. The inserts, in WC-Co cemented carbides, are characterized by an upper negative rake angle $\gamma$ which for ferrous alloys can vary between -15 and -30° depending on the application, and a lower rake angle $\alpha$ of 8 °.

Subsequent to the braze-welding process, a stress relieving heat treatment is performed on the blades, now equipped with inserts. The heat treatments at too high temperatures can lead to a reduction in the hardness of the blades, so compromise temperatures are chosen, always considering the production times.

When the circular saw blades operate at high rotation speeds, lateral vibrations can occur which are not negligible, which cause less precision in cutting, as well as risks for the safety of the operators that can be found around the sawing machine.

This happens because the natural frequencies of the blade decrease due to the compressive stress induced by the thermal stresses produced by the heat generated in the cut. This phenomenon must be prevented by increasing the natural frequencies of the blade with the introduction of residual traction stresses; this process called tensioning is accomplished by locally deforming the blade with a hammer (manual) or special rollers (automated) (1).
Tension improves lateral stiffness and dynamic stability of the blade.

The amount of tensioning depends on the blade size, on the operating conditions with a higher tension required for blades working at higher speeds. Uneven tensioning due to variations in the lateral stiffness that can create a parametric harmonic motion of the blade during processing, a variation in stiffness has the same effect as the application of a variable load over time. The leveling consists in smoothing the deviations from the geometrical planarity of the blade [ (2)]. Tensioning and leveling produce different theoretical tension states within the blade thickness as shown in Figure 3. While tensioning produces a symmetrical tension state with a non-zero average value in the thickness of the blade, the leveling originates antisymmetric tension states with a zero average value. Afterwards the blades are tensioned by a rolling process, carried out by machine but with a check carried out by a specialized technician at the end. Then "tensioning rings" are imprinted on the two planar faces of the blade body, one on each side, concentrically at its center. Depending on the distance from the center of the blade (ring radius), these rings lead to obtaining more "hard" or "soft" blades. This qualification is based on the measurement of the bending angles of the blade following the application of certain pressures on teeth, separated by specific distances. By this it becomes possible to make considerations on the oscillation of the blade and on its frequency of resonance when cutting. For the considered cutting operation, with a cutting speed of about 210 m / min, neutral, intermediate blades are preferred.

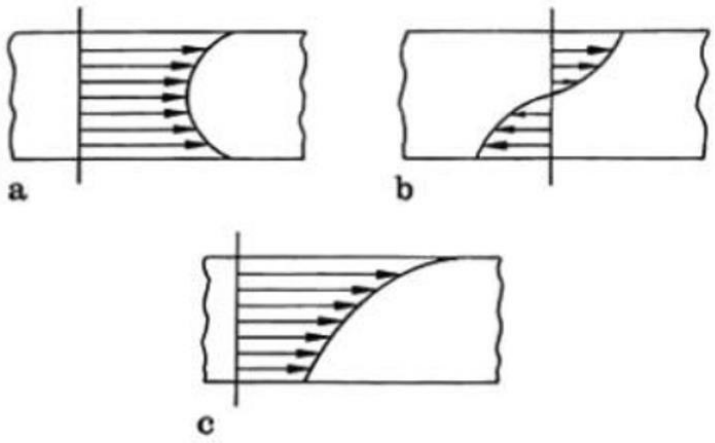


**Figure 3. Tension trends through the thickness of a circular blade, a) tensioning stresses, b) leveling efforts, c) superposition (a) + b)) of the two effects (2).**

The inserts are then sharpened and then, by brushing, subjected to the removal of burrs and to honing (rounding of the cutting edge down to approx. 20 µm). The softening process of the cutting edges is important because sharp cutting edges wear and degrade more quickly, due to the intense mechanical stress that would be

localized during processing and which would lead to fracture and crushing (3). After these operations cleaning and surface preparation are carried out for the subsequent coating, using electrolytic cleaning processes, ultrasonic treatments, rinsing and drying.

## 1.1 Machinability of metallic alloys and its assessment

Machinability is defined as the ease / difficulty with which a material can be processed under a set of defined conditions such as: cutting speed, material feed rate and depth of cut. It can also be described as the relationship of interaction between the material to be processed and the tool material in order to obtain an acceptable tool life and good surface finishes of the material to be processed. Some focal points to monitor the workability are: the forces exerted on the piece during processing and the shape of the chip produced by the cutting operations. The workability of a material is mainly controlled by parameters such as tool life, the forces developed during the cutting operation and the surface finish on the cut piece (4). The term machinability for machinability machines indicates the ease with which a material can be processed in order to obtain the desired size, shape and surface finish. It is described as the relationship of interaction between the material to be processed and the tool material in order to obtain an acceptable tool life and good surface finishes of the material to be processed. The machinability index, or the measure of the workability of the component, is defined as:

$$\text{Workability index (\%)} = \frac{\text{cutting speed to guarantee tool life of 20 min}}{\text{cutting speed with reference material for 20 min tool life}} * 100$$

The reference material is AISI 1112 which has a workability index of 100%, material with higher indexes will have better workability (AISI 1215, magnesium alloys, aluminum alloys), while those with an index lower than 100% will have minor workability (cast iron, stainless steels, AISI 4140 66%). However this is a relative measure and there are no universal or standard methods for its measurement. Historically, the measurement is done by evaluating the following factors:

- Tool life: measured by the amount of material removed from that particular cutting tool under fixed conditions before the cutting yield becomes unacceptable or the wear of the cutting edge has reached a predetermined value;
- Maximum cutting speed: i.e. the maximum cutting speed that the tool can tolerate, providing a good performance for a pre-established period of time;
- Power consumption: measured by the amount of energy needed to remove a unit volume of material under pre-set conditions

## 1.2 Chip formation mechanism

The removal of metal during the machining operations by chip removal takes place for a plastic deformation-cutting mechanism along a plane inclined with respect to the cutting direction.

More precisely, as the metal is deformed by the forced contact of the tool, the microvoids begin to form at the interface between the various microcostituents (example: edges of grain or particles) where there are incompatibility of deformation caused by the different orientation or nature of the interfaced constituents. The increase in deformation promotes the growth of micro-vats up to a critical value such that the damage caused to the crystal lattice is such as to give rise to a microstructural instability that causes the coalescence of microvoids, the formation of a microcrack and finally a fracture. The upper rake angle refers to the angle which is formed between the surface of the cutting edge which deforms the material to be machined and the normal with respect to the cutting plane. The mechanisms that lead to chip formation can be different depending on the material that has been machined

### 1.2.1 Fragile workpiece material

In the case of a fragile material, the tool, when it comes into contact with the work piece, creates a crack which will grow according to the mechanisms of the fragile fracture until it separates the material into two flaps, at this point of fundamental importance. cutting geometry; the best thing would be to have a cutting edge with a positive rake angle, but this is not advisable because given the high hardness of the material to be cut the end of the cutting edge would bear too high loads and would easily break. If the cutting edge had a rake angle of 0, the condition shown in Figure 4 at point A is obtained, obtaining an almost rectangular fragment and therefore having a regularity of the chip. If, on the other hand, the rake angle was negative as shown in Figure 4 point B (necessary for some materials given the high strain suffered by the cutting edge that could break), many fragments of material would be formed detached from the work surface.

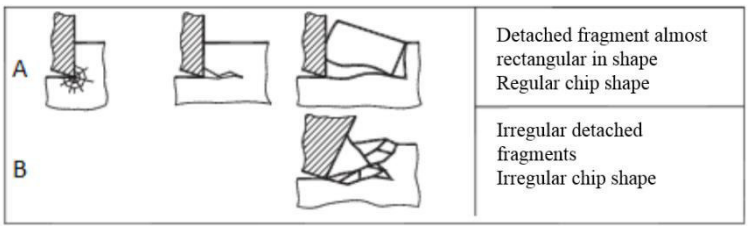


**Figure 4.** Schematization of chip formation in fragile materials **(4)**.

## 1.2.2 Ductile workpiece material

In a ductile material, using a tool with a neutral rake angle (Figure 5 point A), deformation lines will form in correspondence with active sliding planes that will give a continuous shape but with a jagged profile to the shavings. These lines are well spaced from each other and clearly visible. If the rake angle was positive (Figure 5 point B), the shavings formed will be continuous and the machine will have to give an almost constant force to work the piece.

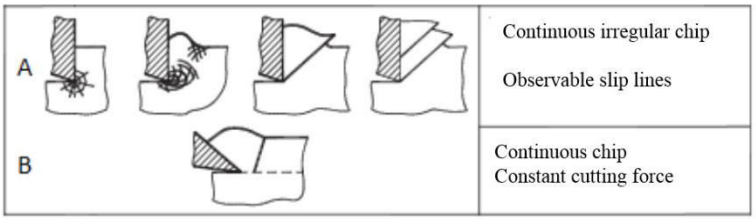


**Figure 5.** Schematization of chip formation in ductile materials **(4)**.

## 1.2.3 Soft workpiece material

Finally, if we had a very ductile material, we distinguish two cases: the first (Figure 6 point A) where we have a continuous but jagged chip shape with deformation lines not very spaced and therefore hardly distinguishable; In case B, a lot of heat is generated due to the high strain strains. The greater the heat generated, the greater the tendency of the chip to stick to the surface of the cutting edge; this phenomenon occurs when a force of adhesion is generated, between the chip in the formation phase and the cutting edge, greater than the force necessary for the plastic deformation of the material. If this happens, accumulation of the material near the cutting edge increases the torque necessary for cutting, when the torque has reached a value such that the area attached to the cutting edge is detached and can proceed with the normal shaping of the chip. Following this phenomenon one can see distinct ridges on the chip surface.

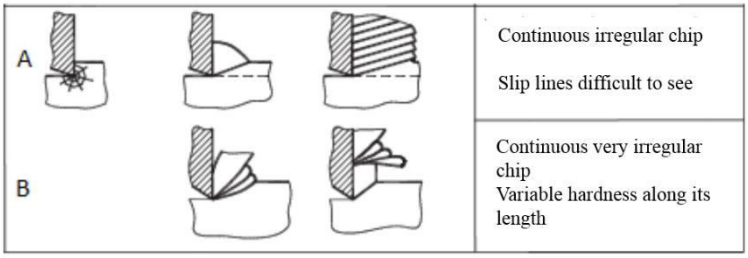


**Figure 6.** Schematization of chip formation in soft materials **(4)**.

## 1.3 Desired characteristics for cutting tools

Before introducing the materials used in the production of inserts for applications in machining tools, it is necessary to list some characteristics common to all the tools and which constitute a series of fundamental criteria for their evaluation.

- Cold hardness is guaranteed by the chemical composition of the material that constitutes the cutting edge and is further improved by subjecting the material to specific treatments.
- On the other hand, the hot hardness must be maintained once the operating temperature has been reached (temperature reached by the cutting edge for certain cutting speed and material rates).
- The property of resisting shocks and deforming under the application of a load is referred to toughness: this parameter becomes fundamental in multi - cutting tools such as drills, a category to which the cutting blades belong with a particular geometrical meaning (5), which undergo continuous shocks on the surface to be processed during machining. Hardness and toughness are properties that can be assumed in the first analysis as complementary, therefore the choice of material is always the result of a compromise.
- Resistance to wear and chemical inertia are two properties that influence tool life.
- An adequate thermal conductivity must facilitate the disposal of the heat produced in the cutting area in order to keep the temperature assumed by the cutting edge at acceptable values.
- The friction coefficient must be kept as low as possible between the tool and the material to be processed in order to contain the heating in the cutting area.

The effectiveness of a material in a cutting tool depends on the right combination of properties as maximizing only one often does not lead to a general improvement but to the depletion of other properties (eg materials with high resistance to wear are often not very tenacious). The properties of the material to be cut and the type of work to be done must influence the choice of the most suitable material. In the design of a cutting tool, the properties of toughness, resistance to thermal and plastic deformation and resistance to wear, crater formation and, in the case of coated inserts, the resistance to chipping are of primary importance. A detailed review of the properties required for cutting tools is described in (6).

Toughness machining means the resistance of the cutting edge of the tool to breakage under unfavorable conditions such as: high feed speed, high work interruption frequency, lack of rigidity. The interruption of work in a machining operation is to be understood as the fraction of time during which the tool does not work due to a discontinuity in the section of the piece, for example a tubular geometry is discontinuous because it alternates full and empty. Ultimately, an

interrupted or intermittent cut takes place when the tool is not in constant contact with the piece. These fluctuations affect both the thermal load and the tool that bears the mechanical load and can negatively affect the integrity of the cutting edge, productivity and process safety. It is necessary that under conditions where a discontinuous / interrupted cut is foreseen, the cutting material must be carefully chosen, in these cases toughness it is the parameter that can be a discrimine between a good working and the premature breaking of the tool (7).
In the metal-to-metal cutting, the use of high speed steel (HSS) blades is also not recommended, even after hardening surface treatments (eg nitriding). HSS blades are not suitable for cutting other metals as they are subject to wear from the early stages of machining.

When cutting very different alloys, it is not possible to standardize the geometry of the blades because wear occurs in a different manner for each class of material according to different mechanisms (8). On the basis of the machinability of the single material, the tools that best respond to the workability characteristics of the material and which are more resistant to wear phenomena must be chosen.

## 1.4 Materials for cutting tools

The so-called hard metals are used to make tools for machining metal removal (turning, milling, drilling) or for any other process in which a material of high hardness is required (cutting, crushing, etc.). Carbide tools are harder than HSS (up to $HV_{10}$ 2200 compared to $HV_{10}$ 1000) and withstand higher cutting temperatures (1000°C compared to 600°C) allowing higher machining speeds. A disadvantage of the carbide is toughness, lower than that for HSS (Figure 7).

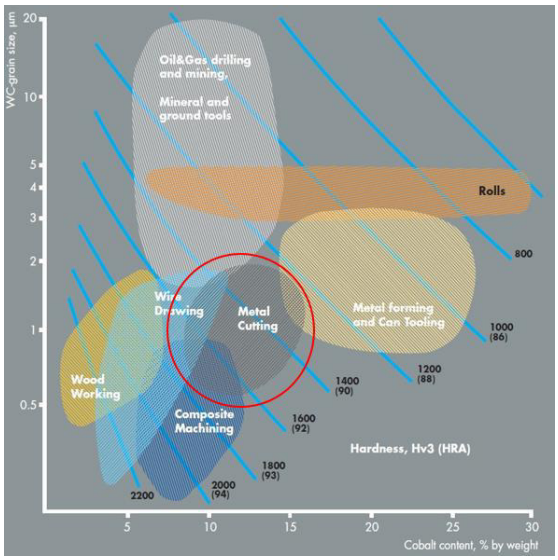


**Figure 7.** Relationship between carbide grain size and % binder for some cemented carbide grades of spread use **(9)**.

In cutting steel and metal alloys, tools with cemented carbide inserts are used, this consists of hard particles, such as tungsten carbide (WC), embedded in a metal matrix: such materials are commonly called cemented carbides or carbide. Sub-micrometer carbides are used in the processing of stainless steels and high strength nickel alloys (10). The percentage of hard phase (carbide) and binder (cobalt alloy) is dependent on the performance and characteristics that the tool must meet. Most of the abrasive materials used are tailored to the particular application; for example the binder content can vary from 4 to 25% by weight and the hardness consequently from 2200 to 1000 $HV_{10}$. The binder may be different from cobalt alone; in fact, nickel and chromium were added to the cobalt alloys for tools that work in conditions where corrosion resistance is required. The microstructure of the inserts is an important parameter in the control of blade wear, controlled microstructures and finer-sized carbides give better mechanical properties as can be seen from a first analysis in (Figure 8).

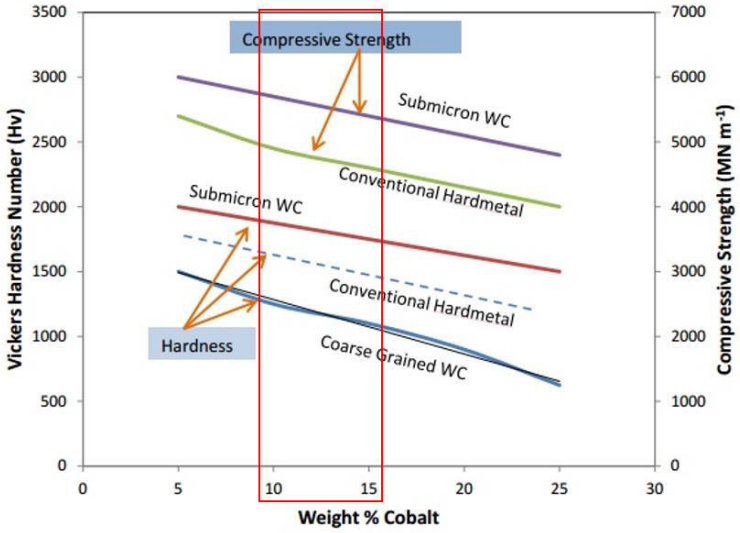


**Figure 8.** Strength and hardness as a function of binder fraction for plain carbides grades with fine or coarse grain size **(11)**.

The red square in Figure 8 represents the interval of binder content more suitable, of common use for cutting tools as observed in Figure 7.

## 1.4.1 Cemented Carbides

Cemented carbide inserts are very common in machining: the carbide inserts on steel blade bodies are also used for cutting blades. Carbides can be coated to increase blade life from the point of view of tool life. The ISO 513: 2012 standard (Table 1) names carbide families and outlines their preferential use based on the mechanical characteristics of resistance to wear and toughness.

**Table 1.** Designation of carbide grades according to ISO 513: 2012 and widespread uses.

| ISO Grade | Use |
|---|---|
| P | All kind of steels except for stainless steels |
| M | Specifically indicated for austenitic, austenitic - ferritic stainless steels |
| K | Cast iron |
| N | Non ferrous alloys |
| S | Special alloys for high temperatures based on iron, nickel, cobalt, titanium and titanium alloys |
| H | Hard metals |

The standard indicates with letters the classes of carbides according to specific compositional limits while with numbers (from 0 to 50) the degree of toughness / hardness is indicated. High numbers correspond to greater toughness, while lower numbers correspond to greater hardness.

The inserts containing tungsten carbide show a ten times longer life and a productivity 2 - 3 times greater than fast steel tools [9]. The production of cemented carbides passes through pressing and sintering of tungsten carbide powders or mixed carbides with a metal binder (cobalt), the possible presence of other carbides (VC, Cr3C2) contributes to the inhibition of the growth of crystalline grains . Isostatic sintering with liquid phase is an established production process that allows to reach densities close to the theoretical ones by operating at very high temperatures (up to 1900 ° C). Commercially available carbides with grains of different sizes, from sub-micrometric ones (d <0.2 μm) up to more coarse sizes (d> 6.0 μm). Increasing the carbide fraction allows to achieve greater hardness but negatively affecting the toughness. Decreasing the carbide size allows to obtain inserts that are more compact and therefore harder and more resistant to abrasion.

Grades with a binding content between 3 and 10% by weight and d <1 μm have higher hardness and compressive strength values in combination with high wear resistance and good toughness. These grades are used in a wide class of working on metallic materials. As the grain size increases, the toughness of the produced inserts increases, the variation in hardness is inversely proportional to the grain size and the metal binder fraction.

A sintered characterized by reduced carbide grain size and low binder fraction has compressive strengths of up to 7000 MPa. At temperatures above 600 ° C there is an impoverishment of the mechanical properties. A solution is to introduce a fraction of carbides which form a cubic phase with a centered body (TiC, (Ta, Nb) C) and guarantee greater hardness and resistance to high temperatures. A common goal in sintering is to modify the surface layers of the hard metal in order to obtain layers free of enriched cubic carbides instead of binder (cobalt) (12). Mixed carbides have a higher hardness than the WC alone, resistance to higher wear but also lower toughness in some compositions.

The different WC powders used, the composition and amount of metal binder and the amount and type of crystalline grain growth inhibitor are the factors responsible for the variety of degrees available and normed (Figure 3).

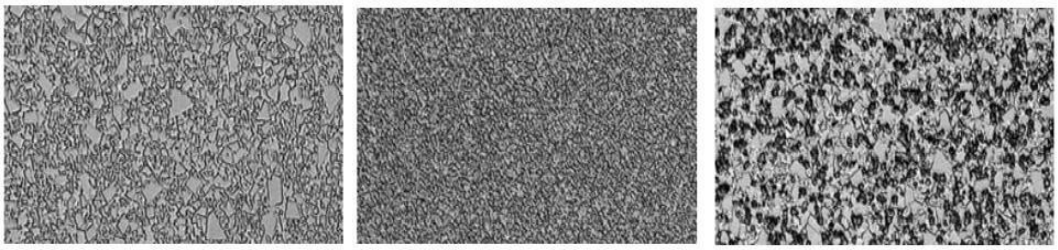

**Figure 9.** Plain carbides, submicrometric and containing cubic phases, according to ISO standards.

The grades can be divided into three broad categories: pure cemented carbides, that is, consisting only of WC and binder (Co), cemented carbides characterized by micrometric grain size in which grain refiners (VC or $Cr_3C_2$) are dispersed to reach smaller sizes at the micron and finally bound cemented carbides in which there are other carbides (TiC, TaC and NbC) which form a third phase, a cubic with a centered body, characterized by greater hardness. Another advantage of the so - called nano - grain carbides is that it can produce inserts for tools which, once sharpened, give a finer cutting edge, also improving adhesion with a possible coating (13). Titanium carbide in particular reduces the tendency of the WC to spread on the surface of the steel chips while tantalum and niobium carbides improve the mechanical resistance, the resistance to thermal shocks and also improve the hot hardness (14). The addition of TaC and TiC is not always effective in increasing wear resistance, the percentage of carbides must be controlled. In pin on disk tests on AISI 304 austenitic stainless steel (15) the addition of 1% of cemented carbide TaC (6% Co) proved to be more effective in limiting the size of the particles during sintering and increasing the resistance to wear compared to inserts containing both TiC and TaC.

With reference to Table 2, which shows the general characteristics of cemented carbides regulated according to ISO 513: 2012, three categories of carbides are examined: K, P and G.

- The carbides K 10 and K20 have up to 94% WC in weight and the remaining 6% of binder (Co), this allows to reach hardness up to 1600 HV 30 which makes them suitable for working very hard materials such as tool steels and steels that give short chips, nickel alloys, cobalt and titanium.
- P 25 and 40 carbides have up to 72.5 wt% WC and up to 17.5% titanium carbides and tantalum (TiC TaC) which lead to hardness values up to 1450 HV 30. This gives a less resistance to wear but greater toughness to work non-alloy or cast iron steels, at high speeds and up to high temperatures.

- Carbides G 10 and 60 have quantities of cobalt between 9% and 25% which results in greater toughness and lower resistance to wear, this grade of carbides is indicated in the processing of molds, punches and components that work in conditions of high wear.

**Table 2.** Main features of the classes of cemented carbides containing WC.

| Class of cemented carbide | ISO grade | Hardness [HRA] | Grain size [µm] | Co binder [% wt] | Carbides fraction [% wt] | Use |
|---|---|---|---|---|---|---|
| | | | | | | |
| **Plain** | K, N, S, H | 89 – 93.5 | 1 – 8 | 3 – 12 | TiC (0.1 – 1), (Ta,Nb)C (0.3 – 1) | Milling of ferrous alloys |
| **Micrometric** | M, N, S | 92 – 93 | < 1 | 6 – 15 | VC (0.2 – 0.3), $Cr_3C_2$ (0.3 – 0.5) | Drilling heat resistant alloys, Milling of titanium alloys |
| **Mixed** | P | 91 – 94 | 0.8 – 2.0 | 5 - 10 | TiC (4 – 25) (Ta,Nb)C (max. 25 %) | Milling of high strength steels |

## 1.4.2 Production route and main characteristics of cemented carbides

Cemented tungsten carbides offer excellent wear resistance thanks to the combination of hard WC particles with a tough matrix, which makes cemented tungsten carbides one of the first and most effective products from powder metallurgy. These hard metals are used in various applications where resistance to wear is very important, such as nozzles for sandblasting and spraying, seals for slurry pumps and components for the oil industry. In the hard metals, the wear properties are the most interesting mechanical properties. The production of hard metals WC-Co occurs purely through liquid phase sintering. The high solubility of the WC in cobalt at high temperatures and the excellent wettability of the WC by liquid cobalt leads to the achievement of excellent densification during the sintering process in liquid phase, leading to the production of structures with low porosity (16). The cemented carbides are therefore characterized by high hardness, toughness and resistance. The production process consists of five main phases:

1. Production of powders;

2. Grinding;
3. Pressing;
4. Pre-sintering;
5. Sintering.

Various techniques for processing tungsten carbide powders are available. These include the traditional method based on the production of tungsten carbide powders by reduction through tungsten oxide hydrogen, followed by carburization. It is also possible to directly perform the carburization of tungsten oxides. The spray production process, on the other hand, makes it possible to obtain WC-Co powders in situ (16). The grinding of the powders is carried out to obtain a more homogeneous dispersion of the tungsten carbide powders in those of cobalt. In this process the dimensions of tungsten particles are normally reduced and the stress induced in the particles leads to a simplification of the sintering process. During milling, cobalt can go against a phase transformation, going from a strictly cubic structure to a compact hexagonal, therefore a lubricant is used, during the mixing of the powders, mainly to reduce the friction between the mixtures of powders and tool surfaces and minimize breakdown trends. The ground powders are then pressed into a mold using rigid steel or carbide molds, with a pressure of 150-990 MPa. The components can be pressed directly into specific shapes or in large blocks that will be subsequently formed. Following the pressing process, the composite is pre-sintered in hydrogen, with increasing temperature up to 800 ° C. Hydrogen reduces the amount of oxygen absorbed and the oxides on the surface of the particles. When a cooled compacted product is sufficiently coherent, it allows a subsequent molding since it is less prone to damage. Subsequently, the sintering treatment is carried out, normally conducted at temperatures between 1350 ° C and 1550 ° C.

The rounded shape of the tungsten carbide in the initial stages of the sintering process leads to the faceted morphology that will give the characteristic flat trigonal prism shape of the WC grains (16).

Cobalt is widely used as a binder, due to its excellent wettability and adhesion properties with carbides. The capillary action of cobalt during sintering makes it possible to obtain high densities. Cobalt exists in two allotropic forms, the compact hexagonal that is stable below 417 ° C and the centered cubic that is stable up to 1495 ° C (cobalt melting temperature). In any case, a significant amount of FCC cobalt is present in the sintered WC-Co hard metals even at room temperature. The transformation between the two phases is of a martensitic nature and is influenced by the quantity of dissolved tungsten carbide and the free medium path in the binder, ie the average distance between the surfaces of two adjacent carbide grains.

A high concentration of tungsten and carbon in the binder has led to an increase in the temperature at which the martensitic transformation takes place, from 417 ° C up to about 750 ° C (16). This prevents the formation of fragile hexagonal compact phase at low temperatures. Hard metals with a finer microstructure have a higher FCC / HCP ratio than conventional values, due to the higher tungsten concentration in the binding phase. Tungsten is combined with carbon to form two carbides, WC, which has a maximum microhardness of 24 GPa and W2C with a

microhardness of 30 GPa. The pure WC does not melt under standard atmospheric conditions, but decomposes into a liquid and graphite phase at temperatures above 2780 ° C as observed in the WC phase diagram in Figure 10.

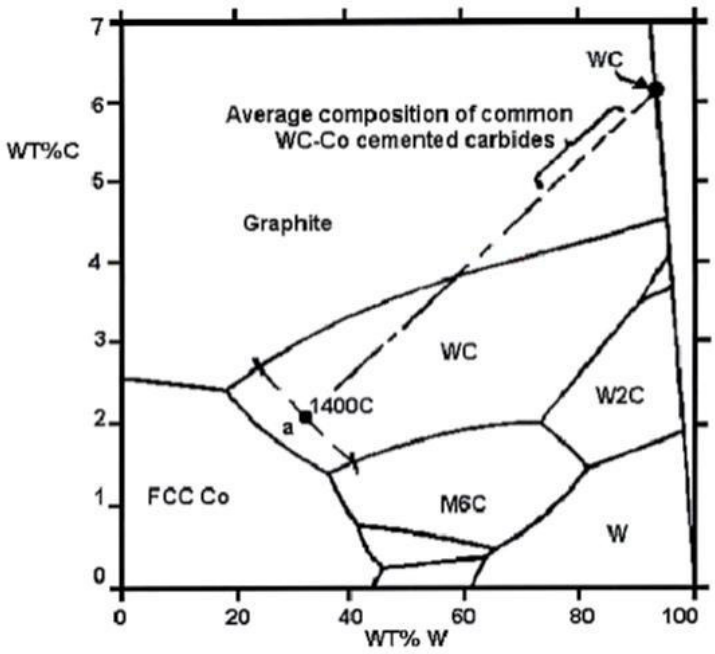


**Figure 10.** Pseudoeutectic W – C phase diagram **(17)**.

The major phase in cemented carbides is the WC monocarbon phase, characterized by a hexagonal crystalline structure with two atoms per unit cell and a c / a ratio of 0.976 (Figure 11).

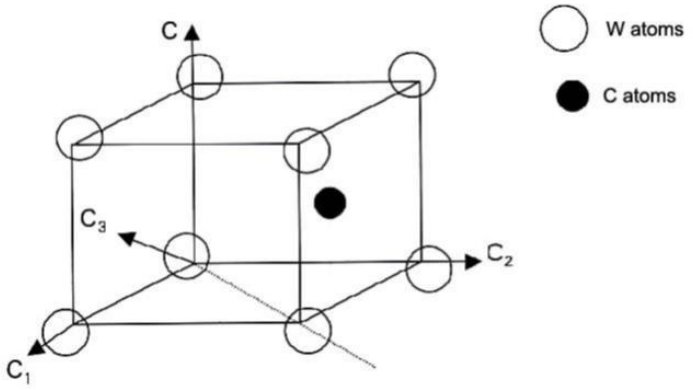


**Figure 11.** HCP crystal structure of WC **(18).**

## 1.4.3 Contribution of secondary carbides to cemented carbides wear resistance properties

Sliding wear is one of the most relevant aspects for tools used in the manufacturing industry processes, for example in finishing, cutting, drilling and drawing operations. In these processes the degradation of the instrument is attributable overall to wear. Material properties such as hardness, composition and microstructure, and working conditions (dry or lubricated conditions) affect wear

behaviour. Cemented carbides are typically used in these applications for their excellent combination of high hardness and moderate toughness. The wear resistance of WC-Co alloys is, in general, dependent on the carbide – binder ratio, carbide grain size and bulk hardness. An increase in the size of the grain leads to a lower hardness of the material but to a better resistance to wear with equal quantities of binder (Cobalt). Wear resistance is proportional to the ratio between grain size and quantity of binder. From the study conducted by Jia and Fischer the best results were obtained for larger grain size and binder reduction rather than increased hardness due to grain size reduction (19). It has been shown that the properties of the WC-Co carbide can be improved by the addition of refractory carbides such as tantalum (Ta), molybdenum (Mo), cadmium (Cd), titanium (Ti), vanadium (V) and niobium (Nb).

Sliding wear of cemented WC-Co carbides has been studied by many authors while the study of friction of these materials has aroused less interest. The majority of publications focused on the qualities of WC-Co with carbide sizes between medium and coarse (micrometric dimensions), with rather limited focus on the effects that the addition of different carbides lead to friction and wear resistance of the hard metal. (20) tested the mutual wear of hard metals, with binder percentages ranging from 6 to 12% by weight and with grains varying in size between 0.6 and 2.2 μm. Friction and wear have proved to be a function of applied loads and oscillation speed. Titanium carbide is harder than tungsten carbide and therefore cemented carbides with TiC addition tend to have a higher abrasion resistance than WC-Co composites that do not. TiC titanium carbide is also known to reduce the tendency to weld between the tool tip and the processed fragments. Cemented carbides WC-TiC-Co showed a high hardness at high temperatures, an excellent feature considering the high temperatures that reach the tools during the working processes (even 800 ° C at the point of contact) (15). TaC tantalum carbide has been shown to be an effective grain growth inhibitor and capable of increasing fracture toughness (15),
it was found that the WC-Co added with less than 1% by weight of TaC, turned out to be the most effective in increasing the resistance to wear by sliding, in all tested conditions. This result is mainly attributable to the high hardness, although the oxide formation may be relevant in varying the results, for higher loads. The combined addition of TiC and TaC instead does not significantly improve the wear resistance of the material, if in excessive quantities. Excessive amounts of TaC lead it to lose effectiveness as a grain growth inhibitor. Excessive dimensions of tungsten carbides and TiC make the material more sensitive to fracture and material removal. In the tests carried out in their study it was also observed that stainless steel showed a higher wear rate than mild steel against all the qualities of cemented carbides considered, although it had greater hardness, due to the lack of formation of oxide on the surface of wear.

## 1.4.4 Alternative materials

The tools used for cutting and machining steel and super alloys must have adequate hot hardness to withstand the temperatures generated by high processing speeds. The high speed machining of super nickel-based alloys is carried out with coated carbide tools, other materials have been developed: ceramic, cubic boron nitride (CBN) or polycrystalline nitride (PCBN), while uncoated carbides are used when the speeds processing are low. The use of carbides of sub - micrometric size is growing at a constant speed in all applications where high resistance to abrasion and mechanical resistance are required. The impact resistance of these alloys, however, is limited but the development of new powders has been successful and it is natural to expect significant production increases in the immediate future. Another rock is linked to the consolidation of compact at high temperatures, different treatments have been studied such as the use of wheat growth inhibitors or the use of different compaction technologies to maintain the nanometric size. While some studies have been successful in presenting techniques for compacting cemented carbide with grains in nanometric size, an industrial aspect of these techniques has not yet been consolidated (11). Tools that use CBN and ceramic inserts are an emerging technology in chip removal processes compared to more traditional materials; for reasons of costs, materials with lower properties are still preferred but designed to work in acceptable intermediate conditions.

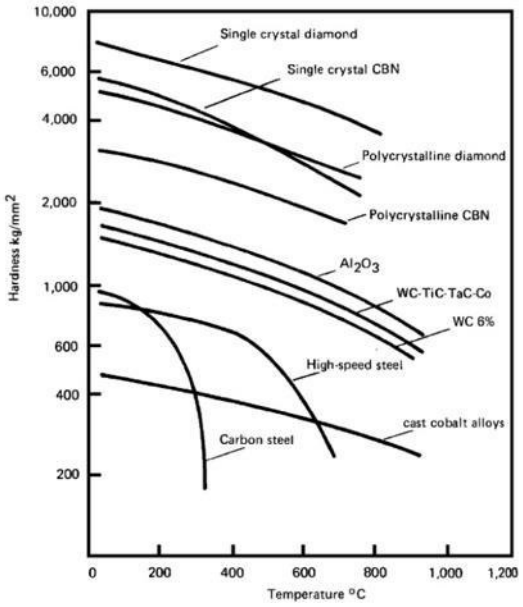


**Figure 12**. Hardness values when temperature changes for some materials used in the processing of super alloys **(21).**

Carbides coated with multilayer coatings (TiN / TiCN / Al2O3 / TiN) are a solution also adopted for lower costs. Coatings based on titanium-containing compounds are used because they have higher resistance to wear and high speed cutting properties. Feasibility studies on the use of carbides with multilayer coatings (22), (23) have shown that in turning operations, a multilayer coating can be effective (TiN / TiCN / Al2O3 / TiN) and can be adopted for industrial production processes. The trend in the future (24) will be that, mainly economic and then toxic,

to replace cobalt in favor of alloys iron - nickel, iron - chromium - nickel, nickel aluminides or iron aluminides in the role of binding agent hard metal.

# 1.5 Cemented carbides mechanical properties

## 1.5.1 Fracture toughness

Wear resistance is certainly the most important property for cutting tools, nevertheless some relevant breakage are due to low fracture toughness, especially in interrupted cutting applications where toughness is highly required due to the continuous contact/non – contact regime, causing a cyclic sequence of mechanical loading/unloading.

Fracture toughness indicates the resistance of a material to the propagation of a crack. Fracture toughness is measured by the critical intensity factor $K_{IC}$. The $K_{IC}$ value is calculated using the equation below (25). Where H is the hardness of the material, F is the indentation load and the length of each of the Palmqvist cracks. When all quantities are expressed according to SI units (International System) constant A assumes the value 0.2784.

$$K_{IC} = A\sqrt{\frac{HF}{\sum_i a_i}}$$

A toughness / hardness chart shows the relationship between the two quantities: the toughness decreases with increasing hardness (Figure 13). Fracture toughness and hard metal hardness vary differently with the composition and / or microstructure of the material. In literature there are disagreements about what kind of relationship exists between these properties.

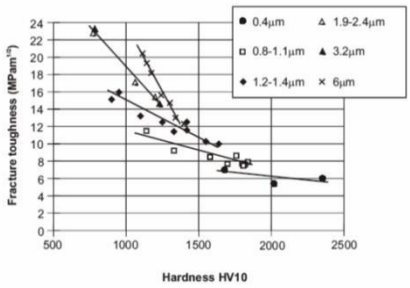


**Figure 13.** Fracture toughness with varying hardness of hard metal WC-Co with different grain sizes and binder percentages **(26)**.

Roebuck and Almond have found that if the volume fraction of cobalt and the size of the WC grains are reduced then the fracture toughness tends to the limit value of 7 MPa m1 / 2, more recent studies on very fine hard metals confirm this trend (27). These results suggest that further refinement of the WC grain size would lead to a further increase in hardness without any sacrifice in terms of carbide fracture toughness.

## 1.5.2 Mechanical strength

Cemented carbides have high compressive strength, much greater than those of most other materials. Typical values of compressive strength range from 3.5 to 7.0 GPa (28). These materials have low ductility at room temperature so that the little difference exists between their yield strength and fracture strength. At highertemperatures the ductility increases slightly. The yield stress decreases monotonically with increasing temperature and the fine-grained carbides tend to lose their yield strength much more rapidly than the coarser grades. However at room temperature the fine-grained carbides exhibit a high yield strength.

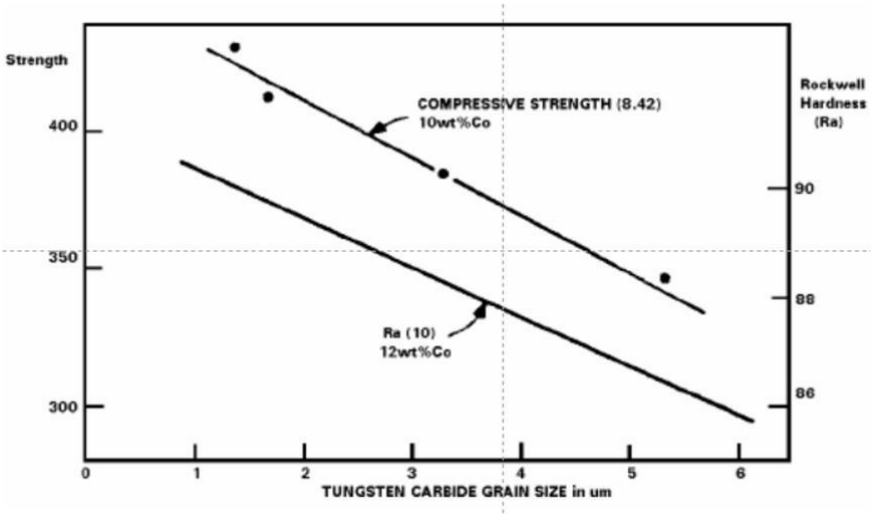


**Figure 14.** Effect of WC grain size on hardness and compressive strength of WC-Co hardmetals **(29)**.

## 1.5.3 Effect of carbide grain size

The transverse rupture strength (TRS) is a three-point flexure test used to measure the strength of sintered materials and is commonly used in the testing of WC-Co hardmetals. Work by Exner showed that the WC grain size has an influence on the TRS of WC-Co hardmetals. In his work a maximum TRS at a WC grain size of 3 μm was reported (29) (Figure 15).

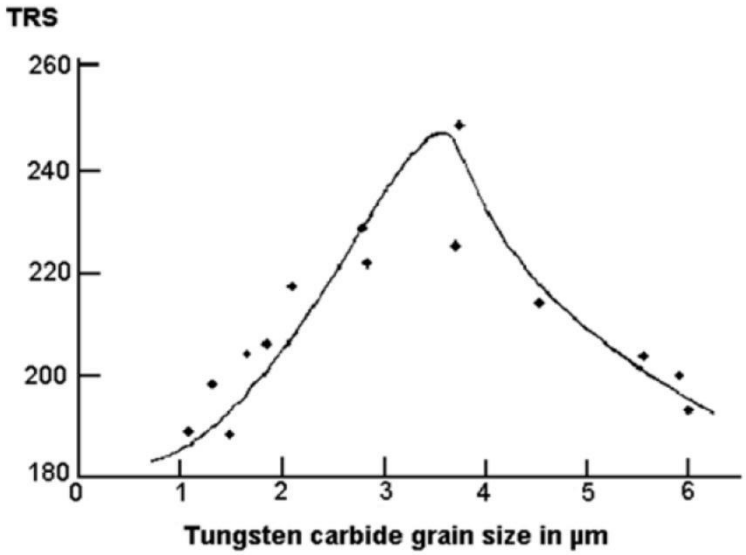


**Figure 15.** Influence of WC grain size on the transverse rupture strength of WC-6Co hardmetals **(29)**

## 1.5.4 Binder mean free path

The binder mean free path is dependent on both the cobalt content and the WC particle size and can be used to describe the distance moved by a dislocation when the binder is free of precipitates. The transverse rupture strength exhibits a maximum when plotted against the binder mean free path. The maximum is a transition point from predominantly brittle to predominantly ductile failure. When the binder mean free path is low the strength is controlled by the fracture toughness and therefore increases with increasing binder mean free path. When the binder mean free path reaches higher values the hardmetal yields before failure and the strength is mainly controlled by the yield strength of the hardmetal, which decreases with increasing binder mean free path.

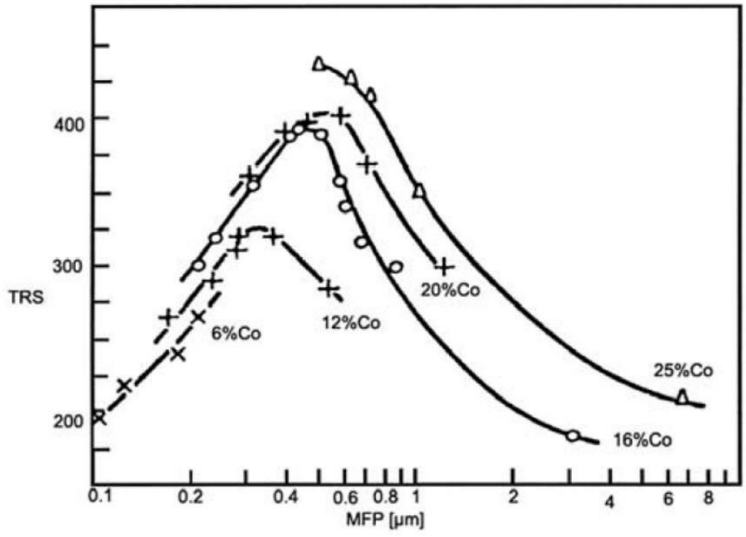


**Figure 16.** The influence of the binder mean free path on the strength of WC-Co cemented carbides **(29).**

## 1.5.5 Contiguity

It is difficult to determine the effect of contiguity on the mechanical properties due to other microstructural characteristics that must be taken into consideration. However, the limited work that has been carried out shows increasing hardness with increasing contiguity (30).

## 1.5.6 Wear behavior of cemented carbides

All mechanical properties presented have a direct influence on wear behavior and on the different mechanisms that influence wear behavior of cemented carbides, in the next few paragraphs the main wear processes will be discussed with relation to cemented carbides. Deformation and wear in cemented carbides are strictly related, thus in the first part of the chapter an introduction to deformation and fracture mechanisms will be presented.

### *1.5.6.1 Crack propagation in WC-Co alloys*

Four types of fracture paths can be distinguished in WC-Co hard metals:

- C transgranular fracture through the carbide crystals
- C/C along carbide grain boundaries
- B transgranular through the binder phase (Co)
- B/C along binder/carbide boundaries

Fracture paths B and B/C are formed by the nucleation and coalescence of voids in the binder phase. The voids are formed by the hydrostatic stress that develops in the ligament as the binder is stretched without debonding from the WC grains (31). The work of fracture along the binder/carbide interfaces is smaller than for transgranular fracture through the binder. Carbide fracture normally precedes binder fracture and determines the direction and type of path the crack takes. However the main contribution to fracture energy comes from path B. The crack normally initiates in the brittle WC phase and avoids the ductile binder which forms ligaments attatched to the WC grains. As the crack continues to open each ligament is stretched until it ruptures. At this point the crack tip in the matrix has moved further ahead. The local geometry of the microstructure determines whether the crack advances along a B or B/C type path. The plastic deformation of the binder is constrained when the surrounding WC skeleton is intact. When the carbide next to the binder region cracks, localised deformation of the binder begins under plastic strain. As the ligament is stretched its lateral contraction is impeded by its continuity with the carbide and pore-like crack blunting and/or the formation of voids inside the ligament occurs.

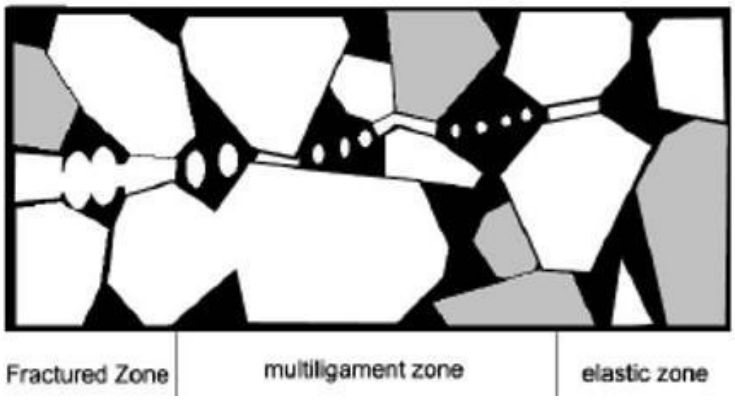


**Figure 17.** Schematic of the crack tip region in WC-Co during deformation. The black region represents the binder phase, and the grey regions represent the WC grains. The white region is the area where WC grain fall-out has occurred **(31)**.

Crack paths B and B/C both lead to the formation of ligaments and voids in the binder phase. The main difference is that the plastic deformation when the crack runs parallel to the carbide/binder interface is reduced. Path B/C is therefore more energetically favourable and is observed as long as the angle between the crack and the interface does not exceed a critical value, which has been found to be about 25°. When this value is exceeded the crack is forced to travel through the centre of the binder region (31).

### *1.5.6.2 Sliding wear behavior*

Sliding wear occurs when two solid surfaces slide against each other and is similar to abrasive wear in that they both require relative motion between two surfaces. Sliding wear is more of a surface phenomenon which makes it difficult to predict the friction and wear behaviour from bulk properties. The mechanical properties of hexagonal materials are very anisotropic and this further complicates the wear behaviour of WC-Co hard metals. Sliding wear is not a stable mechanism, during the course of wear the contact surface changes and heat is produced because of friction and this affects the wear rate. Pirso et al. carried out sliding wear tests on WC-Co hardmetals (12) During the initial stage of sliding wear no material detachment was observed for the WC-6 wt% Co and the WC grains became glossy and polished. Carbide grain fall-out was first observed after some distance had been covered, i.e. more than 1 km of sliding distance.

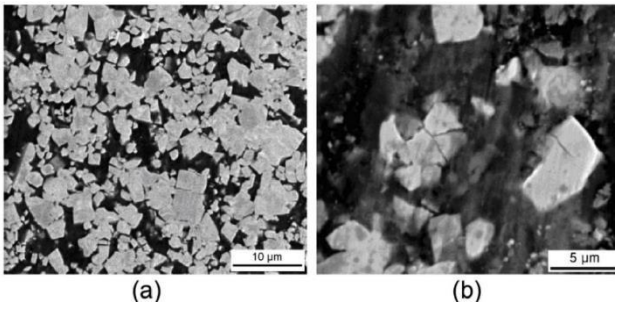


**Figure 18.** Worn surface of WC-20 wt.% Co (a) WC grain size of 1.3 µm and (b) WC grain size of 1.5 µm, after 8 km run at load of 180 N **(12)**.

In tests against a silicon nitride ball, WC-Co hard metal discs show an increasing wear resistance with increasing hardness. The wear mechanisms have been found to occur on a smaller scale than the individual WC grains. During sliding wear the wear debriss are not easily removed and can therefore accumulate on the surface during testing and form a tribofilm or mechanically mixed layer. The tribofilm has different properties from the original material and may therefore influence the subsequent wear behaviour. Tribofilm formation has been observed by Engqvist et al. on the cemented carbides after dry sliding wear (32). It has been suggested that small WC fragments mixed with Co binder increase the surface toughness of the cemented carbide and therefore also affect the wear resistance. Cemented carbides have a high wear resistance in sliding contact, especially at high normal loads. The wear mechanisms are best explained when the individual phases are considered separately. The fragmentation of WC into small wear debriss is also important for the relief of stresses in the material. These two features and the high fracture toughness of the composite accounts for its ability to endure high pressures without entering into a high wear regime.

A friction coefficient between 0.3 and 0.5 has been reported for cemented carbides and the effect of the microstructure on the friction coefficient is still not clear (33). Binderless carbides exhibit a high resistance to microfracturing and have similar wear rates to cemented carbides containing a metallic binder phase.

The main wear mechanisms observed have been the fragmentation of WC grains and the oxidation of the fragments. It was suggested that the binder is initially squeezed out of the surface by compressive stresses in front of and on the sides of the indenter.

Cobalt extrusion is followed by cracking of the WC grains. This is followed by the microfracture of WC grains adjacent to the surface defects, which occurs due to load concentrations around the defect and reduced resistance to fracture as a result of binder flow and extrusion. WC fragments are removed and cobalt smears on the surface of the hard metal. The cobalt on the surface is expected to act as a lubricant which could reduce wear. Jia and Fischer carried out sliding wear tests on WC-Co hard metals with WC grain size ranging from 1.5 to 0.9 μm (34). The tests were conducted using a pin-on-disk tribometer without lubricant. The volume loss in all the samples increased linearly with sliding distance. The wear rate was found to increase with decreasing material hardness. The samples with 6 wt% cobalt exhibited a rapid decrease in the friction coefficient with increasing WC grain size and a similar but less pronounced dependence was observed for the softer materials

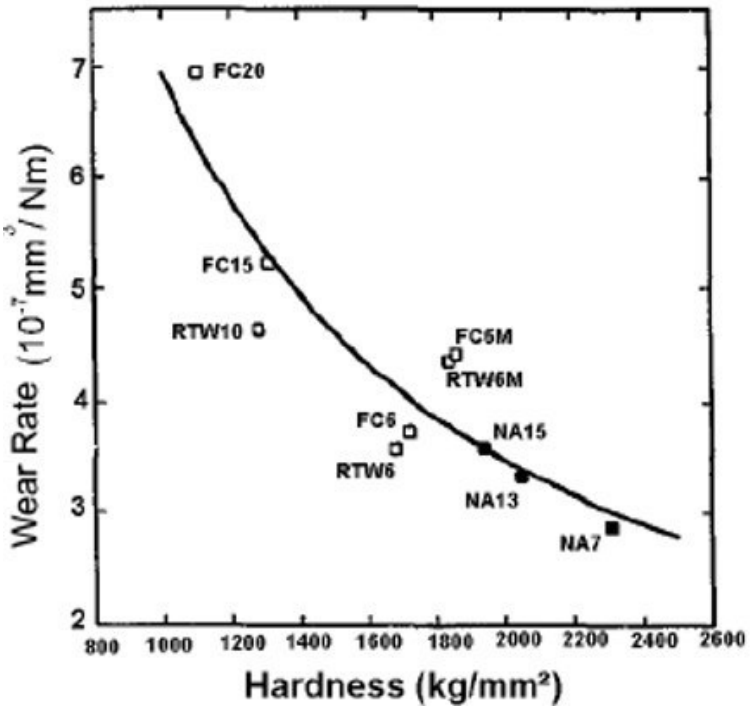


**Figure 19.** The variation in the wear rate with hardness of WC-Co hardmetals sliding against silicon nitride at 9.8 N applied load and 31.4 mms-1 sliding speed **(34).**

. All the samples exhibited a similar friction coefficient with a value between 0.4 and 0.5, even though they had different wear rates. The WC grains on the worn surface were very smooth and polished with occasional slip or cleavage features. Limited preferential binder removal was observed and the wear scars showed no evidence of plastic deformation on the micrometer or larger scale. In this work it was found that smaller WC grain sizes led to a lower wear resistance in spite of an increase in hardness. The wear was found to increase with increasing cobalt content, with the wear rate of nanostructured materials with equal cobalt content being only 60% that of the conventional counterpart. Jia and Fischer concluded that the best way to increase sliding wear resistance was to reduce the cobalt content and increase the WC grain size.

### *1.5.6.3 Abrasive wear behavior*

As a result of the different properties of the WC and Co phases the abrasive wear of cemented carbides is complicated. The abrasive wear of WC-co hard metals is divided into categories that depend on the size and hardness of the abrasive particles. Wear by grits that are 1.2 times harder than the composite belong to the “hard abrasive region” whereas the “soft abrasive region” refers to wear by softer grits, which exhibit a lower wear rate (35). Within each category there are subdivisions defined by the size of the abrasive grooves in relation to the microstructure. If the grooves are large in comparison to the microstructure the wear is called tough and if the groove size is comparable to or smaller than the microstructure the wear is called mild. The abrasive wear of WC-Co hard metals will be discussed according this nomenclature. The relative wear ranking of hard

metals is highly dependent on the triboysystem and is further influenced by the size and nature of the abrasive used, the abrading wheel speed, the applied load and the material properties.

#### *1.5.6.4 Mild abrasive wear*

In mild abrasive wear the abrasive particles are affected by the individual properties of each phase in the hard metal and are not affected by the average bulk properties. The wear resistance of a composite can be determined from the load distribution on its phases and their individual wear resistances (36). The optimal wear resistance is attained when the phases are worn down in parallel and the minimal wear resistance occurs when each phase is worn independently of the other. In cemented carbides the fraction of the hard carbide phase is high which means that the thin layers of Co binder between the carbide grains can be assumed to behave differently from bulk cobalt. Different cemented carbides with hardnesses ranging from 950-1850 HV have been found to have very similar wear resistances, very similar to the average of monocrystalline WC.

#### *1.5.6.5 Hard abrasives*

Large hard grits act as cutting tools and lead to the formation of grooves that are larger than individual WC grains. This takes place in applications where the load is high, such as the grinding of cemented carbides. The wear rate increases with the groove depth in correlation to the indentation hardness. In this type of wear WC grains are removed from the surfaces as small fragments and in some cases fatigue cracks below the worn surface have also been observed (35).

#### *1.5.6.6 Soft abrasion*

In the soft abrasion region the abrasive particles are not able to penetrate the hard metal surface. The abrasive particles slide over the surface pushing the WC grains back and forth and causing the extrusion of cobalt and fragmentation of the carbide grains.

Damaged material is then either removed by the abrasive grits or smeared over the material surface. In this wear regime the wear resistance has been found to be proportional to the mean free path of the cobalt binder and finer WC grains and a lower cobalt content increase the wear resistance.

The abrasive wear behaviour of fine-grained hard metals differs from that shown by coarser grained hard metals. The fine-grained microstructures offer higher resistance to microcracking than the coarser cemented carbides with the same hardness. As WC grains decrease in size their individual fracture toughness increases, i.e. the crack resistance increases (37).

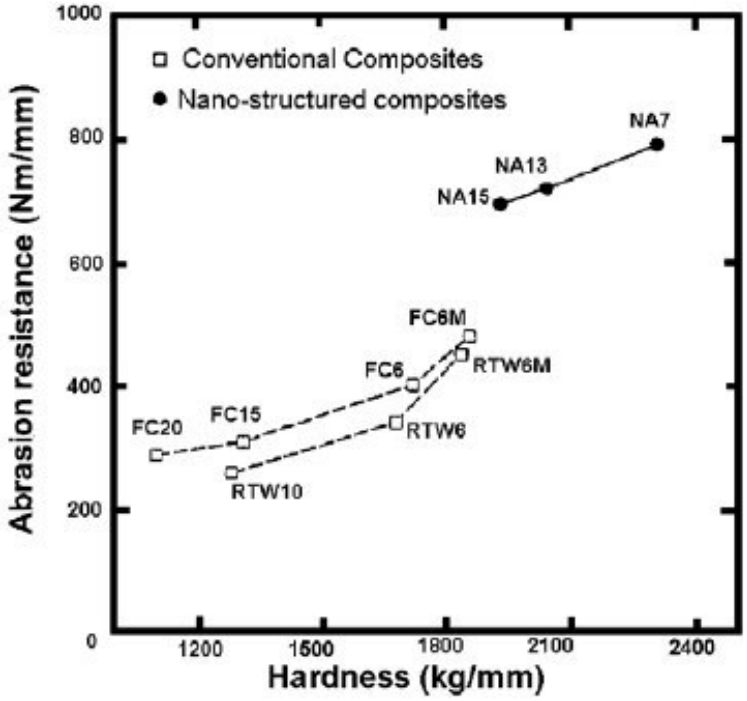


**Figure 20.** The variation of resistance with hardness of WC-Co composites from absrasion by diamond, Full symbols: nanocomposites and open squares: conventional cermets **(19)**.

## 1.6 Cemented carbide grades for circular saw blades

The information on cemented carbides and cermets used in cutting blades, unlike mechanical tools such as turning and milling, are difficult to find in both scientific and technological literature, the heritage of manufacturers. In scientific-technological literature and especially in industrial patents, information on blades can be found in which the carbide composition has been studied for specific uses. As an example, the patent (13) is shown, the object is a circular blade for cutting stainless steels, with coated carbide inserts. The choice of carbide fell on a simple carbide (containing only WC as carbide and Co as binder) of sub - micrometric size (0.1 - 0.8 μm) with a percentage of WC ranging between 90 and 98% and the remaining 2 - 10% of binder only. Carbides P30, M20 and of the K series are also used for blades which are used in cutting tool steels and stainless steels.

The inserts to be used in a cutting blade must have a high resistance to wear and a higher toughness. The intrinsic characteristic of the cutting process involves continuous impacts of the teeth with the material to be cut: for this reason, materials with low toughness are excluded such as those presented in the chapter "alternative materials" (cermet, polycrystalline diamond, boron nitride). Since toughness is a parameter directly connected to the fraction of binder, it would be appropriate to consider among the carbides to study those with fractions between 8 - 10% and 12 - 15% by weight of Cobalt. Other parameters on which to act for the choice of the best material are the grain size, the presence of other carbides (γ phase) and the functionalization of the layers.

The reduction in the size of the crystalline grain on the one hand increases the resistance to wear of the insert but at the same time reduces the values of toughness, although the scientific literature does not appear to be unambiguous in this regard (38). It can be assumed that wear resistance is the main parameter in determining the life of a tool and that an increase in it is, consistent with the maintenance of acceptable toughness, an objective to be pursued. For these reasons it is considered promising for research the study of carbides in size is superior to micron (1μm <d <5μm) than less than micron (d <1μm) so as to evaluate the right properties for the use required to the inserts containing the oversizing (in this case related to the fineness of the grain) and consequently the costs.

Carbides forming crystalline phase with a centered body (phase γ) (TiC, (Ta, Nb) C, TaC) contribute to increase the hardness and therefore the wear resistance of cemented carbides. Formulations containing mixed carbides in increasing percentage up to a total of 20% by weight can be considered.

## 1.7 Wear in cutting tools

The prediction and control of wear is one of the most essential problems emerging in the design of cutting operations (4). Tool failure is said to occur when the tool no longer performs the desired function whereas total failure (ultimate failure) is defined as the complete removal of the cutting edge, a condition obtaining when catastrophic failure occurs (39).

Machining of metals is a complex process. A wear mechanism is a classification of the process by which material is removed from the contact surface. Cutting tools are subjected to different wear mechanisms which can be distinguished depending either on the main wear process that takes place or based on the place where wear acts.

The cutting tool environment features high-localized temperatures (~1000 ºC) and high stress (~700 MPa). The tool may experience repeated impact loads during interrupted cuts, and the work piece chips may chemically interact with the tool materials. The useful life of a cutting tool may be limited by a variety of wear processes such as crater wear, flank wear or abrasive wear, built up edge (40).

- Flank abrasive wear is the most common type of wear and the preferred wear type, as it offers predictable and stable tool life. Flank wear occurs due to abrasion, caused by hard constituents in the workpiece material.
- Crater Wear is localized to the rake side of the insert. It is due to a chemical reaction between the workpiece material and the cutting tool and is amplified by cutting speed. Excessive crater wear weakens the cutting edge and may lead to fracture.

- Built up edge is caused by pressure welding of the chip to the insert. It is most common when machining sticky materials, such as low carbon steel, stainless steel and aluminum. Low cutting speed increases the formation of built-up edge, as for adhesive wear in general.
- Plastic deformation takes place when the tool material is softened. This occurs when the cutting temperature is too high for a certain grade. In general, harder grades and thicker coatings improve resistance to plastic deformation wear
- Thermal cracks occurs when the temperature at the cutting-edge changes rapidly from hot to cold and multiple cracks may appear perpendicular to the cutting edge. Thermal cracks are related to interrupted cuts, common in milling operations, and are aggravated using coolant.
- Edge chipping/Breakage known as chipping or breakage is the result of an overload of mechanical tensile stresses. These stresses can be due to many reasons, such as chip hammering, depth of cut or feed that is too high, sand inclusions in the workpiece material, built-up edge, vibrations or excessive wear on the insert.
-

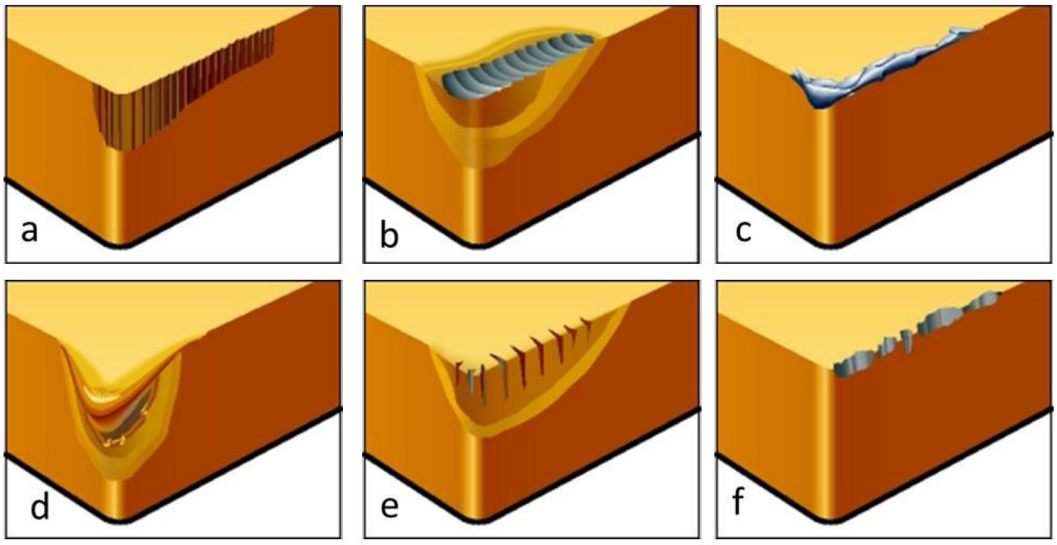


**Figure 21.** Wear modes on cutting tools. a) Flank abrasion, b) Cratering, c) Built up edge, d) Plastic deformation, e) Thermal cracking, f) Edge chipping.

### 1.7.1 Tool wear Curves

There are three distinctive regions that can be observed on Tool wear curves. The first region is the region of primary or initial wear. Relatively high wear rate (an increase of tool wear per unit time or length of the cutting path) in this region

is explained by accelerated wear of the tool layers damaged during its manufacturing or resharpening. The second region is the region of steady-state wear. This is the normal operating region for the cutting tool. The third region is known as the tertiary or accelerated wear region. Accelerated tool wear in this region is usually accompanied by high cutting forces, temperatures and severe tool vibrations. Normally, the tool should not be used within this region.

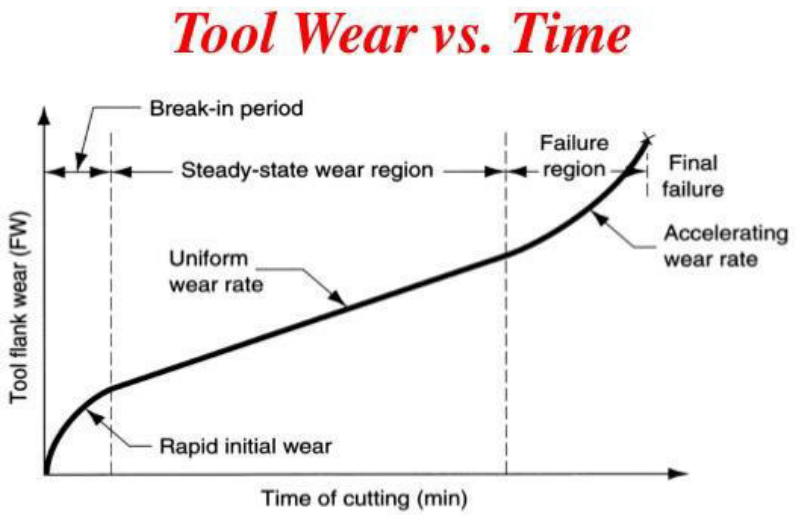


**Figure 22.** Characteristic tool wear Curve.

# Chapter 2

# Hard coatings

## 2.1 Introduction

Thin coatings obtained from vapour deposition such as Chemical Vapour Deposition (CVD) and Physical Vapour Deposition (PVD) and are very important in a wide range of application such as cutting tool, gears, metal forming and so on. In particular, hard coatings play an important role in the surface finishing of tools, machine parts and even decorative applications because of theirhardness, good wear resistance, reduced friction coefficients, excellent corrosion resistance and, in part, nice colours. Hard and wear resistant coatings are increasingly used in order to reduce material losses or to increase the lifetime of tool and machine parts (41). Usually they are called hard material when the hardness is around 20 GPa, superhard with a hardness of 40 GPa and ultra-hard materials when is 80 GPa (42). This big difference depends on the coating design that influences the microstructure (grain size and type of nanostructure), chemical bonds, residual stress of the coating and the substrate temperature during the deposition (43). In Figure 23 it is possible to see the different types of nanocomposite coatings and the different change in properties in relationship with different chemical bonds.

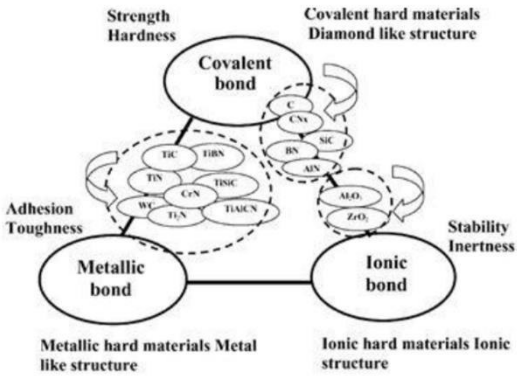


**Figure 23.** Hard materials for nanocomposite coatings in the bond triangle and changes in properties with the change in chemical bonding.

## 2.2 Film deposition growth

During PVD coating, the film material is usually deposited atom by atom on a substrate by condensation from the vapour phase onto the solid phase. Normally the coating atoms impact with low kinetic energy (few eV) and produce a film by the following simplified growth route (44).

The processes that take place during the formation of a thin film are mainly nucleation and growth. The whole phenomenon can be divided in different steps (45):

- The impacting species are physically adsorbed on the substrate surface.
- Due to the non-thermal equilibrium, the species move over the surface and create clusters.
- The clusters tend to desorb and, depending on the deposition condition, can collide with other infringing species and start growing. This step is called nucleation stage and it is the most important step in PVD since it strongly affects coating adhesion, grain size, orientation and density.
- In this step the critical nuclei grow and produce islands, until a saturation nucleation density is reached. This phenomena depends on the energy and the rate of the impinging species, the activation energies of
- adsorption, the temperature, the topography, and the chemical nature of the substrate.
- The small islands start to coalesce and form big island, until their growth fronts meet other islands growing similarly. The effect of this is to provide a grain boundary defect and from this point to promote island growth only in the vertical direction.
- In the last step, the islands start to grow vertically together carrying to the formation of holes and leaving channel. The structure of the films at this stage changes from discontinuous island type to porous network type.

The growing process depends on:

1. the substrate surface roughness
2. the surface temperature
3. the adatoms surface mobility
4. the geometrical shadowing effects
5. the chemical reaction with other species
6. the mass transport during deposition
7. the deposition parameters

In ion plating where there is additional high energy particle bombardment, additional factors include:

- Adsorption of inert and reactive gaseous species on the growing surface
- Gas scattering of vaporized particles
- Concurrent bombardment by high energy particles.

## 2.3 Coating structure zone models (SZM)

The understanding of the film microstructure in relation with temperature and pressure was studied first by Movchan and Demchishin (45) and after by Thorton (46).

In 1969 Movchan discussed how surface, grain boundary and bulk diffusion influence film morphology of metal coatings. The model distinguishes between three zones, as shown in Figure 24. Considering the normalizing temperature Ts/Tm where Ts is the surface temperature and Tm is the melting temperature, three main zones can be defined in the SZM diagram:

- Zone 1 for Ts/Tm < 0.3: the film has a conical or columnar structure
- Zone 2 for 0.3 < Ts/Tm < 0.5: columnar grains appear
- Zone 3 for Ts/Tm > 0.5: structure of fully annealed metal with equiaxial grains

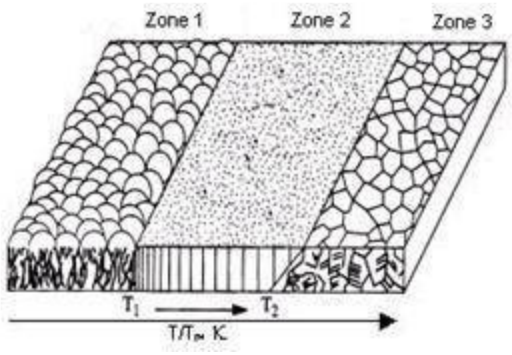


**Figure 24.** Structure zone model by Movchan and Demchishin **(45)**.

# 2.4 Coating architecture

## 2.4.1 Introduction

The study of the deposition parameters is fundamental to produce the desired architecture. It is possible to controlled chemical composition and layer sequence through a set of parameters according to obtain the required coating (47).

The possible coating architectures are:

1. Monolayer coatings with different thickness (Figure 25.a).
2. Multilayer coatings with layer thicknesses of the order of nanometers or micrometers (Figure 25.b).
3. Compositionally gradient layer (Figure 25.c).
4. Multiphase composite coatings with phase dimension of the order of several thents of nanometers to some tents of nanometers (Figure 25.d).

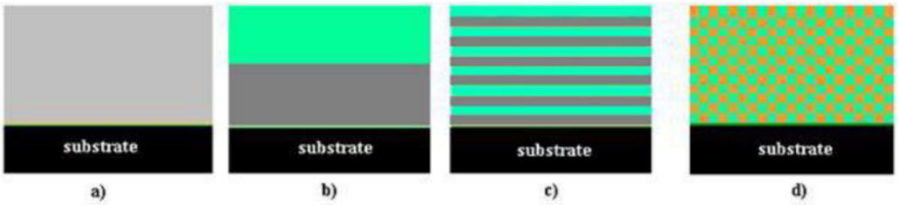


**Figure 25.** Some of the possible structures of thin films coatings, a) monolayer, b) dual layer, c) multilayer/superlattices, d) composite.

## 2.4.2 Monolayer coatings

The single layer is a coating deposited on a appropriately prepared substrate in one process or technological operation, comprising one layer of material.

Single layer coatings are divided in:

- Single constituent coatings consisting of one material, e.g., TiN, CrN, etc
- Multi component coatings consisting of several material components, e.g. WC/Co, WC/C etc.

The most frequently studied compounds are the transition and refractory metal nitride (TiN, CrN, AlN), carbide and boride films, most of these materials crystallise into interstitial solid solutions with a face centred cubic structure (48). Multicomponent coatings based on different metallic and nonmetallic elements combine the benefits of individual components leading to a further refinement of coating properties. Alloying addition onto the base TiN structure, such as Cr and Y drastically improves the oxidation resistance, Zr and V improve the wear resistance, whereas Si increases the hardness and resistance to chemical reactivity of the film. Addition of B improves the abrasive wear behaviour of Ti-Al based nitride coatings due to the formation of TiB2 and BN phases depending on the deposition conditions. Hf based nitrides and carbides have potential for resistance to flank and crater wear (42).

## 2.4.3 Dual layer coatings and multilayer coatings

The multilayer layer coatings consist of two or more layer of materials. They may be constituted by layers of the same material, separated by a layer of another material or they may be layers constituted by different materials. The aim of applying more than one layer is the improvement of some selected properties.

The following modification of multilayer coatings structure are known:

- Multiple coating: comprising two or more layers of some material, deposited in technological environment that differ only slightly as to physico-chemistry properties.
- Sandwich coating; comprising several layer of different materials with at least one of them occurring twice and not directly on the top of the same material, with each material layer of nanometre scale, the total thickness of the two successive pairs of layer, known as the bilayer thickness o superlattice period (λ), depends on the substrate rotation speed and the deposition rate.

The progress on this typologies of structures began since the late 1980‟s, with creation the multilayer hard coatings with hardness values exceeding 50 GPa. This

structures form part of the second generation of PVD coatings, which are considered to be the multicomponent materials.

The properties of the multilayer coatings depend on the properties of the constituent materials, the modulation wavelength or bilayer thicknesses and the interface structure (44).

### 2.4.4 Composite coatings

A composite coating usually consists of two or more phase combined either as different layers (multilayer or laminate) or as homogeneous isotropic mixture of different phase. The properties of this type of coatings depend not only on the composition but on the size and the distribution of the separate phases.

These can generally be defined by two classes:

- metal/ceramic composites
- ceramic/ceramic composites.

The properties of composite materials vary also as a function of the size of the reinforcing phase.

### 2.4.5 Nanocomposite coatings

Nanocomposite coatings have recently attracted increasing interest because of the possibilities of synthesizing materials with unique physical and chemical properties. Because of their superior mechanical properties (in particular hardness and toughness) and high chemical inertness, these coatings can significantly decrease the friction coefficient and increase the wear resistance and, at the same time increase the resistance to fatigue, erosion and corrosion.

They can be applied on most ceramic and metallic substrates with strong bonding; with the new developed techniques it is possible to deposit nanocomposite coatings on all kind of substrates.

Nanocomposite coatings are composed of at least two phases: a nanocrystalline phase and an amorphous phase, or two different nanocrystalline phases (49).

These new types of coatings represent an innovating concept of material whose hardness and properties are not subjected to the volume mixture rules, but depend on grain boundary effect and on the effect of the composite element.

Therefore, a schematic representation of the different possible nanostructured is shown in Figure 26. The first one (Figure 26.a) represents a columnar nanostructure composed of grains assembling in nanocolumns. The second one (Figure 26.b) represent a dense globular structure composed of grains fully surrounded by tissue phase. The third one (Figure 26.c) is formed by a mixture.

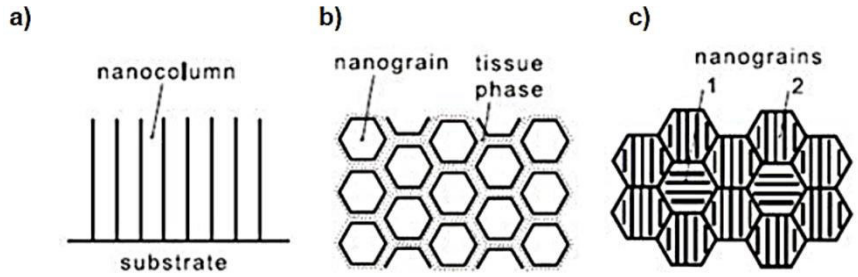


**Figure 26.** Schematic illustration of the different nanostructure. a) nanocolumn; b) nanograin; c) mixture.

# 2.5 Coating defects

## 2.5.1 Introduction

The growth defect phenomena are very well known in all coating technologies. Any imperfection formed on substrate surface during pretreatment or growth defects in coatings prepared by physical vapour deposition are very often drawbacks in their applications (50).

They can cause:

- local loss of adhesion,
- sticking of workpiece material,
- higher friction,
- voids and pitting corrosion

Namely there are different causes that affect substrate and coating surface defects. In general, most coating defects are produced by foreign particle contamination on substrate surface before and during coating, while part of them originate from evaporation or sputter source due to arcing (51). In certain applications, coating imperfections cannot be tolerated.

## 2.5.2 Growth Defects

The growth of PVD coatings takes place far away from the thermodynamic equilibrium resulting in high defect densities within the coating. Growth defects can be divided in microscopic and macroscopic defects.

The microscopic defects appearing in coatings can be further distinguished in:

- 0-dimensional defects: intrinsic point defects such as self interstitials or vacancies appear due to fast effective quenching of the vapour and to the collision cascades of the incident particles. As a consequence, precipitations are accelerated and intrinsic point defects can form clusters or complexes with extrinsic defects. The incorporation of noble gas atoms or impurities by substitution on regular lattice sites is called extrinsic point defects. These defects arise due to collision cascade or implantation resulting in a remarkable volume change of lattice which

leads to residual stresses. Extrinsic point defects are usually generated simultaneously with intrinsic point defects (52).

- 1-dimensional defects: generation of dislocation. It is assumed that in layers with grain sizes larger than 0.1 mm the dislocation density is similar to those in highly deformed metal. In contrast to this, the existence of dislocations in nanocrystalline materials is discussed controversially. In these materials the annihilation of generated dislocations is favoured because of the high number of grain boundary regions, which makes the material elastically strongly inhomogeneous.
- 2-dimensional defects: grain boundaries.
- 3-dimensional defects: considering zone 1 of the microstructure model a remarkable porosity between the grain appears, which results from shadowing effects of the incident particles especially at a low angle incidence. These defects are called cavities.

Other defects that belong to this category are clustering of vacancies or coalescence of Ar or N, which are incorporated during the deposition rocess in the formation of pores.

## 2.5.3 Macroscopic defects

Hillocks, pinholes and doplets are the most common macroscopic defects of thin coatings (53).

The formation of pinholes is connected to the soruface roughness (Figure 27). The most dense PVD coatings ca be achieved by smooth substrate surface because of the lack of macro-columnar morphology, which would result from geometrical shadowing features on the substrate surface. The dropletes have a detrimental influence on the corrosion behavior of coatings. Growth defects are generated on top of droplets during deposition process due abnormal coatings growth above droplet.

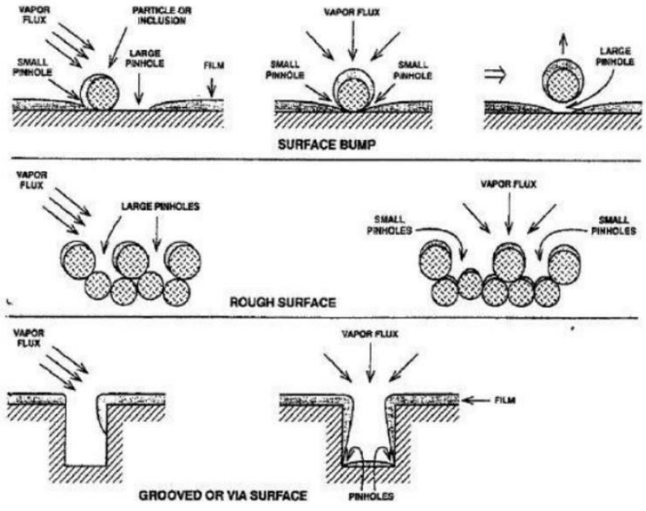


**Figure 27.** Effect of surface features and angular distribution of deposition flux on film deposition: top, inclusion or particle contamination; middel, rough surface, single surface feature.

The ejection of melt metal droplets is integral to the vaporization of neutrals and emission of electrons during the process of arc discharge . During this process an arc travels along spots across the target surface with a short dwell time ($10^{-7}$ ms). Due to the strong heating of the target surface micro molten pools are developed at the spots. The target metal plasma consisting of vapour ions, vapour neutrals, electrons and liquid metal droplets are ejected by the molten pools (44). The liquid droplets can solidify during the flight to the substrate and form coating macrodroplets there. The number, density and size of droplets depend on parameters like the cathode current or power, target melting point, and background gas pressure (47).

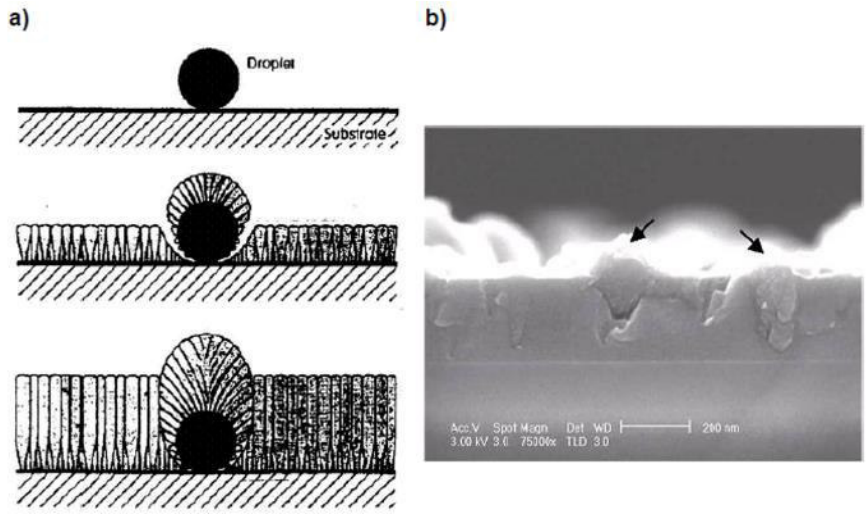


**Figure 28.** a) Schematic illustration of the formation of a nodular defect overgrowing an arc induced macro particle; b) Coating deposited through Cathodic Vacuum Arc, arrows indicate macroparticles in the coating (droplets).

A schematically illustration of the formation of a growth defect from a droplet is shown in Figure 296.a and defects are shown in Figure 296.b. Growth defects exhibit a distinct structure from the rest of the coating and as it grows it creates its own boundary. This microstructure is usually composed of dense columnar grains extending in a feathery pattern outwards from the core. Around the base of the defect the coating become severely under dense due shadowing and hence less intense ion bombardment. The detrimental effects of droplet formation are as follows: local loss of coating adhesion, surface roughening and formation surface shrinkage porosity due to a droplet self-repulsion mechanisms. The self – repulsion mechanisms is explained in Figure 29. The bonding strength of the droplets is very often not sufficient to maintain the droplet from being expelled out of the coating due to increasing compressive stress of the growing coatings or an undergrowing of the spherical droplets (54). If the expelling even takes place shortly after the film growing is initiated then the hole will be refilled by the growing film resulting in the formation of a dish like defect. If droplets leave the substrate and the coating in a late stage of the film growth, which is a rare event, then it will result in rather deep holes or craters in the coating .

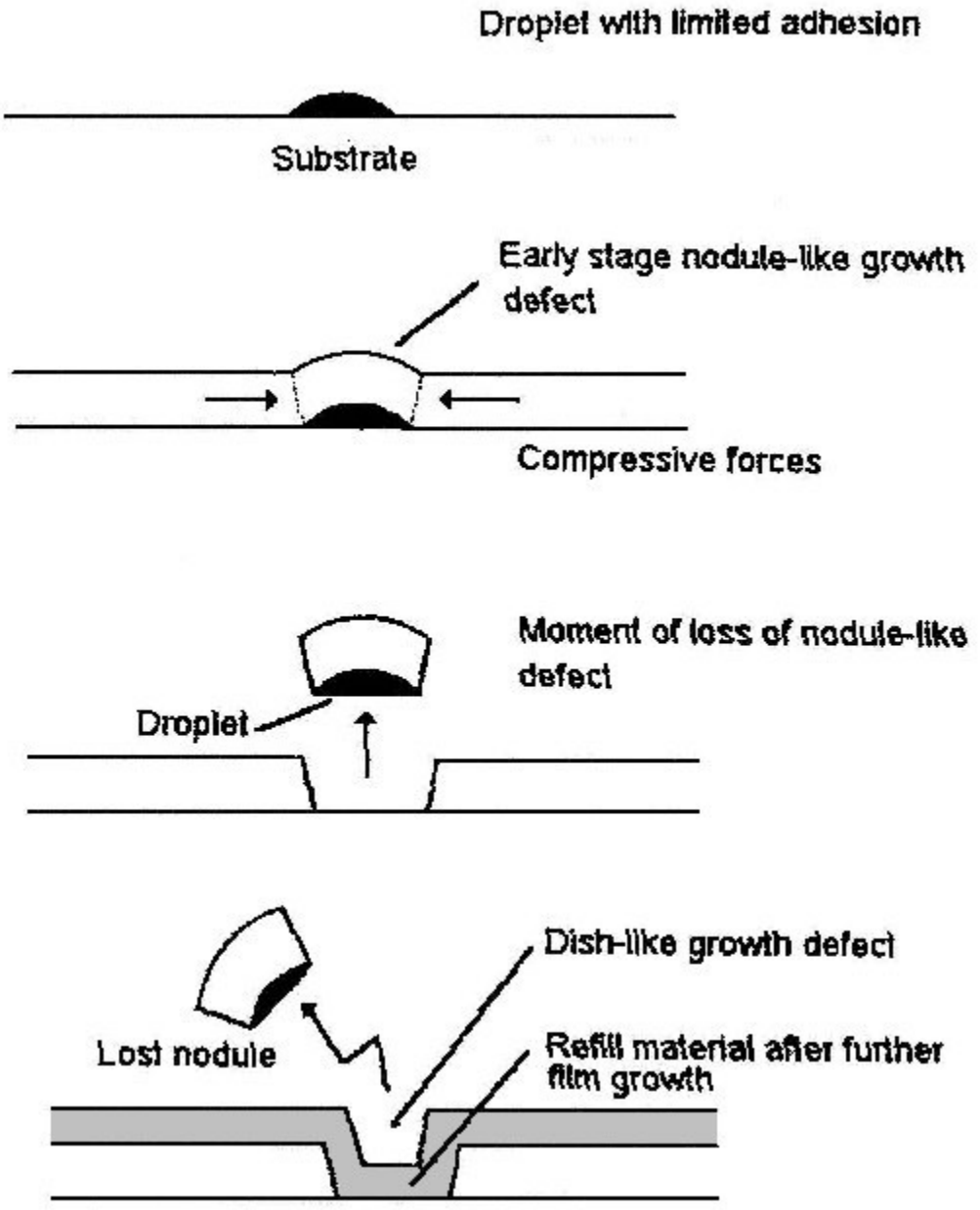


**Figure 29.** Schematic explanation of the self expulsion mechanisms of droplets **(54)**.

## 2.6 Thin film properties

### 2.6.1 Hardness

The hardness of a material is determined by the strength of the interatomic forces and by the crystal structure that affect the deformation mechanisms.

Materials exhibiting a high intrinsic hardness are characterized with high cohesive energy, short bond length and high degree of covalent bonding. A high resistance to dislocation propagation and multiplication can, for example, be achieved in materials with a high bond strength, and highly directional bonds such

as covalent bond that can hinder dislocation propagation. In general, the hardness decreases as the proportion of covalent bonding decreases. Some typical micro structural features that influence the hardness value are: impurity atoms, dislocation, grain boundaries, precipitates and vacancies.

The most generic feature observed in thin film microstructure is the small grain size d (usually<1μm). If the films are deposited at low temperature with respect to their melting point temperature Tm, d can be 5-10 nm. Hardness typically decreases with increasing grain size according with the Hall-Petch relation (55):

$$H = H_0 + k\sqrt{d}$$

where $H_0$ is intrinsic hardness of mono crystal, d is the average size of crystal grains and k is a constant depending on the material. With a decreasing in grain size, the mobility and the multiplication of the dislocation are hindered. This effect is particularly important for grain size down to tens of nanometres (56) being for such reason this grain size referred as critical size (dc). Below this grain size, further reductions in grain size (Figure 30) bring about a decrease in strength because of the activation of grain boundary sliding effect (Figure 30). In the region above of the maximum hardness (at d>dc), the transition to the activity of intragranular process and dislocation activities occurs. In the other region, where d<dc deformation mechanism is the intergranular process dominated by small-scale sliding in grain boundaries.

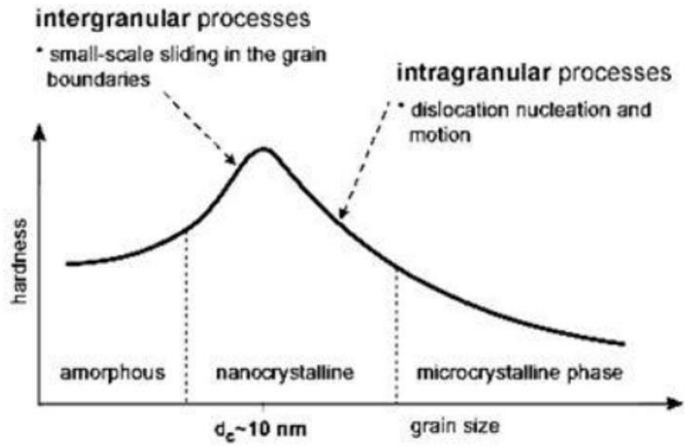


**Figure 30.** Graphic illustration of material hardness vs. size of grains **(57).**

In nanocomposite coatings, the hardness can be also influenced by the ratio of the amorphous and the crystalline phase and from the orientation of the crystal. Some alloying elements can also be helpful to increase the hardness, for instance by adding the Al in the TiN coating the hardness increases since the interatomic distance decreases and lattice deformation is provided (57). Superhardness was also observed in multilayer materials and it has been explained by a model based on the dislocation motion within the superlattice structure, accounting also for the role of the real interface structure on the dislocation mobility (58).

### 2.6.2 Friction and wear

Mechanical failure due to wear is probably the most common cause of direct or indirect engineering component disposal from service. Lubricants are often used to reduce the friction forces and the galling tendency between the contacting surfaces in sliding systems, e.g. in sheet metal forming operations. But today in order to enhance the surface properties of materials, and to limit the use of lubricant for environment benefit, producers of components are moving to different surface treatments and, in particular, to hard protective coatings. The benefits of applying engineered surfaces in sheet metal forming applications include: improved working environment in the workshop, reduced friction forces, increased tool wear resistance (59).

To be effective the engineered surface must strongly bond to the substrate and have a low tribological affinity due to both its chemical composition and mechanical properties with the mating counterpart surface. Furthermore, the engineered surface should remain chemically and structurally intact under the contact conditions loads, temperatures, etc. to which it is exposed. Monolithically grown columnar structured coatings experience severe plastic deformation and cracking, which could lead to the release of large wear particles often reaching several tens of nanometers in diameter. In contrast, it was observed that at high mechanical loads the wear occurs preferentially by the coalescence of cracks generated approximately parallel to the worn surface within volumes involving only a few individual layers from the structure (8-10 nm).

### 2.6.3 Fracture toughness

Residual stresses in functional coatings play an important role, The mechanical performance of PVD coatings is to a high degree coupled to the stresses that usually are built up during growth, in the same way the performance and lifetime of the coated component.

The origin of residual stresses in PVD coatings can be divided into two components, a thermal and an intrinsic contribution. The thermal contribution origins from the fact that the thermal expansion differs between the coating and the substrate. Hence the shrinkage of the coating will be different from that of the substrate material during cooling down after deposition. The intrinsic stress is due to the accumulating effect of atomic forces generated throughout the coating volume by atoms which are out of position with respect to the minimum in the interatomic force fields.

Generally the resulting coating properties are strongly influenced by the deposition method and the selected deposition condition. The mechanical integrity of a functional coating is influenced by residual stresses which derive from four principal sources: growth stresses, geometric constraints, thermal gradients and service stresses. When a coating-substrate composite is deposited at elevated temperature and cooled down to room temperature, the thermal expansion

mismatch between the coating and the substrate results in thermal residual stresses that can cause perpendicular microcracking (60).

The effect of a compressive stress is the formation of microcrack that can propagate along the interface. Figure 31 shows schematic image of the failure mode is shown. In the first one the coating is under tensile stress and with a „weak" interface the coating start to delaminate that means low adherence. In the second one the coating is under tensile stress but with a strong interface. In this way start perpendicular microcracking. In the last one the film is under compressive stress and a phenomena of buckling and spalling start to appear (61).

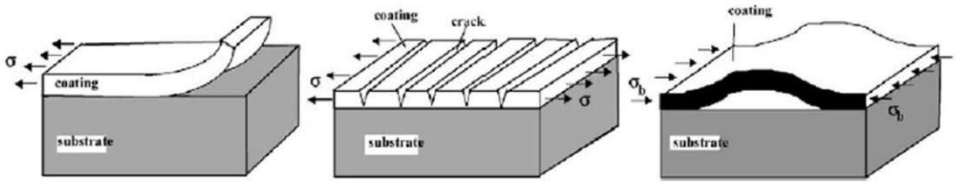


**Figure 31.** Failure modes of a thin coating under residual stress.

# Chapter 3

# Materials & methods

## 3.1 Cemented Carbide characterization

Four grades of cemented carbides were chosen in this part of the study and characterized from the point of view of morphology, composition, mechanical properties and wear resistance. The aim of this characterization was to identify and select the best candidate to be used as cutting insert in TCT – saw blades for high speed cutting of metallic alloys.

The four grades chosen for this characterization and their composition are listed in the table below (Table 3). Three mixed grades and a plain grade produced by Sinterloy s.r.l. were chosen; all these grades are employed in steel cutting but, based on the properties highlighted in the first chapter, a specific choice based on tailored properties was done with this characterization. The optimal candidate has superior toughness with respect to the other grades and higher sliding wear resistance.

**Table 3.** Nominal composition for cemented carbides employed in this study.

| | **K15** | **M20** | **P35** | **P40** |
|---|---|---|---|---|
| **WC [wt%]** | 89.5 | 82.21 | 74.23 | 79.00 |
| **Co [wt%]** | 10.00 | 8.05 | 11.37 | 11.00 |
| **Co [%vol]** | 16.1 | 11.3 | 14.4 | 15.1 |
| **TiC/TaC [wt%]** | - | 9.54 | 14.40 | 10 |
| **Grain refiners (VC, $Cr_3C_2$) [wt%]** | 0.50 | 0.20 | 0.10 | 0.10 |

The different procedures adopted for testing the cemented carbide properties will be further described in the next paragraphs and are:

- Microstructural and compositional characterization by scanning electron microscope (SEM + EDS) and XRD
- Hardness and toughness
- Grain size determination by image analysis

### 3.1.1 Microstructural and compositional characterization

Platelet shaped samples 20 * 20 * 2 mm were employed in this part of the study (Figure 32), handling such samples in fact is easier and they can be easily fit inside the SEM chamber. These same samples, provided with a hole for hanging inside the PVD chamber and pre – cracked, were then coated and used for coating characterization.

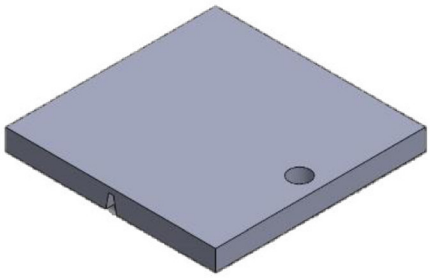

**Figure 32.** Platelet sample made of cemented carbide.

The surfaces were grinded with diamond discs (75, 54 and 18 μm) and then polished with diamond suspension on cloth (3 and 1 μm) before microstructural observation. The SEM used in this thesis is a LEO 1450-VP present at Politecnico di Torino, Alessandria Campus (Figure 33). Based on thermoionic effect equipped with secondary and back scattered electron detectors and with microprobe for one point and mapping semi-quantitative analysis of chemical composition. A Field Emission Scanning Electron Microscope – ZEISS Merlin present at Politecnico di Torino, Torino – Campus, equipped with secondary and back scattered electron probes able to reach higher magnifications was used for more accurate evaluations of the interfaces of coatings and wear products.


**Figure 33.** SEM equipment at Politecnico di Torino, Alessandria Campus. On the right the FESEM ZEISS MERLIN.

The same samples were submitted to XRD analysis in order to assess the phase composition of the cemented carbides and above all to exclude the presence of deleterious phases for cutting applications such as the η – phase (62). In this thesis was used a X'Pert Philips equipment present at Politecnico di Torino,

Torino Campus, with Cu kα radiation and λ = 0.154060 nm. Each XRD sample scan had been done with 2ϑ from 30° to 100°.

### 3.1.2 Mechanical properties assessment: hardness and toughness

Hardness and toughness of the considered cemented carbides have been evaluated using a durometer to equipped with a Vickers indenter and loaded with 30 Kg ($HV_{30}$). For greater measurement accuracy imprints made in this way and the relative cracks in the tips have been observed and measured by a metallographic microscope (Leica MEF4 M, Figure 34), rather than through the measurement apparatus present on the instrument (Figure 35).

**Figure 34.** Leica MEF4 M metallographic microscope at Politecnico di Torino, Alessandria Campus.

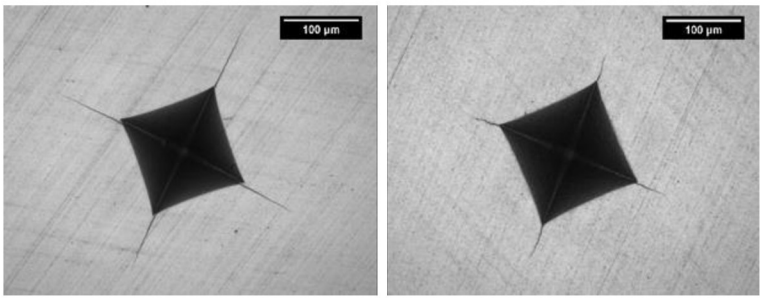


**Figure 35.** Example of the $HV_{30}$ imprints measured.

The value of the Vickers hardness (HV) is obtained has been obtained through the formula:

$$HV = 2 \cdot sin\left(\frac{136°}{2}\right)\left(\frac{F}{\bar{d}^2}\right)$$

with the applied load (measured in kilograms-force) and the average dimension of the diagonal of the indentation (measured in millimeters), 136 ° is the opening angle of the Vickers indenter. The test is carried out by indentation of the indentation with the desired load, after having brought the indenter in contact with the surface to be penetrated. After penetration, the indenter is lifted and the indentation can be measured. The test is carried out by indentation of the indentation with the desired load, after having brought the indenter in contact with the surface

to be penetrated. After penetration, the indenter is lifted and the indentation can be measured.

Toughness of the material was quantified from the measurement of cracks at the apexes of the Vickers hardness indentations following the Palmqvist approach (63).

$$K_{IC} = 0{,}0889 \cdot \sqrt{HV \cdot \left(\frac{P}{4 \cdot \bar{l}}\right)}$$

Where HV is the value of the measured Vickers hardness, P the indentation load in Newton and $\bar{l}$ the average length of cracks at the apexes of the impression, expressed in meters. The durometer was also used for the evaluation of the hardness of AISI660 and AISI4140 steels, in the form of bars, materials used for the pins for wear testing tests. The hardness tester used in this thesis is a EMCOtest M4U 025 (2005) present at Politecnico di Torino, Alessandria Campus (Figure 36). Equipped with Brinell, EN ISO 6506 / ASTM E10, Vickers EN ISO 6507 / ASTM E92 and Rockwell EN ISO 6508 / ASTM E18 indenters, able to apply loads from 9.81 to 2450 N.

**Figure 36.** Hardness tester EMCO – Tester at Politecnico di Torino, Alessandria Campus.

### 3.1.3 Grain size distribution by image analyis

The characterization of grain size distribution was performed with image analysis of SEM images acquired on the cemented carbide sample surface. Ten images were analyzed for each sample by using the image analysis software Image J (64). The chromatic variations from the images acquired both in scanning mode with secondary electrons (SE), and in scanning mode with back-scattered electrons (BSE) were exploited to identify the single WC grains. The chromatic difference between the grains is particularly evident: WC that appear clear and its coloration tends to white, compared to cobalt that appears darker, tending to black. The

secondary carbides, present only in the M20, P35 and P40 grades, appear to be a dark gray color, tending to black, barely distinguishable from the darker cobalt, which are then confused by the program with the binding cobalt. The procedure adopted for image analysis is detailed in Figure 37 and consists of a mixed application of functions present in the Image J program to obtain a binary image similar to that of Figure 38 where the the space is divided into black and white and every single WC grain is isolated from the contiguous ones.

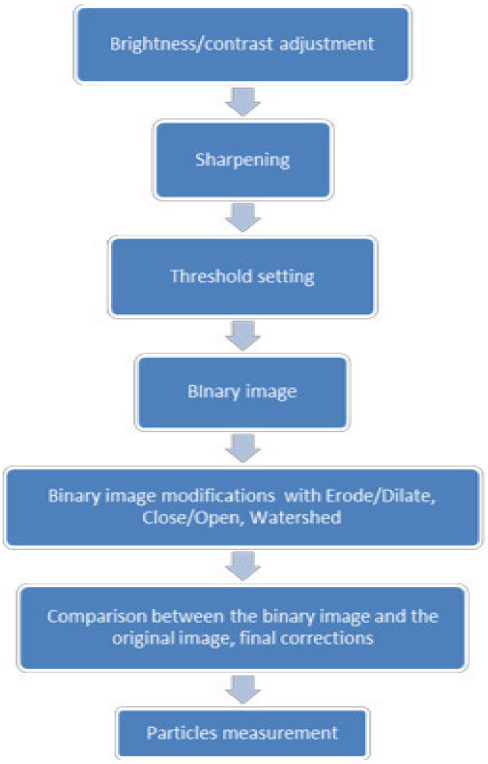


**Figure 37.** Procedure adopted to perform image analysis for carbide grain size quantification.

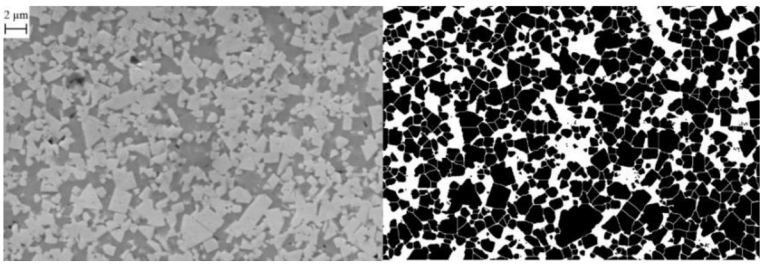


**Figure 38.** Resulting image after application of filters and binarization.

The grains were counted using a specific function present in the program and their average diameters were put into an histogram and compared.

### 3.1.4 Wear testing and characterization

The analysis of the variation of the coefficient of friction measured during the test allows to describe the different conditions of the system, respectively initial,

stationary and degenerative. In the case under consideration, the main conditions of interest are those stationary. In the present study, a tribometer of the pin-on-disc type was used to simulate the wear process that occurs on the flank of the hard metal tooth of the cutting blade for AISI 4140 ferritic steel (42 CrMo4) and AISI 660 heat and corrosion resistant austenitic alloy. The flank of the TCT sawblade is in fact subjected to high sliding speed (the maximum sliding speed, because it is the outermost part of the blade) and low normal force since it has no role in chip formation. Anyway the flank is continuously in contact with the freshly cut surface of the workpiece and it the location where tool wear takes place. The tribometer is a device used to perform tests and simulations of wear, friction and lubrication of systems subject to tribological studies. Tribometers are often extremely specific in their function and are manufactured by manufacturers who wish to test and analyze the long-term performance of their products. They can therefore be made to measure according to the specific system that you want to study. A generic tribometer can simply be described as a suspended mass and a mass placed on a horizontal surface, joined by a cable and a pulley. The coefficient of friction μ, when the system is stationary, is determined with the increase of the suspended mass up to the moment in which the supported mass does not start to crawl. Using the general equation of friction force:

$$F = \mu \cdot N$$

where N is the normal force, equal to the weight (mass by gravity) of the laid mass; F is the loading force, equal to the weight (mass by gravity) of the hanging mass; μ the coefficient of friction.

Pins of 6 mm dia. were machined from AISI 4140 (42 CrMo4) and AISI 660 stainless steel bars respectively of 28 ± 1 HRC and 31 ± 1 HRC. Uncoated cemented carbide discs made of the four grades listed in Table 3 were tested (Figure 39). The test was carried out using the maximum speed that can be supplied by the instrument (800 theoretical RPM, 1.28 m / s) and low loads (5 N) to make the simulation conditions as close as possible to the real ones, over a distance of 5000 m. During the tribological test thermal measurements were also carried out using an IR thermal camera. Wear was then measured by roughness tester in the case of the discs and via image analysis in the case of pins.

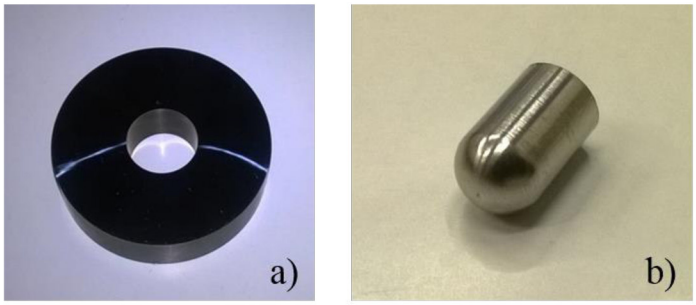


**Figure 39.** a) cemented carbide disc for wear testing, b) pin made of steel (AISI 4140/AISI 660) used for pin on disc testing.

The following procedure was adopted for wear testing: samples were thoroughly cleaned of the by rubbing cotton soaked in acetone and after measuring roughness to guarantee $R_a$ comparable to that of the saw blades (> 0.1 µm). Sample were weighted and placed on the tribomenter; the pin in the appropriate housing, adjusted according to the appropriate contact conditions, with an angle of 90 ° between the disk plane and the pin axis. The wear track was measured after the wear test, weighing did not gave significant results because of the reduced volume loss in the cemented carbides. The tribometer used in this thesis is a pin on disc tribometer present at the Politecnico di Torino, Alessandria campus, built in laboratory after the ASTM G 99 standard (Figure 40).

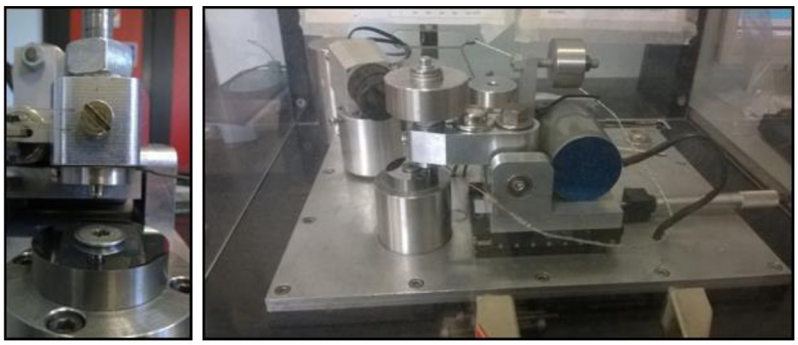

**Figure 40.** Pin on disc apparatus in Alessandria Campus tribology laboratory of Politecnico di Torino.

The temperatures present at the point of contact between pin and disk, during tribological tests, were measured using an IR thermal camera Optris PI 160 (Figure 41). The camera has acquired images of the samples in contact every 20-30 seconds, recording the temperature in the contact area. The camera was placed at a distance of about 15 cm from the samples.

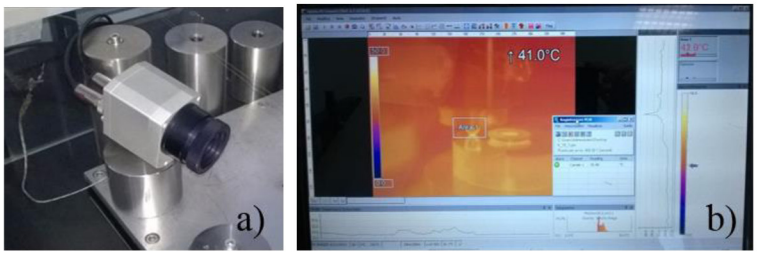


**Figure 41.** a) IR thermal camera positioned towards the tribological contact, b) IR thermal imaging software.

## 3.2 Cutting tests

In the frame of this thesis several cutting tests were done, two were the main targets of the cutting tests:

1- Experimental validation of simulated cutting geometries
2- Identification of wear mechanisms acting on TCT saw blades when cutting AISI 4140 steel

All cutting tests were performed on bars made of AISI 4140 in the quench + temper metallurgical state (28 ± 1 HRC) used for manufacturing of special boltings (after ASTM A320 / A320M - 17b). The bars diameter was kept constant throughout the entire study equal to 17.32 mm. This fact allowed to compare results from different cutting tests with the same test conditions.

The sawing station used for cutting tests is a special machine able to work at high cutting speed (up to 350 m/min) made by Rattunde GmbH (Figure 42). This control system of the sawing machine can return to screen fundamental parameters for monitoring cutting performances such as cutting torque and tool vibrations. From cutting torque expressed in N*m it is possibile to derive cutting force if the geometrical parameters of the tool are known. The very distinctive feature of this machine is that it does not have any kind of system for guiding and stiffening the blade through the cutting (Figure 42): common sawing stations are equipped with cemented carbide pads positioned closely to the saw body to support the blade throughout the cut (Figure 42). This feature allows this machine to reach higher cutting speeds reducing wear on the saw body. The target cutting parameters adopted during testing are $V_C$ = 210 m/min and $f_z$ = 0.04 mm/(tooth*rev), such parameters guarantee a productivity as high as 1200 pz/h.


**Figure 42.** Sawing head detail, on the left. Automated sawing station overview, on the right.

In each of the following paragraphs the blades used for testing will be presented along with the cutting test procedure adopted. All TCT sawblades tested had 120 teeth, a diameter of 350 mm and a thickness of 2.7 mm. The planarity of all saw blades was checked before tested, measuring with a centesimal comparator along the outer rim to be included in the interval ± 0.05 mm, this can prevent unattended ruptures due to lateral vibrations of the tool inside the workpiece. Cemented carbide material was ISO P 20 - 40 grade for all TCT saw blades tested; this decision was taken after the result obtained from cemented carbides characterization.

### 3.2.1 1st cutting tests: benchmark test

This first test had the main objective of assessing the responses of the system in terms of cutting force. A screening test with common, non optimized, cutting geometries was done in order to acquire cutting forces to calibrate the numerical model used for redesigning the cutting geometries (rake angle and rake face height

Figure 43). Each of the values in table was obtained averaging the measures taken from 8 teeth randomly chosen in the cutting tool.

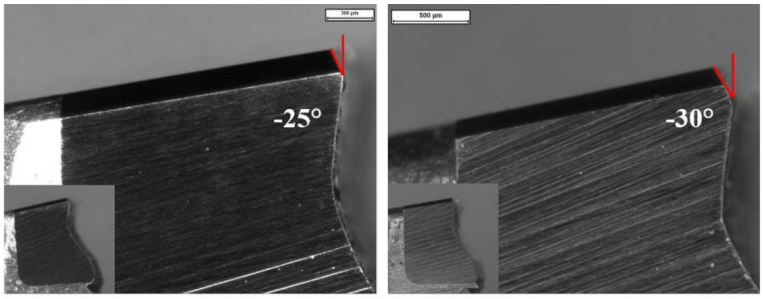


| Blade designation | Rake angle | Rake face_height |
|---|---|---|
| -25°_1 | 24.69 ± 0.71 | 0.16 ± 0.03 |
| -25°_2 | 25.00 ± 1.08 | 0.13 ± 0.03 |
| -30°_1 | 30.45 ± 0.11 | 0.22 ± 0.02 |
| -30°_2 | 30.03 ± 0.70 | 0.21 ± 0.01 |

**Figure 43.** Geometric characteristics of the tested tools.

### 3.2.2 2nd cutting test: validation of FEM results, definition of optimal cutting geometry

This second cutting test had two main objective:

- to validate the results obtained from the finite element modeling;
- to define and choose the most appropriate cutting geometry for high speed cutting of AISI 4140.

The cutting geometries tested in this experiment were less negative: -15° and -25°. A less negative rake angle can be beneficial in terms of wear reduction but exposes the rake to more severe shocks during cutting thus embrittling the insert (Figure 44). The more the rake angle goes to 0° more the resultant normal force (N in Figure 44) acts on a reduced section, as a result the cutting edge can suffer from embrittlement and finally early failure can occur due to chipping.

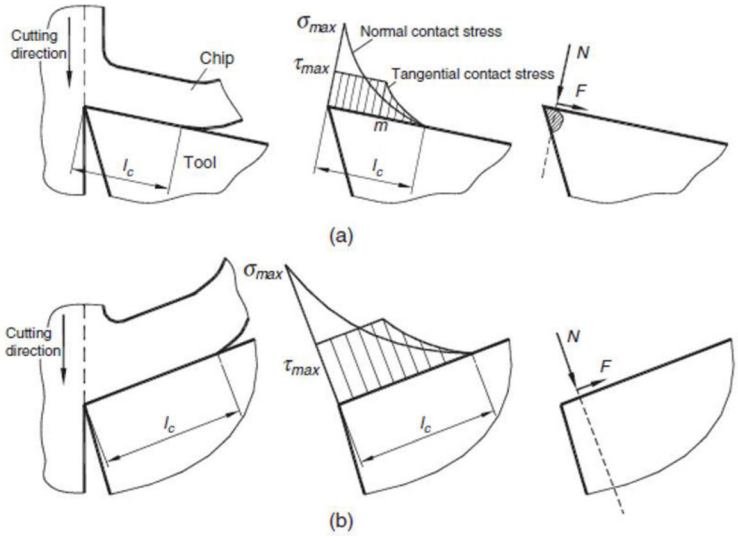

**Figure 44.** Forces acting on the cutting edge having: (a) positive rake angle and (b) negative rake **(4).**

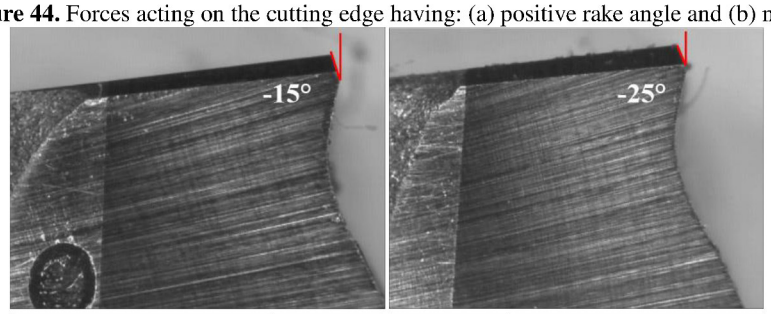


| Blade designation | Rake angle | Rake face_height |
|---|---|---|
| **-25°_3** | 24.01 ± 0.53 | 0.24 ± 0.08 |
| **-25°_4** | 25.00 ± 0.04 | 0.23 ± 0.06 |
| **-15°_1** | 15.27 ± 0.25 | 0.22 ± 0.07 |
| **-15°_2** | 15.19 ± 1.13 | 0.23 ± 0.04 |

**Figure 45.** Geometric characteristics of the tools tested in the second cutting test.

After the same number of cuts performed in the benchmarking cutting test, the cutting torque were converted into cutting forces and compared with the numerical data in order to validate the numerical model. Rake angle and rake face height are displayed in Figure 45. Each of the values in table was obtained averaging the measures taken from 8 teeth randomly chosen in the saw blade.

### 3.2.3 Cutting force calculation

The procedure presented is valid for all the blades tested because the diameter of the body is always the same and the size of the teeth between one blade and the other does not change to the point of causing a difference in the number of number of teeth engaged in cutting (Figure 46). The calculation of the number of teeth engaged during one cut was done with Matlab taking this ( (65)) as a reference for the kinematic equations (rototranslation). In these equations Rt is the radius of the piece, R the radius of the blade, f the feed of the blade in the piece in mm/s, t is the vector of the times, at the angle between two teeth, n is a value that is called a spinning ratio and represents the rotation speed in revolutions per second of the blade. Table 4 shows the values adopted for the calculations.

$$x_i = R_T + ft - R[1 - \cos(ia - 6nt)]$$
$$y_i = R[1 - \cos(ia - 6nt)]$$

**Table 4** Numerical values included in the formula to calculate the rototranslation of the blade.

| **Data** | Rt [mm] | R [mm] | f [mm/s] | a [rad] | n | t |
|---|---|---|---|---|---|---|
| **Value** | 7.30 | 175 | 15.27 | 0.0524 | 23.97 | Vector from 0 a 1.2 s with 0.002 s step |

The number of teeth engaged (Figure 47) was calculated by summing the number of teeth that in each individual moment were included within the

circumference area represented by the bar. As explained in Figure 47, the teeth are 2 for a short distance in the middle of the bar. On the sides of this short section there is a strong oscillation 2/1 (depending on the timestep chosen) while in input and output from the cut there are two traits in which the tooth is only one (with oscillation depending on the timestep). On a diameter of 17.32 mm there is a tooth engaged for about 6.5 mm and 2 teeth engaged for about 14.6 - 6.5 = 8.1 mm. By averaging a weight between distance and number of teeth in the grip we get about 1.55 teeth engaged in cutting. In addition to the number of teeth engaged, the distance traveled by each individual tooth during a cut can also be calculated. As a first approximation, the profiles obtained from Fig.2 were measured. Qualitatively, it is observed that as the diameter of the cut piece increases, the distance cut by each tooth increases in a non-proportional way (e.g. blade dia. 350 mm, z = 120, Vc 210 m / min, fz = 0.04 mm / tooth rev, bar diameter 17.32 mm → Length cut = 0.03 m; bar diameter 20.28 mm → Length cut = 0.055 mm). This is another reason why cutting small diameters is more critical for TCT sawblades than larger diameters. Finally the unitary cutting force is calculated from experimental motor torque as:

$$Cutting\ force = \frac{Torque}{r_{blade} * z_{engaged} * Tool\ thickness}$$

Where the radius of the blade is 0.175 m, the average number of tooth engaged is 1.55 and the tool thickness in the rake area is 2.7 mm.

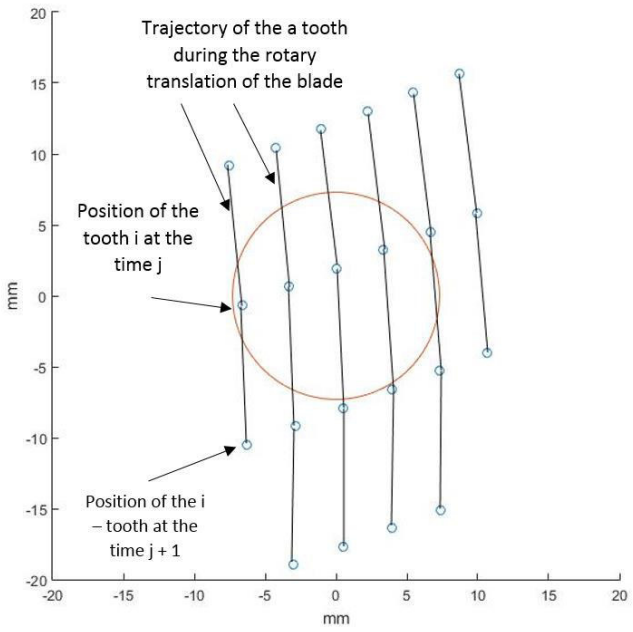


**Figure 46.** Trajectories of a single tooth during cutting.

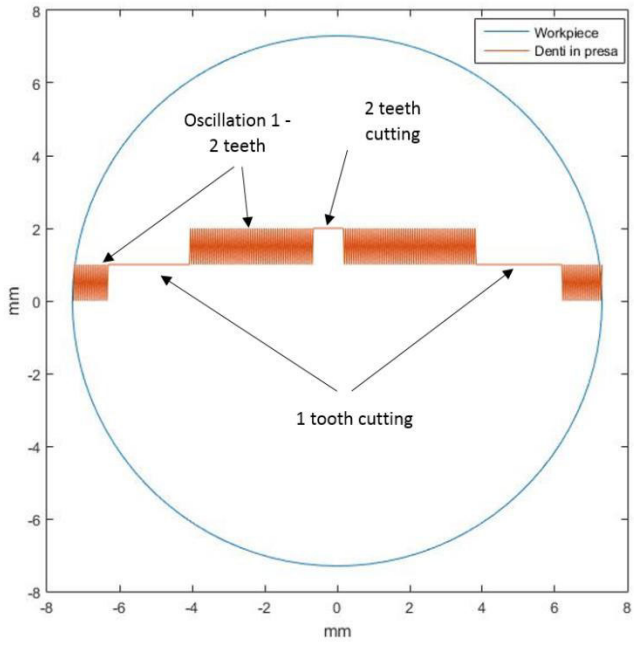


**Figure 47.** Number of engaged teeth when cutting a 17.32 mm bar.

## 3.2.4 Tool wear characterization

Tool wear characterization is of paramount importance to determine tool life, for this reason two different characterization were followed in parallel, one based on quantitative image analysis (from micrographies) and qualitative SEM imaging for wear mechanism identification and another one based on quantitative profilometry. During the whole project two approaches were adopted, 2D wear profilometry and its evolution, 3D image acquisition via multifocal reconstruction of 3D profiles.

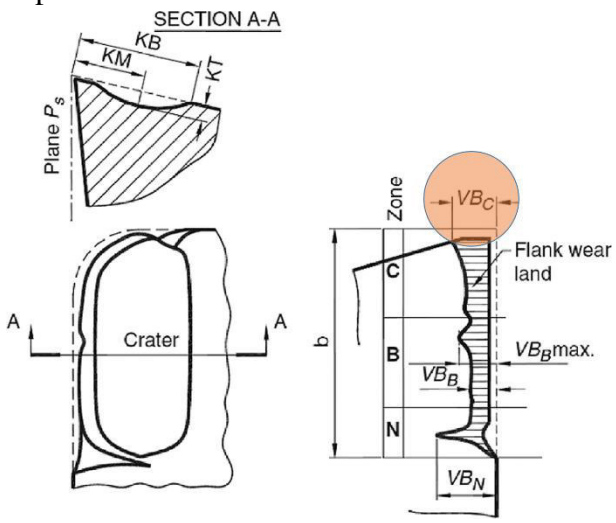


**Figure 48.** VBC measurement according to ISO 8688: 1-1989 **(4).**

Image J software was used for measuring the average value of VB defined by the ISO standard 8688:1:1989 as the average value of the wear scar on the main flank of the cutting tool (Figure 48).

### 3.2.4.1 2D wear profilometry

A MAHR MARSURF CD 120 profilometer was used to probe the blade teeth profile using a 33 mm long WC stylus with tip radius of 3.3 mm (Figure 49). The blade is fixed to a support which allows the tool to rotate if necessary, the probe of the profilometer is put in the initial position and then starts the measurement. The actual measurement starts when the probe starts moving on the surface of the tooth (of a pre – set length); the movement is recorded by a electromechanical sensor and then transferred to video in real time while measuring.

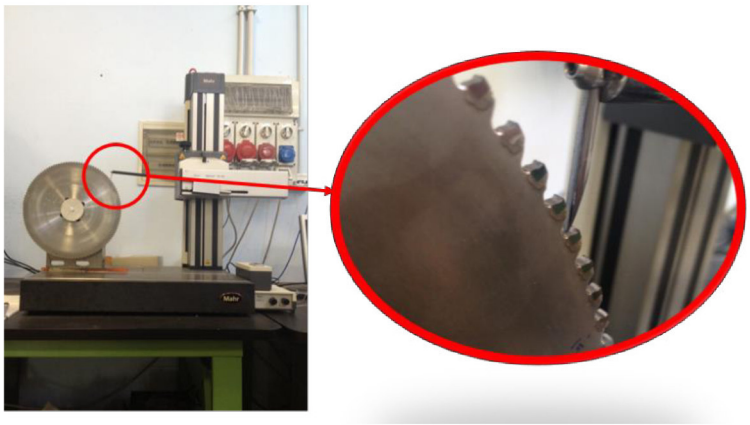

**Figure 49.** Profilometer and detail of the stylus placed in the gullet of a tooth.

The data acquired by this experimental set up were then processed via a Matlab code (Figure 50) to obtain profiles of teeth after cutting tests. The average profile value from 8 teeth was calculated and then new and worn profiles were superimposed to highlight where wear took place. Despite the good results obtained by this method it was used for the first cutting test only because it was sensitive to the position along tooth profile (e.g. craters could lead to misleading conclusions): calculated profiles always had to be compared to optical microscope images.

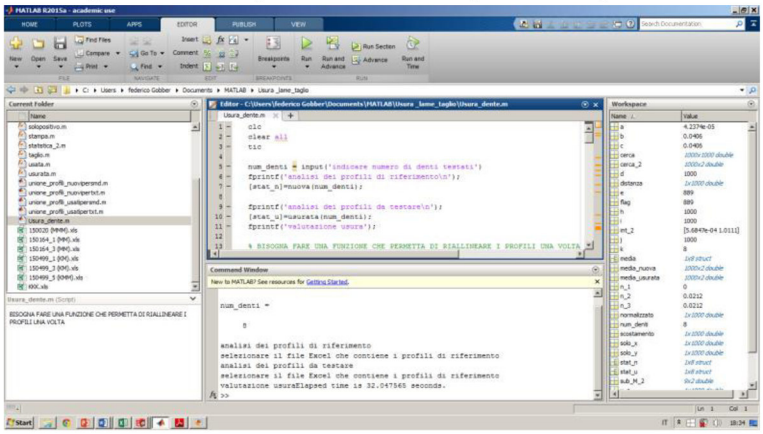

**Figure 50.** Screenshot of the Matlab program named "Profilata" developed for wear assessment.

### 3.2.4.2 3D wear profilometry

An Alicona Infinite Focus SL was used for acquiring the profiles of 8 tooth per tool. The cutting geometry (cutting edge and rake face) was acquired and then processed via two different softwares: GOM v. 7.6 free license and Rhinoceros 5.

With GOM ver 7.6 the profile was imported as a .stl file and then cleaned from noise and errors deriving from the acquisition, in a second step the cutting profile was isolated for both new and worn tool. The superimposed profiles were imported into Rhinoceros for calculating the worn volume. In Figure 51 it is explained how worn volume was calculated using Rhinoceros.

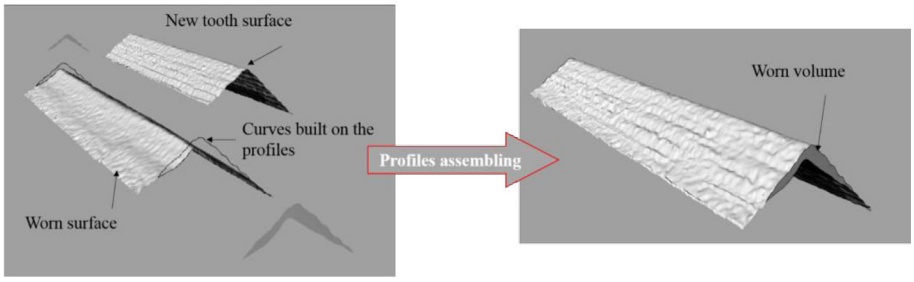


**Figure 51.** Worn volume calculation for cutting tools with Rhinoceros.

## 3.3 FEM simulations

The definition of a new cutting geometry passed through the implementation of a finite element model that could simulate the cutting process and by which it could be possible to estimate the cutting forces. After the first cutting test, different configuration of cutting inserts were simulated numerically via a 2D model for orthogonal cutting; rake angle and the height of the rake face were the two parameters which varied (Figure 52).

| Rake angle | 15 | 15 | 20 | 20 | 25 | 25 |
|---|---|---|---|---|---|---|
| Rake face height | 0.15 | 0.22 | 0.15 | 0.22 | 0.15 | 0.22 |
| Depth of cut | 2,7 mm | 2,7 mm | 2,7 mm | 2,7 mm | 2,7 mm | 2,7 mm |
| Perspective | 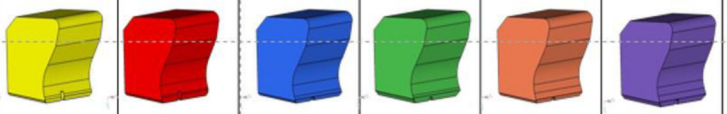 | | | | | |
| Lateral view | 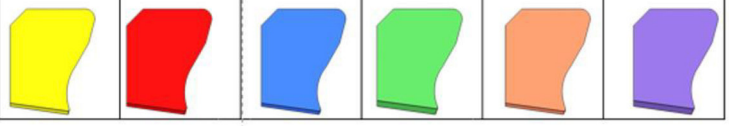 | | | | | |

**Figure 52.** Geometries simulated with Finite Element Modeling of orthogonal cutting.

Inputs for simulation were derived from real geometries:

- Length of cut (LOC): 19 mm
- Tool radius: 175 mm
- Number of teeth: 120

and cutting parameters:

- fz = 0.04 (mm/dente) * giro

- $V_C$ = 210 m/min= 3500 mm/s
- Ω (angular speed) = vt/R = 20rad/sec = 3.18 rps = 191.1 rpm
- $V_F$ (feed velocity) = 15,3 mm/s

The simulation environment adopted was Deform V.11 using AISI 4140 data in Oxley database for flow stress (Figure 53); a specific model calibration was set up (Figure 54), variation of the friction coefficient one iteration after the other was adopted to obtain convergence with the experimental results obtained in the first cutting tests.

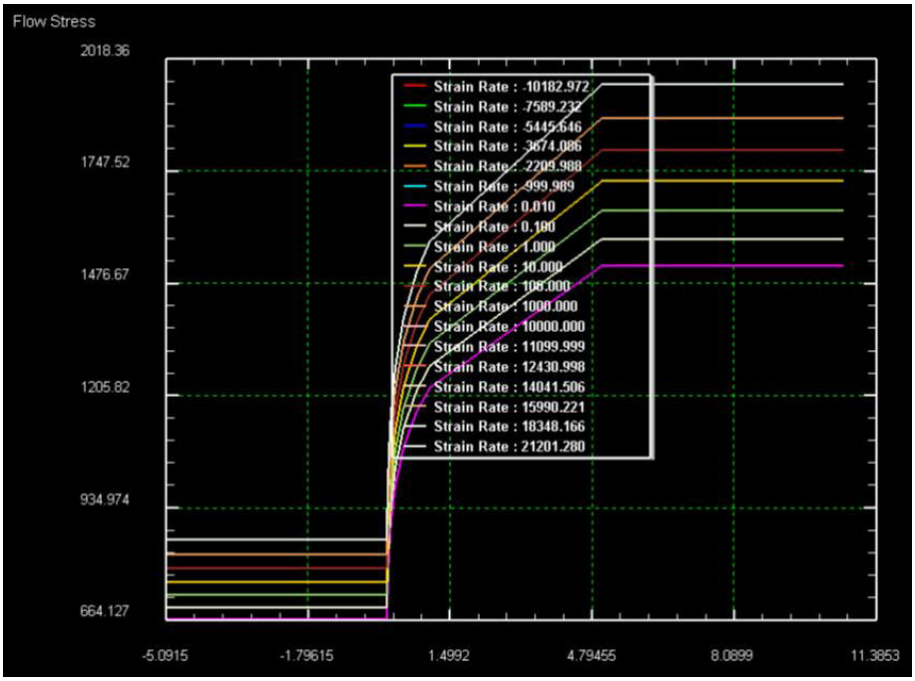


**Figure 53.** Flow stress curves for AISI 4140 in Oxley database **(66)**.

Friction coefficient was the parameter varied between the iterations to reduce the numerical/experimental error. The cutting force for the -25° saw blades calculated after 650 cuts (run in period) was used as the calibration constraint. When the model has been calibrated on the experimental cutting forces it was exploited to simulate the new cutting geometries of Figure 52; the cutting force values were then compared to experimental results obtained from the second cutting test to validate the calibrated model.

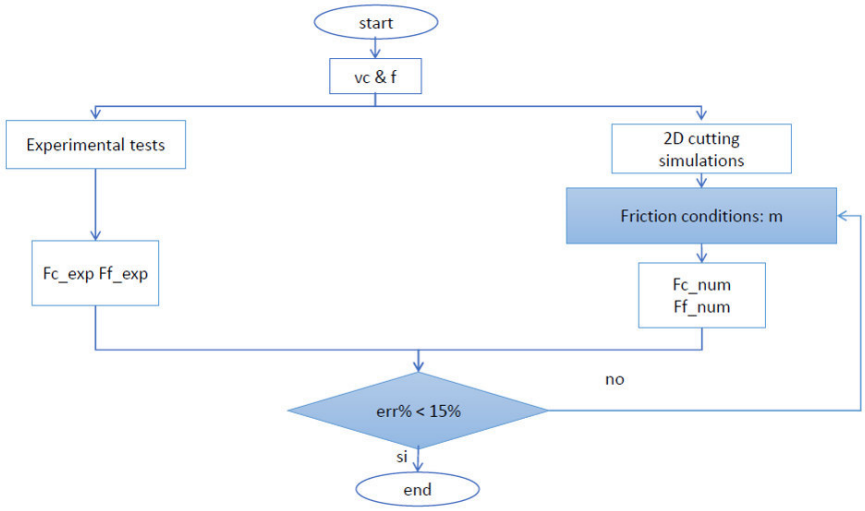


**Figure 54.** Simulation workflow adopted to calibrate the numerical model.

## 3.4 Coating deposition and characterization

### 3.4.1 Substrate preparation

Three different substrate were coated depending on the kind of characterization they were addressed to. The order itself in which the substrates are listed is an index of the level of characterization in a progressive scale up:

- Platelets → basic coating characterization
- Discs → tribological testing
- Saw blades → cutting tests

All these substrates were made of cemented carbide of ISO P20 – 40 grade to ensure the maximum compatibility between the results obtained in at the different levels of characterization (laboratory testing or in plant machining tests). The surface preparation for platelets and discs consisted of surface polishing with cloths and diamond suspension down to $R_a$ 0.1 µm.

### 3.4.2 Coating deposition process

The coating was deposited using a Cathodic Arc Platit PL 2001 (Figure 55) coating unit especially designed for circular saw blades and large tools, with a high loading capacity (up to 800 kg), able to operate at temperatures as high as 500°C, equipped with 4 cathodes: 1 Cr cathode, 2 AlTi 50/50 and one AlTi 63/37. All coatings were deposited with this cathodes configuration.

After surface preparation, in order to obtain a coating with good adhesion, different steps are necessary. Before the deposition of the coating the substrates are cleaned by a ultrasonic machine, in order to prevent the incorporation of dust and oil.


**Figure 55.** Platit PL 2001 CAE - PVD coating unit.

The ultrasonic step has also the function to activate the surface for the deposition. The main steps of the cleaning process are the following:

- Cleaning with ultrasonic
- Rinsing
- Rinsing with water
- Activation with ultrasonic with deionised water
- Rinsing with deionised water
- Preheating and drying under vacuum

After the pre-cleaning process the substrates are transferred, into the PVD chamber, where it undergoes different treatments steps summarized as:

- Evacuation
- Pre-heating
- Ionic etching process
- Coating deposition
- Cooling Down/ Venting

#### *3.4.2.1 Evacuation*

Evacuation of the vacuum chamber removes vapours and gases from the chamber until $10^{-4}$ mbar internal chamber pressure. Consequently, remaining gases, which otherwise would mix with the process gases, are eliminated. Depending on the state of the chamber and the load, such step takes five to ten minutes. Then the heating process can start.

#### 3.4.2.2 Pre-heating

The pre-heating process prevents condensation of water on cold chamber walls. Furthermore the substrates have to be heated up to the appropriate temperature to favour degassing. This takes from one to three hours prior to reaching the temperature set point and a sufficiently clean and high degree of vacuum.

#### 3.4.2.3 Ion etching

In PVD processes, substrate cleaning by ion etching prior to deposition is a key step in achieving good film adhesion, which is essential for all coating applications. Etching with argon or with metal ions is a cleaning process, where thin layers of the substrates surface are removed. Ion etching cleans the surfaces of the substrates and of the substrate holder unit basically by removing off the organic deposits and layers of oxide. Ion bombardment will heat up the substrates very quickly and this, therefore limits the duration of the ion etching process.

The heating and ion etching process is influenced by:

- Arc current, pressure of argon
- Percentage of switch on duration of cathode
- Level of negative bias voltage

#### 3.4.2.4 Coating deposition

The coating cycle starts with:

- Bias voltage adjustment (negative electrical potential applied on substrates from an external source).
- Filling the vacuum chamber with nitrogen to the working pressure required by the process. (Pressure range $1x10^{-3}$ to $5x10^{-2}$ mbar).

The coating process starts immediately after the ion etching with the injection of nitrogen into the vacuum chamber. The temperature of the substrates has to be kept at a constant level. The composition of the coating is controlled by the electrical current of the cathodes arcs, the bias voltage and the gas pressure. The coating cycle is completed when the prescribed electrical current has been transmitted. The deposition time depends on the load of the vacuum chamber and on the required thickness of the coating.

#### 3.4.2.5 Cooling down/venting

Cooling down normally takes place within the vacuum chamber. This part of the process can be accelerated by venting the chamber with nitrogen to approximately 700 mbar.

## 3.5 Coatings

Three AlTiN based coatings were deposited on cemented carbide substrates: two monolayer and a multilayer, all three coating programs were set to produce

coatings with approximatively the same thickness (≈ 4 – 4.5 µm) and an adhesion layer in CrN. In the process of physical deposition from vapor phase by cathodic arc, microdroplets or droplets that consist of portions of the cathode that are transferred to the surface to be coated, create inhomogeneities in the coating. They are mainly produced during the switching on and off of the cathode (67). There are solutions, for example deposition systems equipped with magnetic filters, otherwise it is possible to optimize the parameters of the deposition process, in particular pressure in the chamber and currents, to reduce the quantities and the dimensions of these defects (68). The microdroplets and craters lead to a significant increase in the roughness of the coating, up to about 4-5 times compared to that of the substrate. Some droplets extend for the entire thickness of the coating, creating critical defects as they are prone to detachment and able to leave the substrate uncovered. The monolayer coatings deposited are characterized by the same coating architecture and differ only for the cathode current: 125A or 80A. The reason for depositing two monolayer coatings with different cathode currents was oriented towards the decrease of surface defectiveness (droplets) as indicated in literature. From a preliminary assessment of inserts surfaces coated at 125 A in fact the situation reported in Figure 56 was observed.

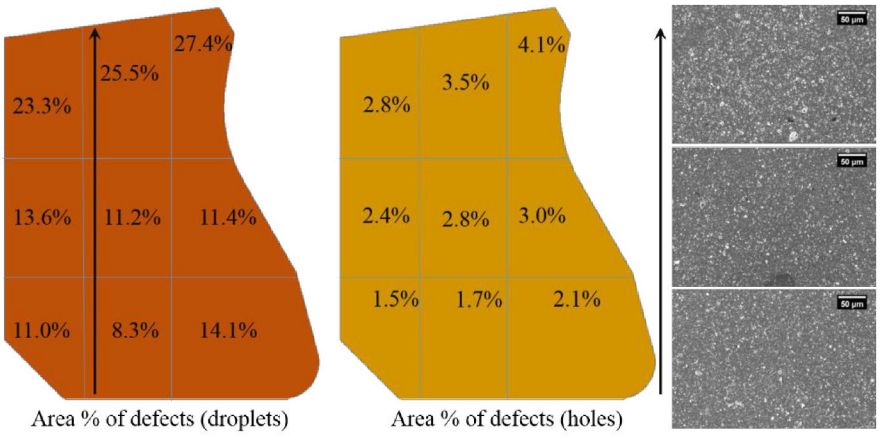


**Figure 56.** Defect fraction on the flank of tool inserts.

A high percentage of the surface is covered with droplets and there is a tendency as the density of defects increases approaching the higher part of the insert: just the one engaged in cutting. This is reasonable since the upper part of the insert is the closest to the cathodes and thus receives first the evaporated particles and macro particles. The objective of lowering the current was diminishing the fraction of defects. On the other side the multilayer was deposited focused on increasing toughness for higher adhesion and wear resistance (Figure 57).

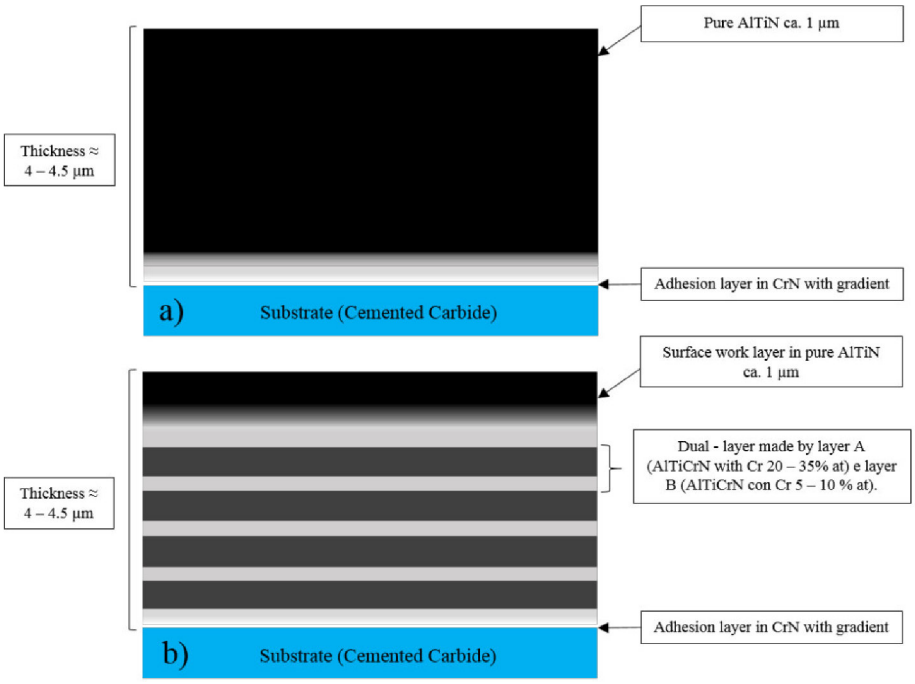


**Figure 57.** Coatings architecture, a) monolayer coatings, b) multilayer coating.

The multilayer coatings architecture can be divided in an inner and an outer portion. The inner portion of the coating is constituted by alternating layers, having the first layer a composition richer in chromium and the second layer a composition richer in Aluminium and Titanium. The outer portion of the coating is a top layer with uniform composition, its stechiometric formula being $Al_{0.55}Ti_{0.45}N$. Furthermore a single layer of Cr is deposited directly on the substrate before starting to deposit the real coating architecture so as to enhance the adhesion between the substrate and the coating. Finally the adhesion layer is completed by a gradient layer of CrAlTiN when all cathodes are turned on at the same time with increasing current.

Table 5 shows the deposition parameters for all coatings realized, where $Gas_{Et}$ is the gas for etching, $P_0$ is the chamber pressure previous to the deposition, $Gas_{Dep}$ is gas during the deposition process and P is the pressure during deposition. A more detailed description of the deposition parameters adopted for the multilayer is given in Table 6.

**Table 5.** Deposition paramters for coatings analyzed.

| **Coating** | **AlTiN 125A** | **AlTiN 80 A** | **AlTiN Multilayer (AlTiN/CrN)** |
|---|---|---|---|
| **$Gas_{Etching}$** | Ar | Ar | Ar |
| **$P_0$ [mbar]** | $10^{-4}$ | $10^{-4}$ | $10^{-4}$ |
| **Cathodes** | Cr 100%, 2 AlTi 50/50, 1 AlTi 63/37 | | |
| **Current [A]** | 125 A | 80 A | 125 A |
| **$Gas_{Dep}$** | $N_2$ | $N_2$ | $N_2$ |
| **P [mbar]** | $5 * 10^{-2}$ | $5 * 10^{-2}$ | $5 * 10^{-2}$ |
| **Bias [V]** | 20 | 20 | 20 |

**Table 6.** Detailed deposition parameters for AlTiN/CrN multilayer coating.

| | Cr_cathode [A] | AlTi 50/50_cathode [A] | AlTi 50/50_cathode [A] | AlTi 60/40_cathode [A] | Bias [V] |
|---|---|---|---|---|---|
| **Adhesion** | 130 | 0 | 0 | 0 | 75 |
| **Gradient** | 110 | 110 | 110 | 110 | 100 |
| **AlTiCrN** | 110 | 120 | 120 | 120 | 20 |
| **Gradient** | 70 | 125 | 125 | 125 | 20 |
| **AlTiCrN** | 70 | 125 | 125 | 125 | 20 |
| **Gradient** | 110 | 100 | 100 | 100 | 20 |
| **AlTiCrN** | 110 | 100 | 100 | 100 | 20 |
| **Gradient** | 0 | 125 | 125 | 125 | 20 |
| **AlTiN** | 0 | 125 | 125 | 125 | 20 |

### 3.5.1 Morphological observation

Both surfaces and cross sections of coatings were observed by SEM (surface) and FESEM (cross section) to analyze surface defectiveness grade

### 3.5.2 Statistical defect characterization

In the current work the analysis of number and dimension of pin-holes was realized through the use of an image analyzer software, Image J. For every coating, 10 images at 1000x magnification were taken through SEM and submitted to image analysis following a similar procedure to that applied for WC grain measurement (Figure 58).

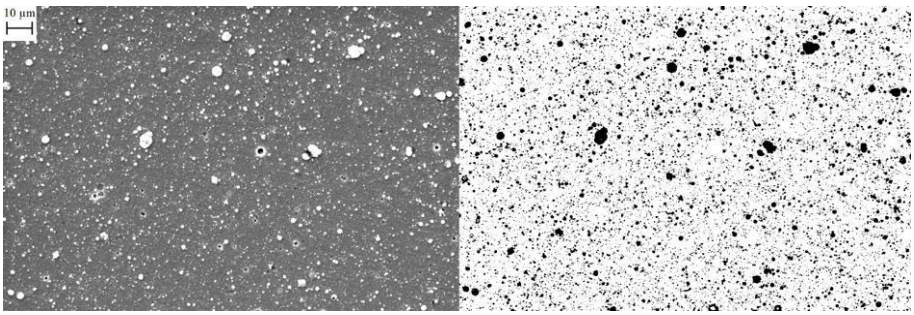


**Figure 58.** Image binarization for droplets counting.

### 3.5.3 Adhesion test

The indention Rockwell-C or Mercedes test (performed with EMCO TEST M4U ) was applied to assess the adhesion of the coating substrate (69). The coating substrate adhesion was evaluated on the basis of the presence, amount and extension of coating detachments surrounding the indentation. The resistance to propagation

of the crack along the interface is then used as a measure of the adhesion. The result is obtained classifying the adhesion with different levels, from HF1 to HF8, according to the amount of cracking or coating delamination around the indent. Figure 59 shows the adhesion classification. Only indentations classified as HF1, HF2 and HF3 correspond to acceptable adhesion. This type of classification applies only to the indentations with a load of 150N are used.

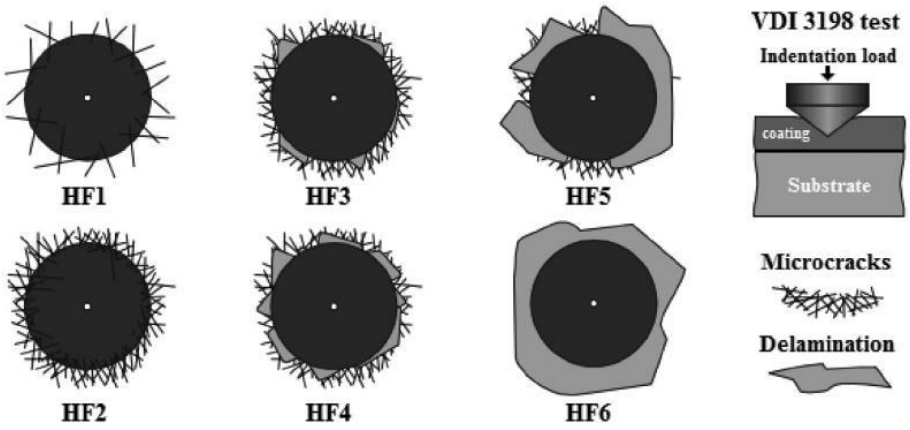


**Figure 59.** Rockwell C adhesion test schematic.

The test makes the assumption that the interface is the weak point in the coating-substrate system, resulting in adhesive failure under load. When the fracture occurs within the coating or substrate itself then cohesive failure has occurred and it may be concluded that the interface is at least as tough as the weaker of the film or substrate.

### 3.5.4 Nanohardness nanomodulus and nanoscratch

Several methods exist for the determination of thin film material properties (at the nano-scale), but most rely on separation of the films from the substrate, and subsequent analysis of individual films (or individual film analysis before depositing the layer) . These methods are impractical on engineering surfaces, as surface films are unknown and cannot be removed for analysis purposes. A technique known as nano-indentation was developed to solve these issues.

Nano-indentation is based on a material resistance to permanent plastic deformation. This technique presses an extremely sharp, hard tip into a surface, under a certain, prescribed load. Through examination of the tip load and displacement data, a material hardness and reduced elastic modulus can be calculated. This technique allows one to examine thin film material properties on very complex surfaces, without having to separate and examine each layer individually. The differences between this test and the meso/micro testare that the tip geometry and loads are much smaller, and the corresponding indentations/penetrations are in the nanometer scale.

Nanoindentations and nanoscratched were carried out with an Hysitron instrument (TI 950 TriboIndenter) present at IIT@polito, A Berkovich tip (used for all the tests) is a 3-sided pyramid with an included angle of 142.3°, where the angle

from the normal to a face is 65.35°. The Hysitron Berkovich tip is intended for deeper nano-indentation penetrations. A load of 5000 μN with a rate of 200 μN/s was applied for each coating, 5 indentations were performed. The maximum load indentation is applied for 2 s. Hardness and Young modulus were calculated by the indenter software using the Oliver and Pharr Method based on the unloading curve, as described below.

Oliver and Pharr (70) analyzed the load-displacement data and developed equations for calculating two important material properties, hardness (H) and reduced elastic modulus (Er), using:

$$E_r = 2S\sqrt{\frac{\pi}{A}} \qquad H = \frac{P_{max}}{A}$$

where the tip contact area, A, is a function of the contact depth derived from the tip area calibration equation, S and $P_{max}$ are constants defined a priori, while Er is the reduced elastic modulus given by:

$$\frac{1}{E_r} = \frac{(1-\nu^2)}{E} + \frac{(1-\nu^2{}_i)}{E_i}$$

E and n are the elastic modulus and Poisson's ratio of the specimen, while $E_i$ and $n_i$ are material constants for the indenter tip. This equation assumes that the deflection of the tip is zero, which is a reasonable assumption since the diamond tip is extremely rigid, with $E_i$=1,140 GPa and $\nu_i$=0.07, respectively.

The nanoscratch test was performed with the same Berkovitch shape tip and gradually increasing the load up to 1000 mN or 5000 mN along a length of 1 mm. Three scratches were made for each load and each coating in order to assess their adhesion. The scratch test technique consists in creating a scratch on the test sample obtained with a diamond tip, this is guided on the surface with increasing constant load. Once the critical load has been reached, the surface is scratched, at another value the film starts to break and at a third value it yields completely. The critical loads are detected in a very precise way thanks to the observation with the incorporated optical/electronical microscope, in this way the adhesion properties of different film / substrate combinations can be quantified. The scratch testers measure the applied normal force, the tangential force (friction) and the penetration thickness. Friction force along the scratch was acquired and compared to the images of scratches.

Three load values are commonly define in scratch tests to characterize coating adhesion:

- LC1 Critical Load 1: vertical load for which cracks appear at the side of the track. It is generally not noted.
- LC2 Critical Load 2: vertical load for which delamination of the coating on the side of the track occurs. It must always be noted and if it is not identified, the test must be repeated with a higher final load.

- LC3 Critical Load 3: vertical load for which the substrate appears. An increase in the progress of the identifier is observed and the trace becomes very clear at the center.

# Chapter 4

# Cemented carbide characterization

## 4.1 Composition and microstructure

From XRD analysis it is evident that the only phases present in the samples are those related to binder and carbides, no deleterious eta – phase was found . Eta – phase can be harmful for cutting application since its presence causes a detriment of the mechanical properties. The XRD confirmed the different nature of K15 which is a single (plain) cemented carbide with respect to M20, P35 and P40 which are cemented carbides with secondary carbides (TiC/TaC) whose characteristic peaks are highlighted by red arrows in Figure 60.

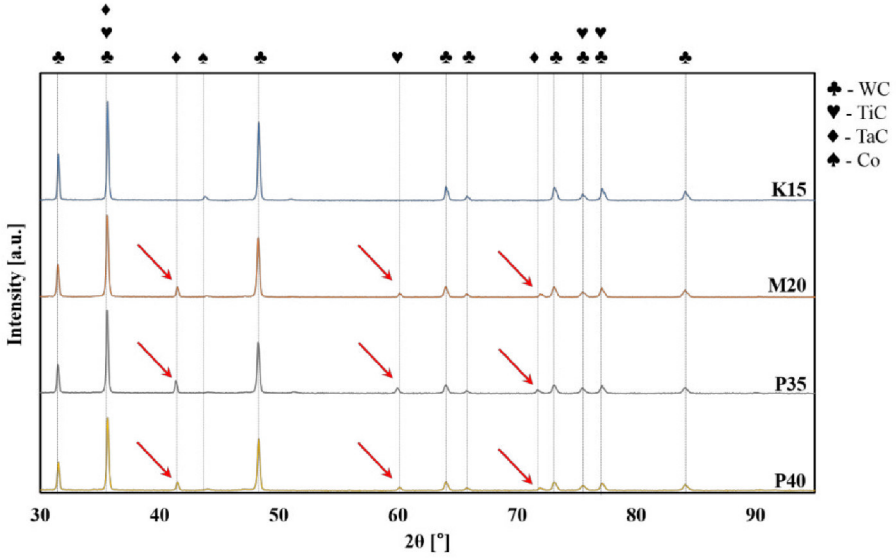


**Figure 60.** XRD analysis of four classes of cemented carbides.

In Figure 61 an example of the results obtained from image binarization is reported for each grade of cemented carbide. The procedure followed was successful in isolating the WC grains from the SEM images. Detailed single grains are appreciable in Figure 61, this fact enhance confidence in the results obtained from image analysis. The measured values of average size confirm the greater fineness of the ISO K15 grade carbide grains compared to the other three grades. Due to the greater fineness, a higher number of grains was measured with the same number of images analyzed, a larger area is also occupied by them. On the other hand, the P40 grade is the one with the coarser size of the WC grains. It should be noted that secondary carbides are present in interesting quantities only in the qualities M20, P35 and P40 and that they are not considered in the count carried

out. Their shape appears more rounded and their dimension is comparable to that of WC primary carbides. K15 is a submicrometric (extrafine) grain sized carbide while all the others are micrometric (fine) carbide grains.

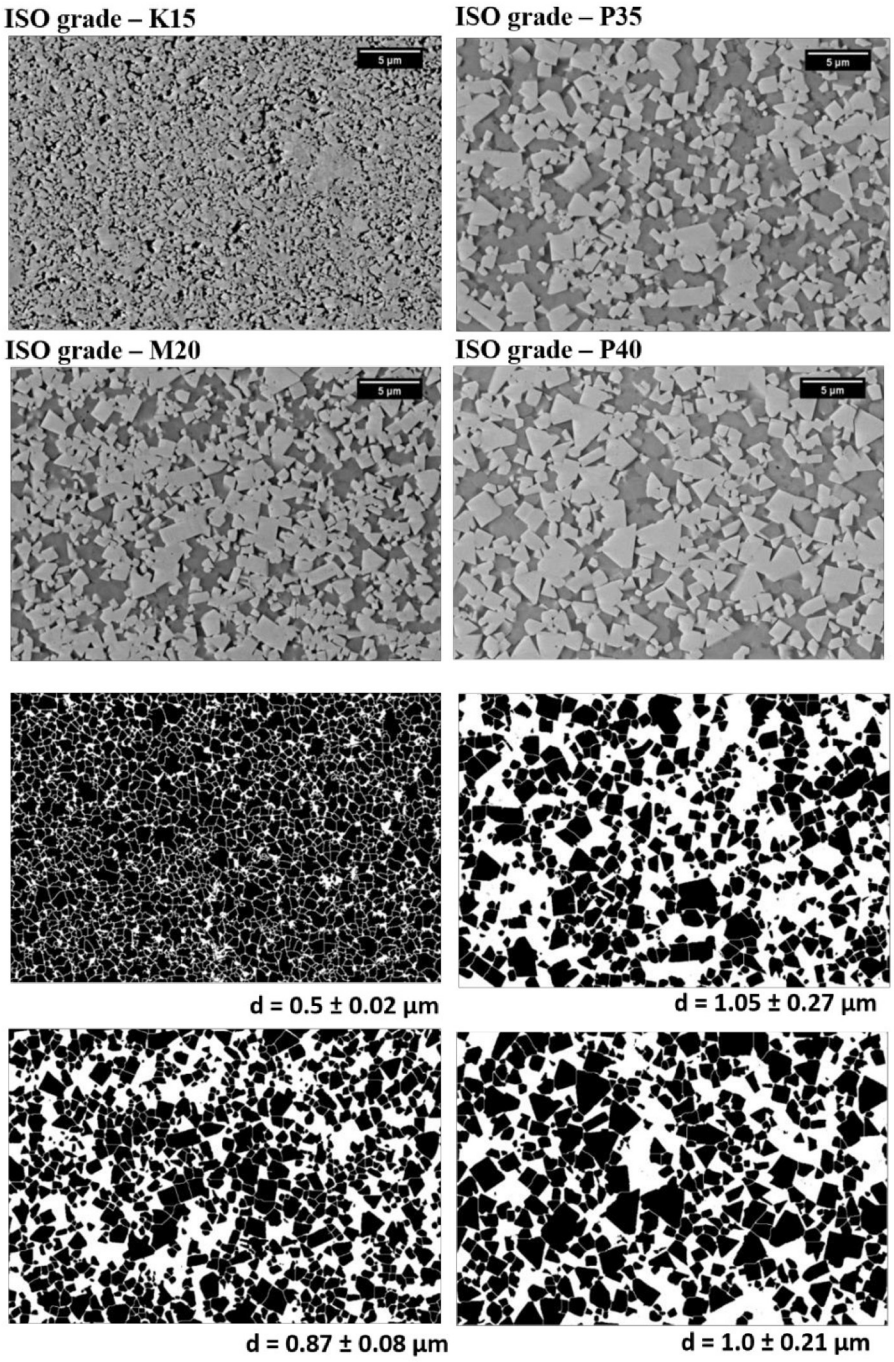


**Figure 61.** SEM images and their binarization empoyed for grain size measurement.

The granulometric distribution (Figure 62), put in histograms, reveals to be asymmetric for all grades, this can be explained with the presence of different classes of grain sizes mixed together during the production of cemented carbides. In powder metallurgy in fact, this is a standard practice, mixing powders with different granulometry in order to obtain the maximum packing and thus the maximum density after sintering (Hot Isostatic Pressing in this case). Anyway K15

results to have the narrowest distribution, very centered around its statistical mode (red arrow).

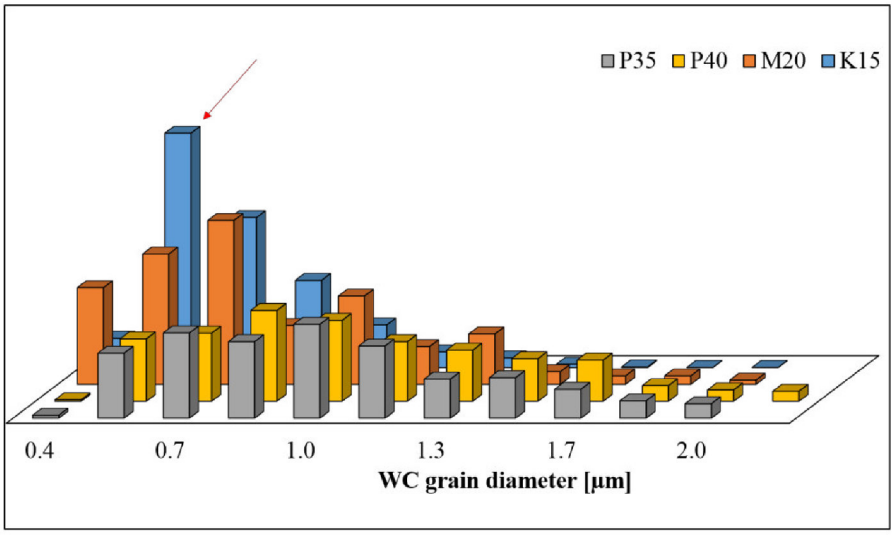


**Figure 62.** Grain size distribution histogram for the four classes of cemented carbides analyzed.

The mean free path in the binder, that is, the distance occupied by the cobalt binding between carbide grains, is instead greater for hard metals with larger grains and, in particular, for those with a higher percentage of cobalt. The M20 type hard metal, having a reduced quantity of binding cobalt and medium sized grains, has a fairly low mean free path, but still greater than that of the K15 type. According to the results of the tests reported in literature, a greater free mean path allows obtaining hard metals with a less fragile and more tenacious behavior, with a better wear behavior (19).

The free medium path in the binder is an important parameter for the mechanical properties of the hard metals as it allows to have the possibility to predict with greater safety, at least in the first analysis, their fatigue behavior. Materials with a high mean free path will in fact have more ductile behaviors, vice versa, with a reduced mean free path, they will show a more fragile behavior, with easy triggering of cracks in the points where the carbides are spaced out by too little binding. The actual influences of this will be observable following the tribometric test, discussed below. In the literature it is reported in many studies (3), (20), (19), (16) as, with the same quantity of binder, larger size of the grains tend to confer less material hardness but higher wear resistance. What tendentially against intuitive. It can therefore be said that the resistance to wear, is generally considered proportional to the ratio between the grain size and the amount of binder (19). From the observation of the values of binder free mean path in Table 7 the measured values suggest that the type of cemented carbide with better wear behavior should be the P40, followed by M20 and P35 approximately on equal merit, K15 is in fact on the last position. These considerations are valid in the first analysis, as it must be taken into account that the presence of secondary carbides tends to increase wear resistance especially at high temperatures (15).

**Table 7.** Microstructural properties of the four grades of cemented carbides analyzed

| | Grain size [µm] | Grain size definition | Density [g/cm$^3$] | Binder mean free path_λ [µm] |
|---|---|---|---|---|
| **K15** | 0.5 ± 0.02 | Ultrafine | 14.48 | 0.14 |
| **M20** | 1.05 ± 0.27 | Fine | 13.2 | 0.27 |
| **P35** | 0.87 ± 0.08 | Fine | 12.5 | 0.36 |
| **P40** | 1.0 ± 0.21 | Fine | 12.9 | 0.39 |

## 4.2 Hardness and toughness

Five indentations per sample were done to mitigate measure errors. The images of the $HV_{30}$ indents made by on the cemented carbide samples, respectively K15, M20, P35 and P40 (Figure 63), were then observed by metallographic microscope to have the maximum measurement accuracy.

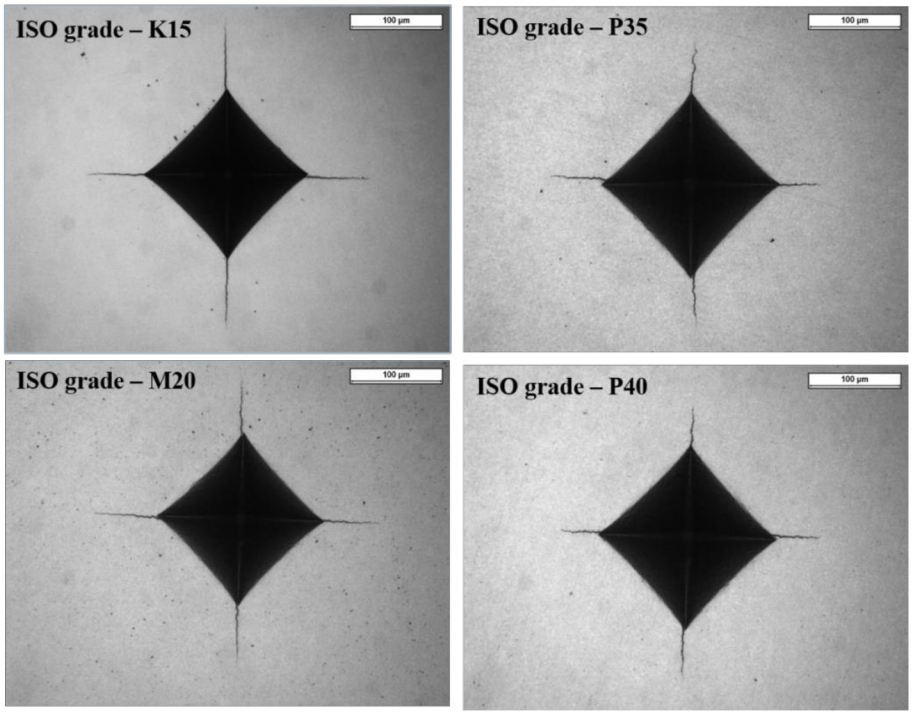


**Figure 63** HV30 indentation for measurement of hardness and toughness of cemented carbides grades.

The measurement of the indent diagonals was carried out using the ImageJ software for image analysis. By measuring the cracks originated at the apexes of the impression and the formula derived from the Palmqvist cracks model (63) it was also possible to calculate the toughness of the indented hard metals. The results of the measurement of hardness and toughness calculations, derived from the indentations are reported in Figure 64.

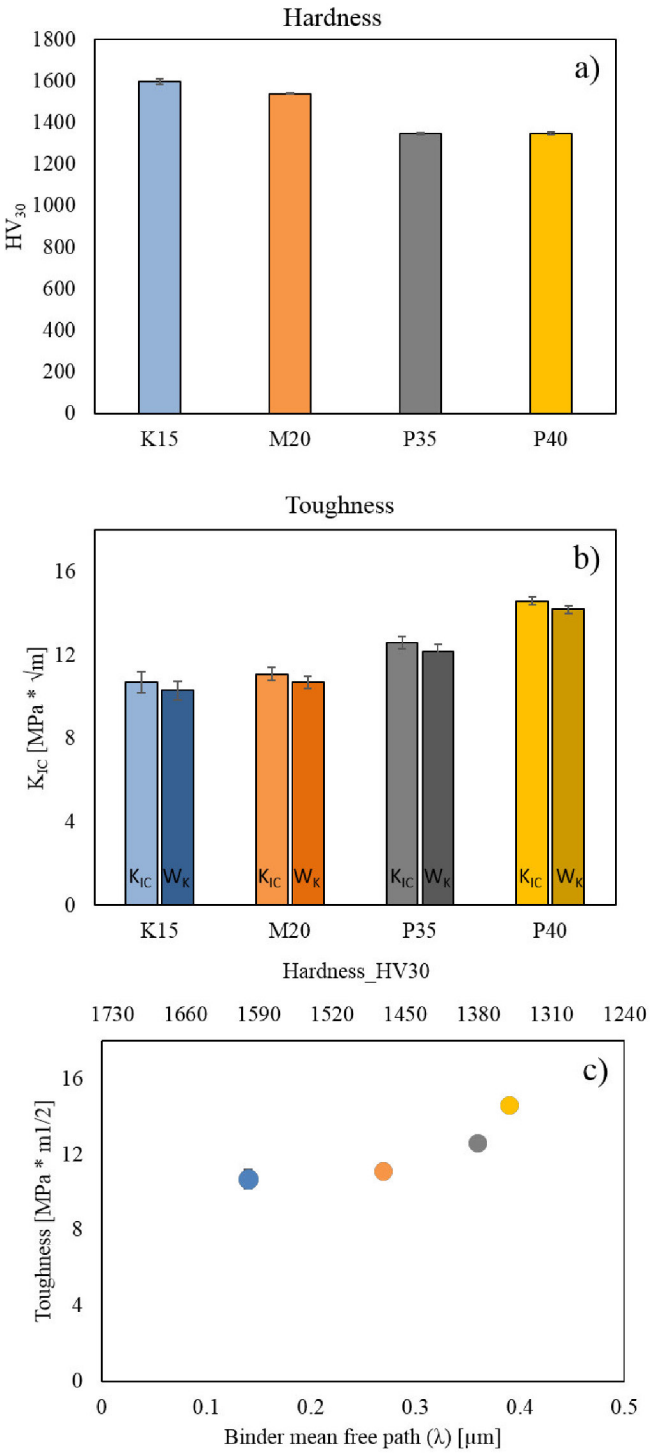


**Figure 64.** a) Hardness HV_30 and b) toughness for the four classes analysed.In c) microstructural and mechanical properties were reported in a single graph.

Hardness and toughness have an opposite behavior as expected (Figure 64a) and b)), higher hardness values correspond to lower toughness grades, furthermore a direct relation exists between cobalt binder volume fraction, grain size and toughness as shown in Figure 65. A higher cobalt binder volume fraction is directly related to a higher binder mean free path. In Figure 64 c the interaction between cobalt binder mean free path, hardness and toughness is presented, the results

obtained from hardness and toughness measurements coincide with literature. K15 despite having the maximum volumic percentage of cobalt binder (≈ 16%) is the only fine grain grade, M20 among the three medium grades has the lowest volumic percentage of cobalt binder (≈ 11%) while P35 and P40 have respectively ≈ 14% and ≈ 15% cobalt binder in volume. These data match with literature ones as can be seen in Figure 64b).

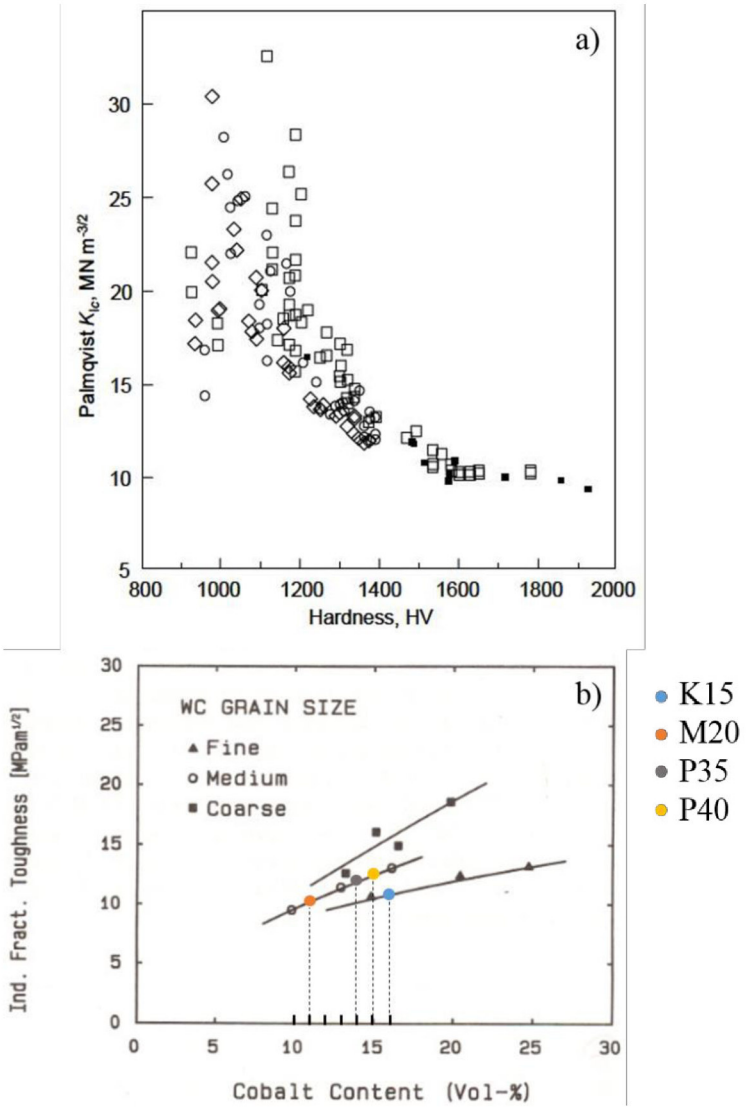


**Figure 65.** Experimental relationship between Hardness and toughness for cemented carbides of different grain size **(27),** b) experimental relationship between binder content, and toughness for different WC – Co grain sizes **(25).**

K15 has the highest volume fraction of binder but its fine grained structure reduces toughness due to the low mean free path, the lowest among all the grades considered. M20 has very similar hardness/toughness properties if compared to K15 but the fraction of secondary carbides and a lower fraction of cobalt binder make its properties different under other aspect, wear resistance for example. P35 and P40 are very similar, the main difference is in the quantity of cobalt binder that in fact plays a major role in determining the hardness/toughness relation.

## 4.3 Cracks morphology

Crack lengths for determining toughness were measured from optical microscope images, anyway these cannot give a sufficient detail for understanding cracking mechanisms, whether it is transgranular or passing through the binder, or along grain boundaries. SEM imaging confirms the different behavior documented by optical microscopy (Figure 66). All images were put aside starting from the apex of the indent, so all cracks are compared at the same length. Despite the volume fraction of binder, highest for K15 grade, these images contribute to highlight the primary role that grain size has in crack propagation resistance for cemented carbides.

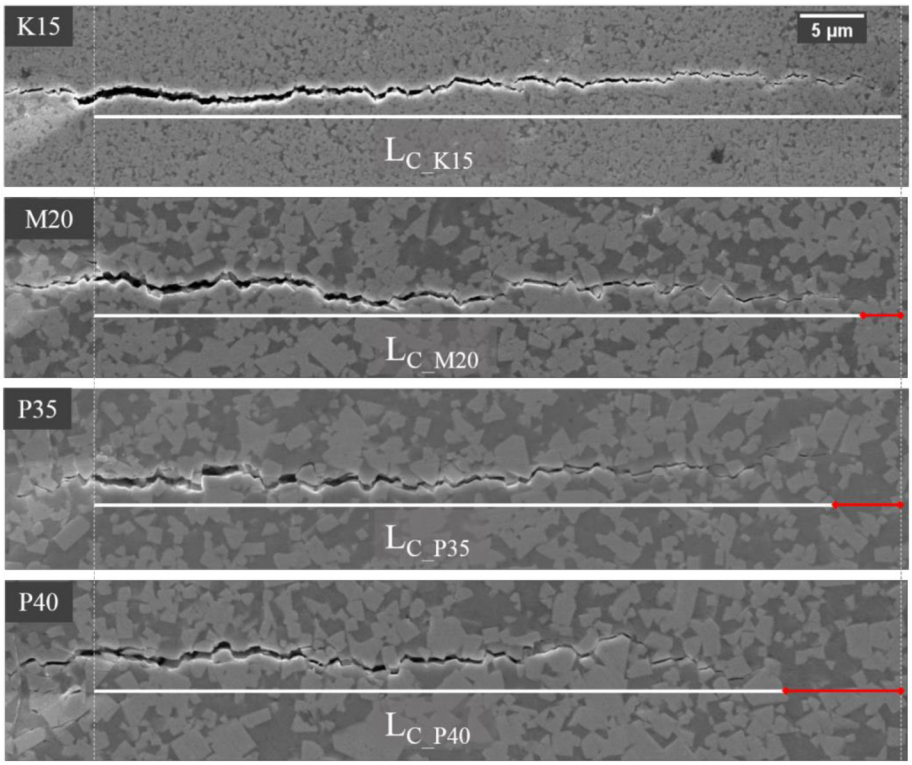


**Figure 66.** SEM images of cracks originating from Vickers indenter apexes, LC is the crack length while the red line represents the portion of solid material.

From a higher magnification (Figure 67) at the crack tips, distinctive features of crack propagations can be highlighted. In plain grade low grain sized K15 the crack is mainly passing through the cobalt binder, it is difficult to observe fractured WC grains. Mixed carbide grade on the opposite have several crack propagation mechanisms acting together, it is supposed that this fact can be due to a more uniform balance of toughness inside the cemented carbide.

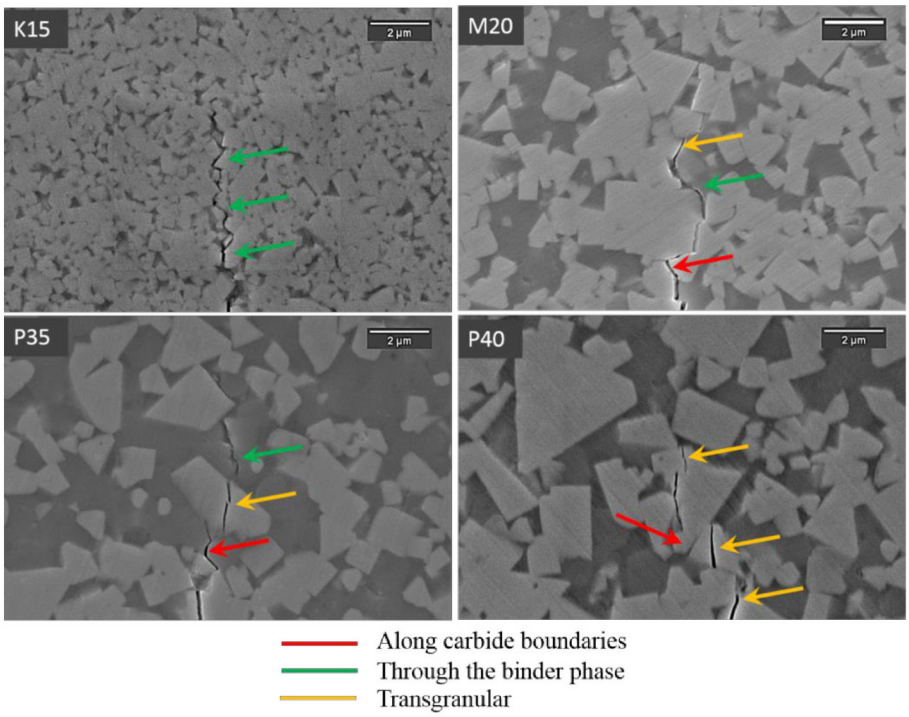


**Figure 67.** SEM images of crack propagation mechanisms in cemented carbides.

## 4.4 Sliding wear resistance

### 4.4.1 Coefficient of friction and temperature behavior against AISI 4140 and AISI 660

The tribological tests, for each grade of cemented carbide, were carried out with pins in stainless steel AISI 660 and pins in tempered steel AISI 4140 (42 CrMo4). From the tribological test (Figure 68) we obtained the graphs of the instantaneous dynamic friction coefficient measured by the tribometer and the values of the temperature measured at the point of contact between pin and disk by thermal camera during the various tests. The temperature and friction coefficient values are very similar for each quality of analyzed carbide, for each type of pin used, respectively in stainless steel AISI 660 and in tempered steel AISI 4140 being the thermal conductivity of materials very similar. An interesting difference between the tests carried out with different pins results in the presence of a peak, in the case of the coupling with AISI 4140 steel pins, in the curve of the coefficient of friction accompanied by a thermal peak, measured at the beginning of the test (less than 500 m). For the discs coupled with the pins in AISI 660 the peak of the coefficient of friction is not as marked as for AISI 4140, even if the presence of a thermal peak has been measured. The thermal peak is therefore linked to the conformation of the two contact surfaces, present in the tests of both qualities of pins, while the coefficient of friction is given by the oxidation of the steel adhered on the track, for this reason it was not detected in the test carried out between hard metal and stainless steel pins (19). It is necessary to remember, observing the curves with increasing temperature trend, that the experimental apparatus itself undergoes an

inevitable heating during each test due to the dissipation of heat deriving from the friction between the surfaces in contact. However, the average friction coefficients and average temperatures proved to be quite similar in the test conditions adopted, with both pin materials.

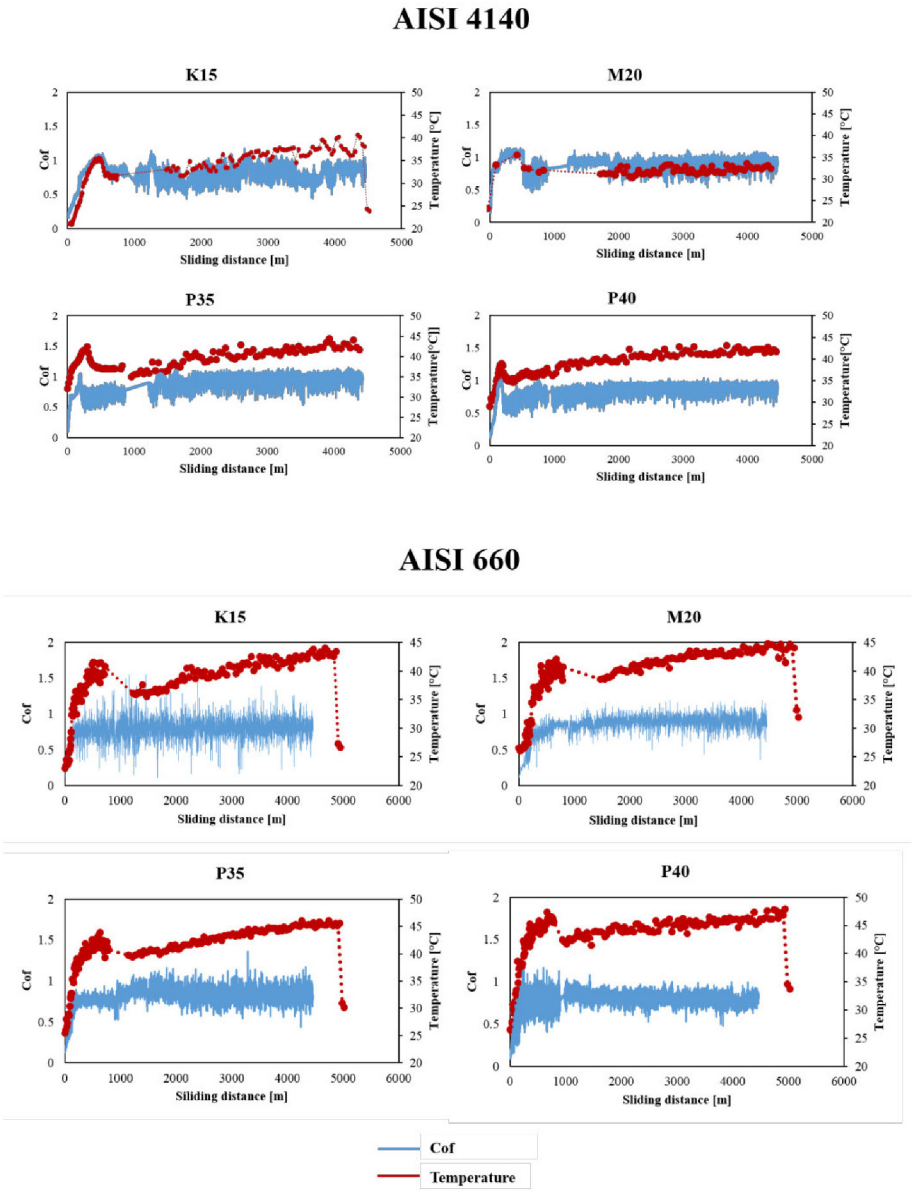


**Figure 68.** Trends in the dynamic friction coefficient and the temperature at the contact point obtained from the thermal imaging camera compared to the sliding distance (total effective distance 5000m) for all cemented carbides grades against AISI 4140 and AISI 660.

## 4.4.2 Wear loss measurement

At the end of the tribological pin-on-disc test, traces of wear and adhered material are present on cemented carbide discs and a conspicuous consumption of the steel pins caps were observed, for both steels (Figure 69). From the comparison of wear of the pins in the two different materials it is evident that it is greater in the case for stainless steel. Increased wear occurred in spite of the greater hardness presented by AISI 660 stainless steel, 36 ± 1 HRC, compared to AISI 4140 tempered steel, 27 ± 2 HRC.

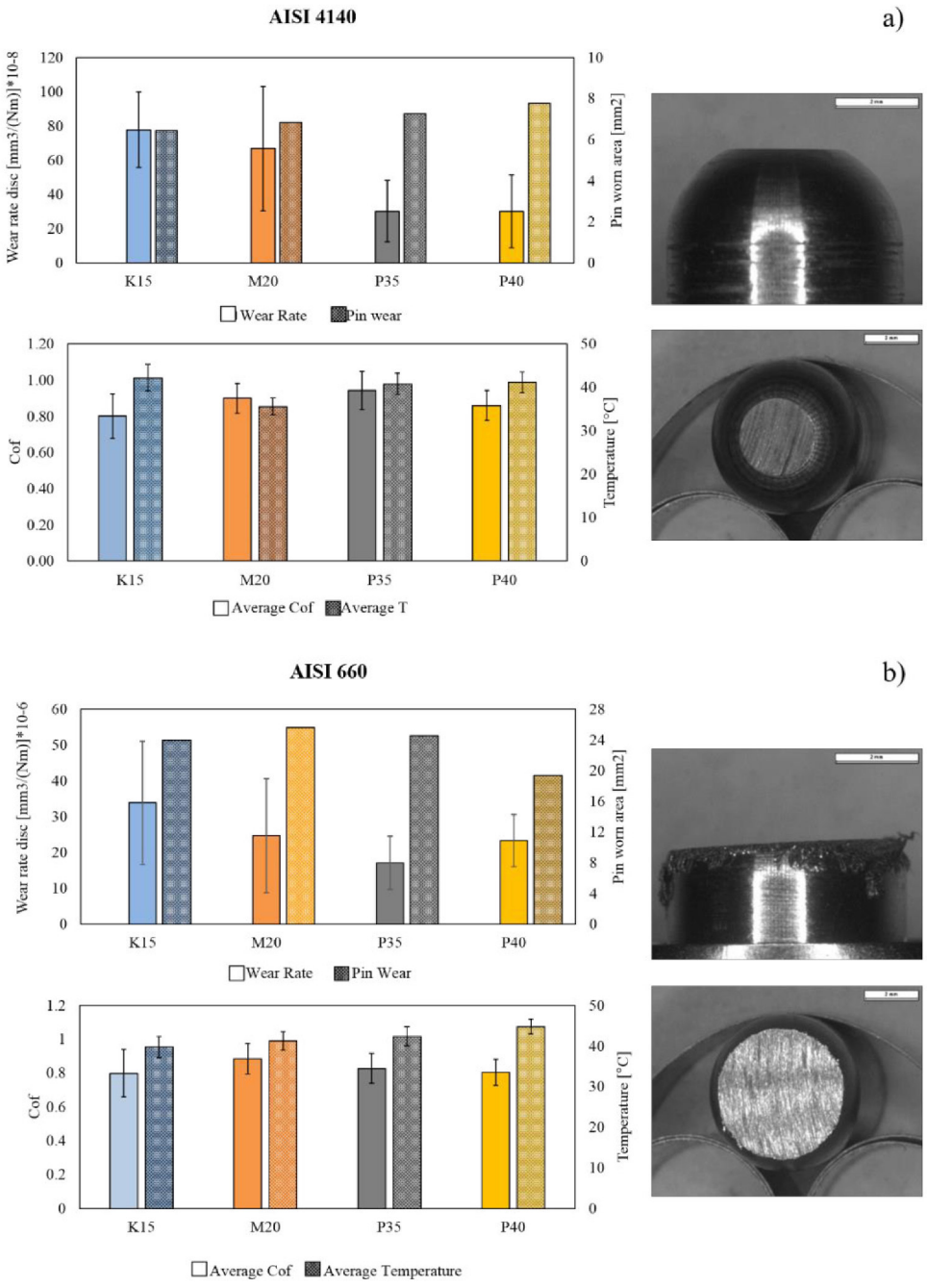


**Figure 69.** Wear quantification for pins and discs. a) results from pin on disc tests against AISI 4140, b) results from pin on disc tests against AISI 660.

Despite a very low level of wear for the cemented carbide discs, which was predictable, the higher toughness grades P35 – 40 show lower wear rate against both steel grades if compared to K15 and M20. Moreover, there are two degree of magnitude in wear against AISI 4140 and against AISI 660, this can be due to different wear mechanisms acting on the surface of cemented carbide when a ferritic steel or an austenitic alloy is sliding on its surface.

### 4.4.3 Wear mechanisms of K15 and P40 when sliding against AISI 4140 and AISI 660

The surface of the two samples that gave opposite results were compared by SEM and FESEM imaging to characterize the behavior of such materials when sliding against a ferritic or an austenitic alloy. The two alloys, are characterized by different microstructures and crystal lattice (BCC VS FCC), this last point above all determines mechanical properties of the alloys and their deformation mechanics. Austenitic alloys (AISI 660) have an FCC structure and are typically ductile, this characteristic is transposed also in cutting mechanisms where tensile properties plays a major role. Ferritic alloys such as AISI 4140 have a BCC structure with lower ductility. These characteristics can be found observing the wear tracks on cemented carbide discs (Figure 70): the pin made of austenitic alloy gives a broader wear track on the disc (and the pin itself is subject to higher wear), a thick layer of adhered material is observable in Figure 71 while this is not true for the ferritic alloy, AISI 4140, characterized by lower wear on both the worn surface of the pin and on the disc one.

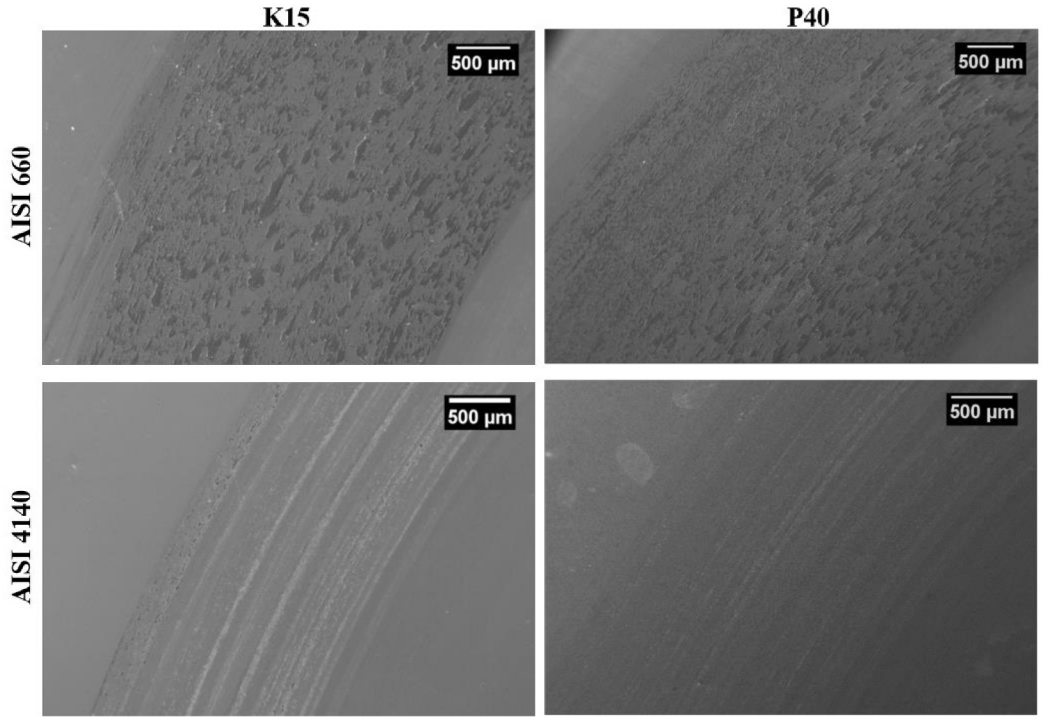


**Figure 70.** SEM images of the wear tracks at low magnification.

Wear debris have a different morphology, larger particles covering the surface are visible for AISI 660. The elongated shape derives from the detachment and subsequent plastic deformation of the fragments that due to their high plasticity and thermal resistance can deform and stretch. Wear debris generated from the AISI 4140 pin are smaller and resemble powders: this is due to a higher fragmentation of the particles detached during sliding. From EDS analysis it was observed a higher

oxygen content on the surface of debris deriving from AISI 4140 pin, this is another indication that the combined action of lower ductility and oxidation contributed to make the adhered material very fragile in the case of AISI 4140 thus generating very fine debris. Indications of differences in the wear mechanisms acting on cemented carbides surface appears at higher magnification.

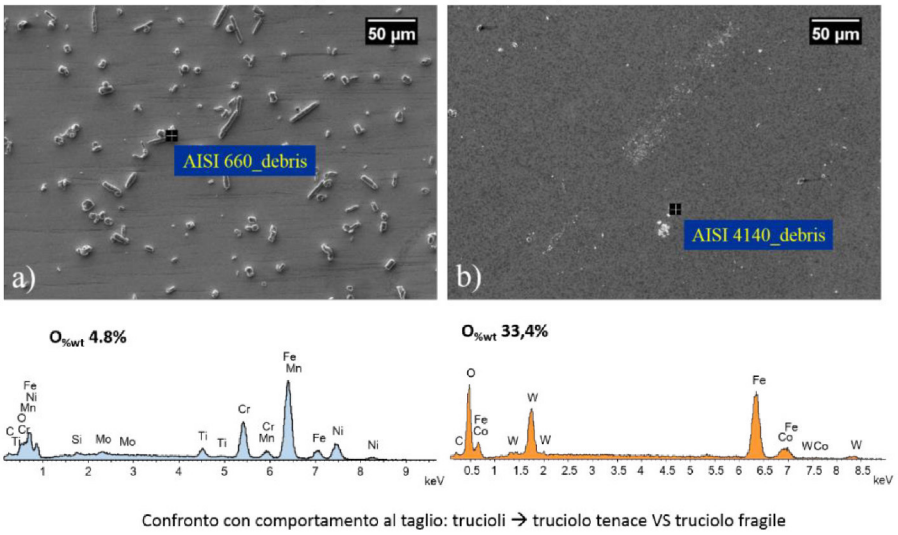


**Figure 71.** Wear debris observed aside the wear track, a) debris from AISI 660 and b) debris from AISI 4140 on the surface of cemented carbide disc.

Both grades are characterized by abrasion grooves when coupled with AISI 4140 pins, this can be ascribed to the high sliding speed that favors abrasive wear and to the generation of a three body contact including oxidized wear debris. More pronounced differences in wear tracks are evident from the images in Figure 72 where cemented carbide discs were coupled with AISI 660: K15 grade exhibits craterization while the surface of the P40 grade is covered by what at this magnification can be defined as vacancies.

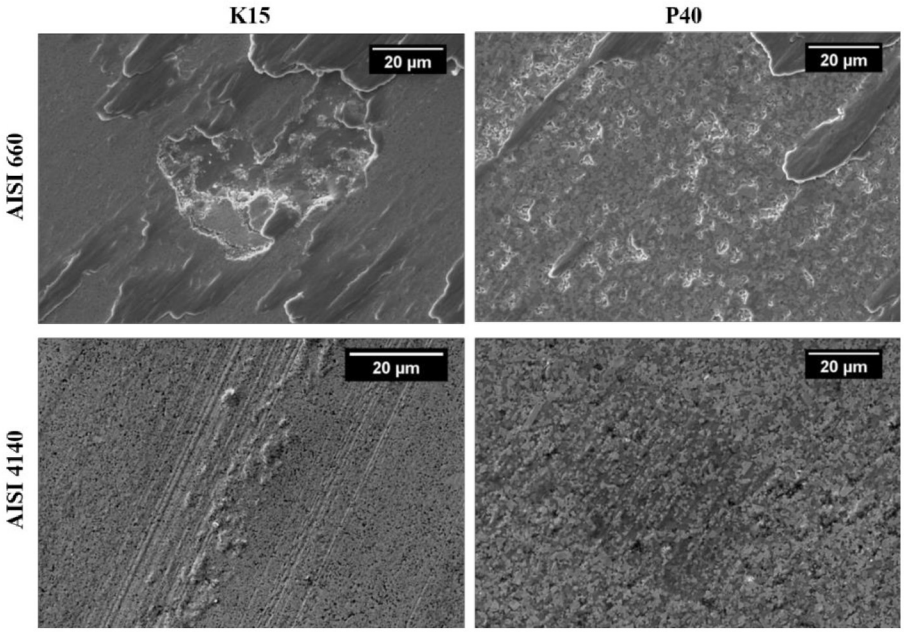


**Figure 72.** SEM images of the wear tracks at higher magnification, to highlight wear.

At higher magnification a discontinuous tribolayer is observed on the surface of AISI 4140 coupled samples, this tribolayer covers the surface of both samples (Figure 73) with higher adhesion in the inter grain spaces where higher fraction of binder is concentrated (white arrows).

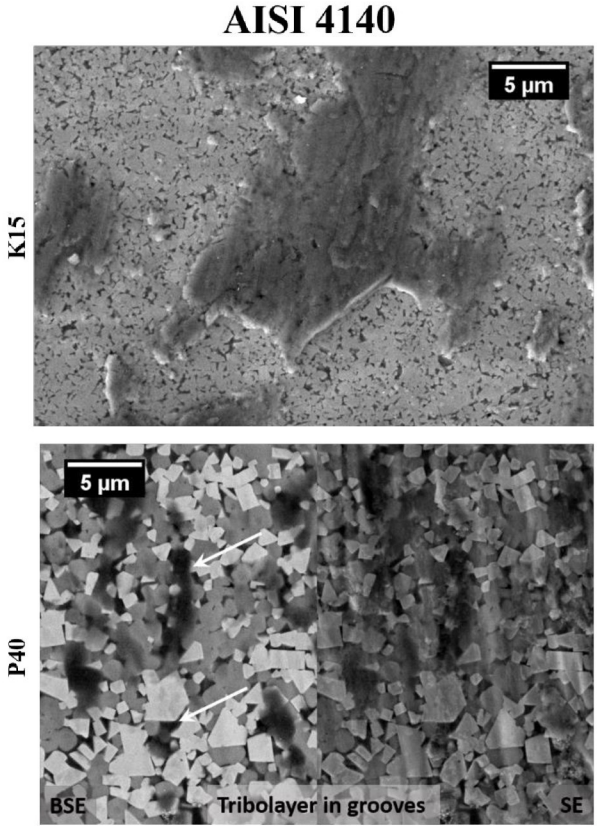


**Figure 73.** FESEM images of the surface of cemented carbide samples tested against pins made of AISI 4140.

The tribolayer produced by AISI 660 is way thicker than that produced by AISI 4140 whose thickness was not observable at the same magnification (Figure 73, Figure 74). The tribolayer on the surface of K15 grade is well adhered, the white arrow in Figure 74 indicates the detachment of the adhered layer but it has to be noticed how the underlying layers (tribolayer) remain attached to the cemented carbide that can subsequently stratify on the surface of the tribolayer (dark blue arrow). The different behavior observed at lower magnifications for P40 grade is more evident here (Figure 74): the surface of the sample is free from that tightly adhered tribolayer present on the surface of K15 grade and indicated by the dark blue arrow. The surface of the sample anyway is rough with carbides that have been pulled out from the surface thus leaving those vacancies observed for P40 in Figure 72.

The high degree of adhesion of AISI 660 on the surface of K15 sample allowed the observation of the cross – section of the tribolayer. From (Figure 75 a) three areas were identified with different colours: the K15 substrate (green), the tribolayer (yellow) and the adhered layer (red). At higher magnification (Figure 75 b) carbides appear to be extracted from the matrix, partially crushed and

incorporated in the steel thus composing this thick and solid tribolayer, very closely bound to the substrate.

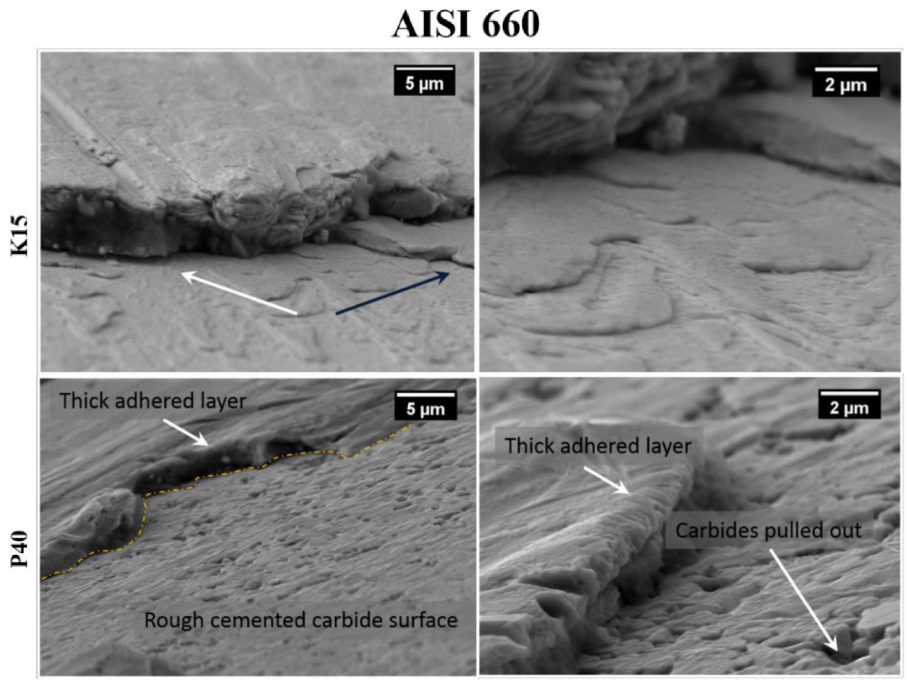


**Figure 74.** FESEM images of the surface of cemented carbide samples tested against pins made of AISI 660.

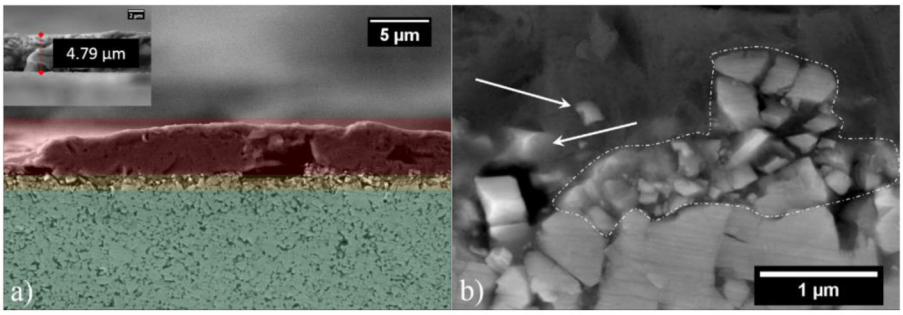


**Figure 75.**FESEM images of cross – section of the tribolayer on the sample K15 against AISI 4140. a) lower magnification image, b) higher magnification detail of the interface.

A similar tribolayer was not observable on the cross – section of P40 sample, in fact during metallographic preparation the lower degree of adhesion favoured the detachment of portion of the adhered layer. This supposition is confirmed by the regularity of the exposed edge of the sample (Figure 76). No crushing, and incorporation of carbides was observed, it is supposed that when adhesion between the pin and the disc takes place on P40 cemented carbide grade, this is merely due to the interaction between the binder and austenitic alloy.

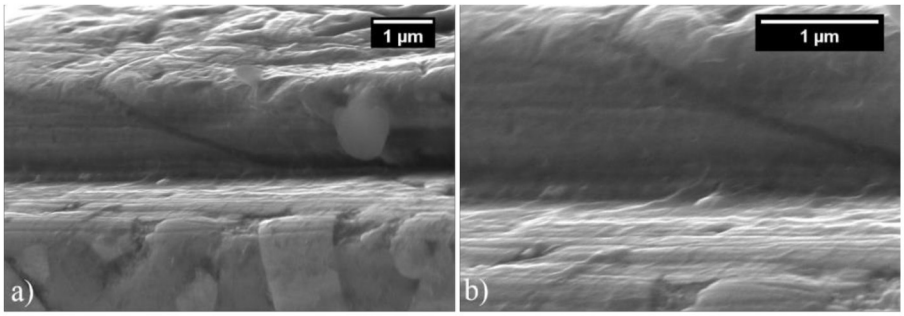


**Figure 76. F**ESEM images of cross – section of the tribolayer on the sample P40 against AISI 4140. a) lower magnification image, b) higher magnification detail of the interface.

On the surface of K15 grade against AISI 660 the are macro spallings of portions of cemented carbide (Figure 77). The observed spallings are visible from portions of tribolayer that detached from the surface. From the cracks visible in Figure 77 b it is assumed that the progressive sliding of the pin on the cemented carbide surface has induced a mixed mechanism of adhesive wear and surface fatigue (from which cracks were generated). The continuous and very fast loading of the pin sliding on the disc surface, coupled to the lowest level of toughness measured among the cemented carbides tested had caused the nucleation of cracks and the progressive detachment of portions of material in correspondence of previous defects such as micro porosities or surface irregularities.

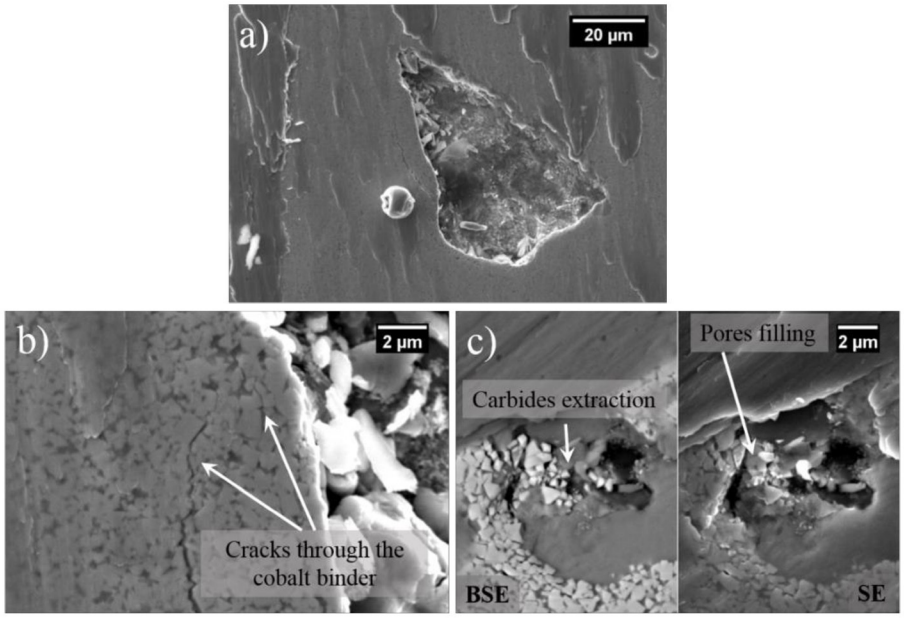


**Figure 77.**SEM images of spalling defects originated on the surface of K15 sample sliding against AISI 660. a) large spalling, b) cracks propagating aside of a spall, c) extraction of carbides from the edges of a defect and filling of the pore generated.

A schematic is proposed to resume the wear mechanisms identified on the surface of cemented carbides under sliding wear conditions (Figure 78).

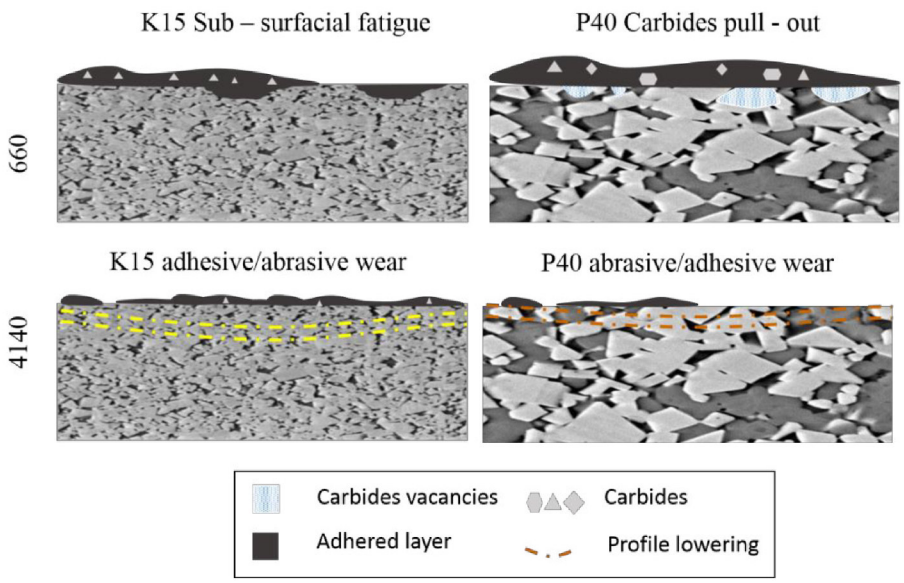


**Figure 78.** Schematization of wear mechanisms observed for K15 and P40 cemented carbide grades when sliding against a ferritic (AISI 4140) or an austenitic (AISI 660) steel.

# Chapter 5

# Tool design and cutting tests

## 5.1 Benchmark cutting tests

The first cutting tests had the objective of characterizing both cutting force (via cutting torque) and vibrations at increasing cutting speeds. The two sets of blades tested had negative rake angle because this configuration is the most conservative against the risk of edge chipping and early failure. The two sets of blades tested highlighted that tool vibrations decrease at increasing cutting speed, this is due to a stiffening mechanism that acts on the blade that by rotating at high speed gets more tensioned by the centrifuge force and thus becomes more rigid. The cutting speed of 210 m/min was finally chosen as the objective speed because of the high production rate guaranteed and for the low level of vibration induced (Figure 79). A variation of the rake angle has an important return on cutting torque: increasing the number of cuts emphasizes the differences between a -25° rake angle and a -30° rake angle. After 2350 cuts a gap of ≈ 30 Nm was observed which is directly related to how wear has acted on the surface of the tool Figure 79.

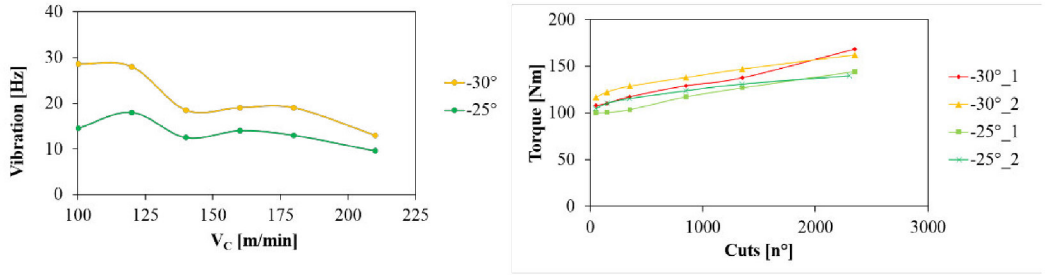


**Figure 79.** Cutting vibrations as a function of cutting speed, and cutting torque at 210 m/min as a function of the number of cuts.

The condition of the tools is in fact very different after 2350 cuts at 210 m/min (Figure 80). Despite common abrasive/adhesive wear on the flank and on the rake of the cemented carbide insert, a strong comb cracking and subsequent cratering occurred on the rake face of the tools with $\gamma = -30°$, which might be caused by high temperatures developed on the rake face when the chip slides on it during chip formation. It is important to notice the geometry named “chip breaker” and its position: direct reference to it will be made in the Tool wear mechanism paragraph.

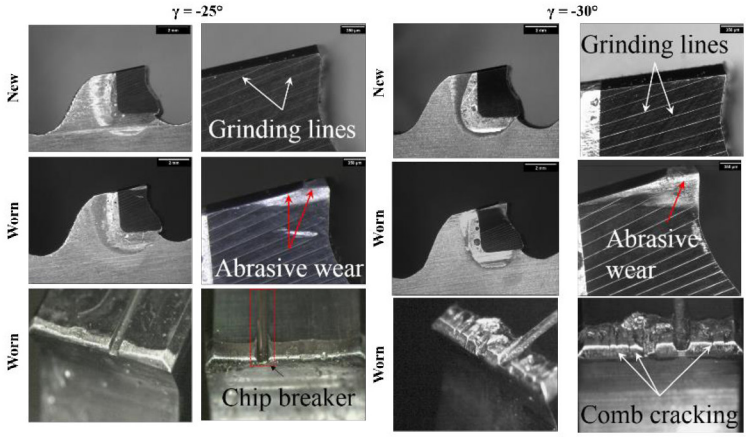


**Figure 80.** Micrographs of the new and worn tools with -25° and -30° rake angle at the end of the cutting test.

2D profiles obtained from 8 teeth per blade were averaged and then superimposed to the averaged 8 new profiles. Cratering on the flank of the insert was highlighted from 2D profilometry analysis for the γ = -30° tools (Figure 81) while a more uniform and reduced wear was detected on the γ = -25° flanks.

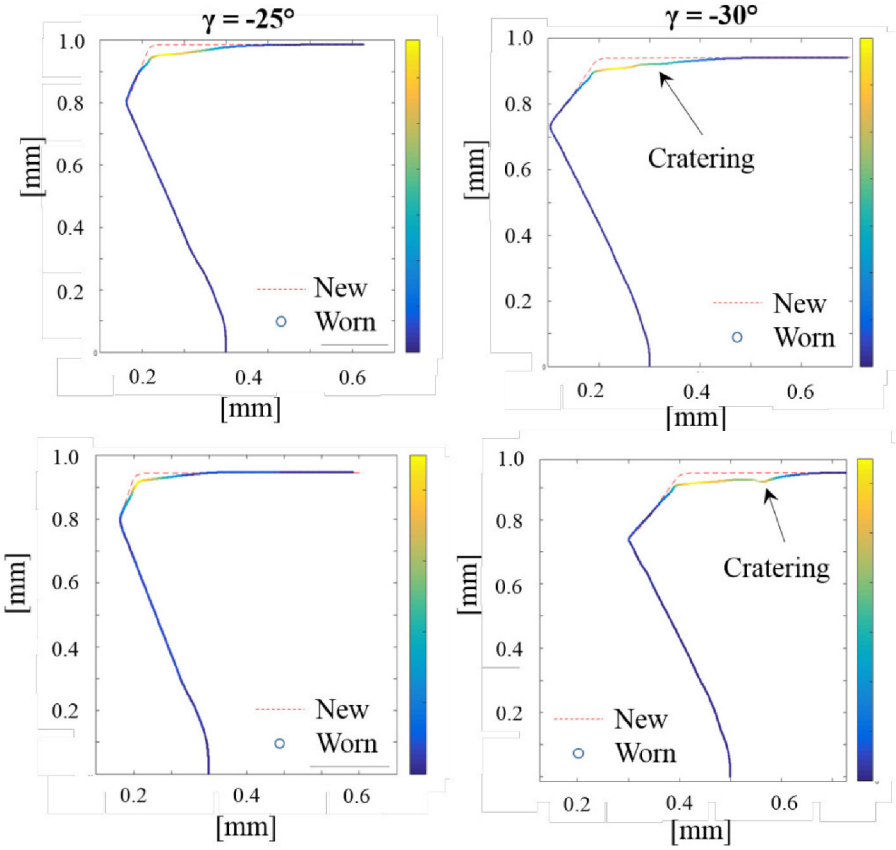


**Figure 81.** 2D profilometry of the tested blades.

The average cutting torque after 650 cuts at 210 m/min was 110 ± 2 Nm. Considering 1.55 teeth engaged, 0.175 mm blade diameter and 2.7 mm of depth of cut, the value of 150 ± 1.5 N was calculated as the target cutting force for FEM calibration.

## 5.2 FEM simulation of alternative cutting geometries

After several simulation trials, the model was calibrated with 0.6 as coefficient of friction. This value does not have to be confused with the coefficient of friction measured by tribological testing. In pin on disc testing in fact the contact is non lubricated while the cutting tool is always lubricated during machining to reduce wear and prevent early chip seizuring and build up edge formation. In the next paragraphs the most significant results from finite element modeling relative to cutting force, tool tip temperature and stress/strain state on the chip will be presented and discussed. The unit or unitary cutting force from simulation is the component of the cutting force along the x – axis, this force will be considered as the real cutting force, in fact thrust force has a low weight in determining the resultant cutting force that is the one measured experimentally. The unitary cutting force calculated from numerical simulations of -15° rake angle cutting tool is comprised between 135 and 136 N (Figure 82); for -20° rake angle it is comprised between 142 and 143 N (Figure 83); for -15° rake angle is comprised between 150 and 152 N (Figure 84). The values oscillate depending on the rake height: the higher cutting force is always related to the higher rake face height.

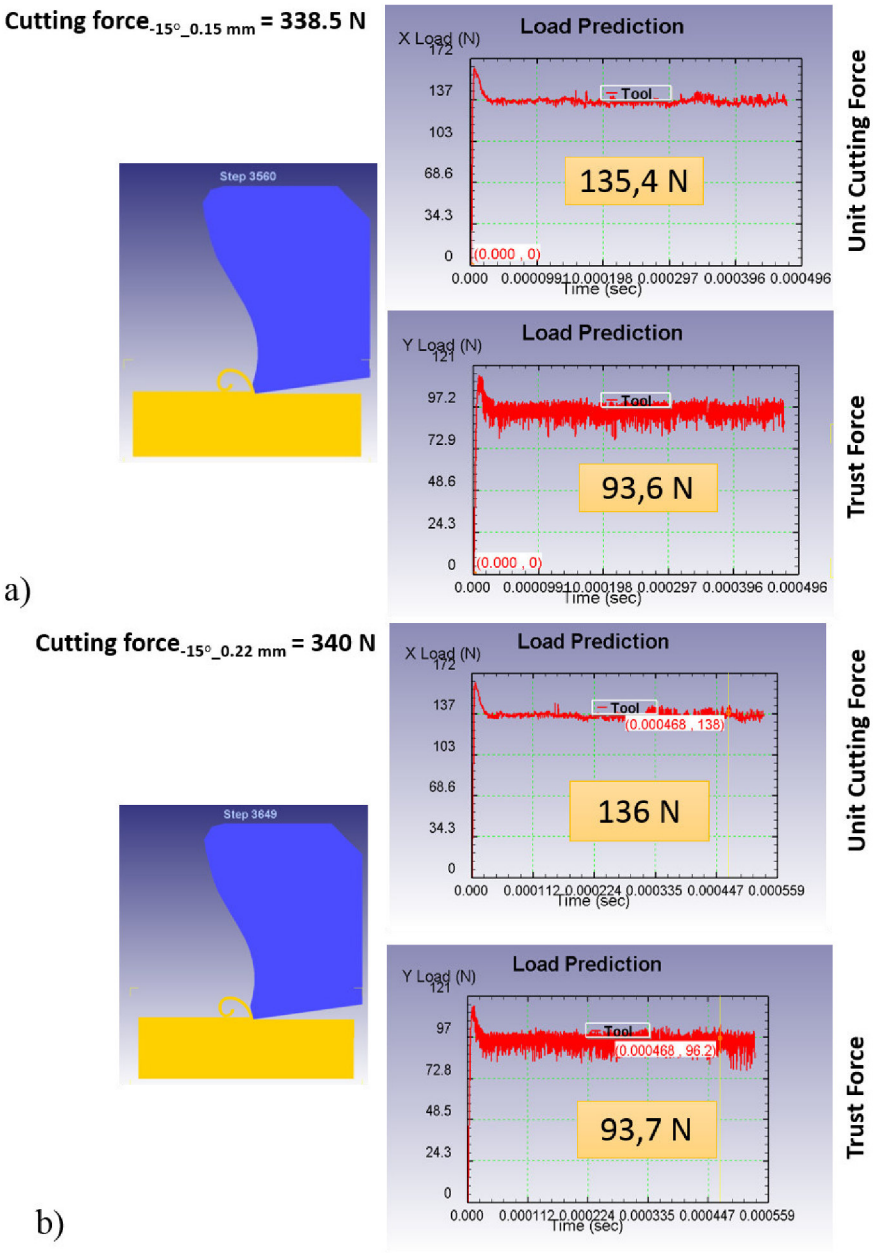


**Figure 82.** Cutting forces for -15° rake angle and a) 0.15 mm rake height and b) 0.22 mm rake height.

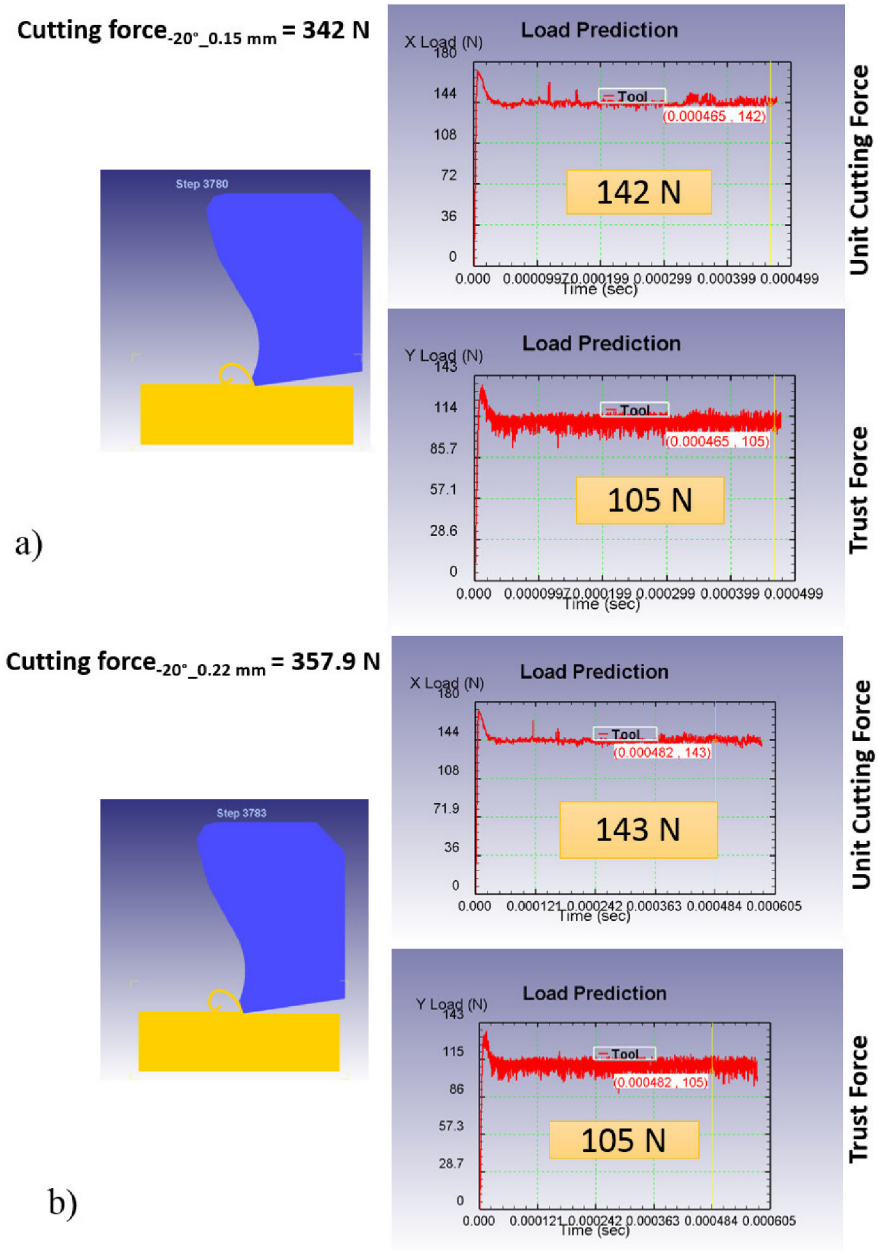


**Figure 83.** Cutting forces for -20° rake angle and a) 0.15 mm rake height and b) 0.22 mm rake height.

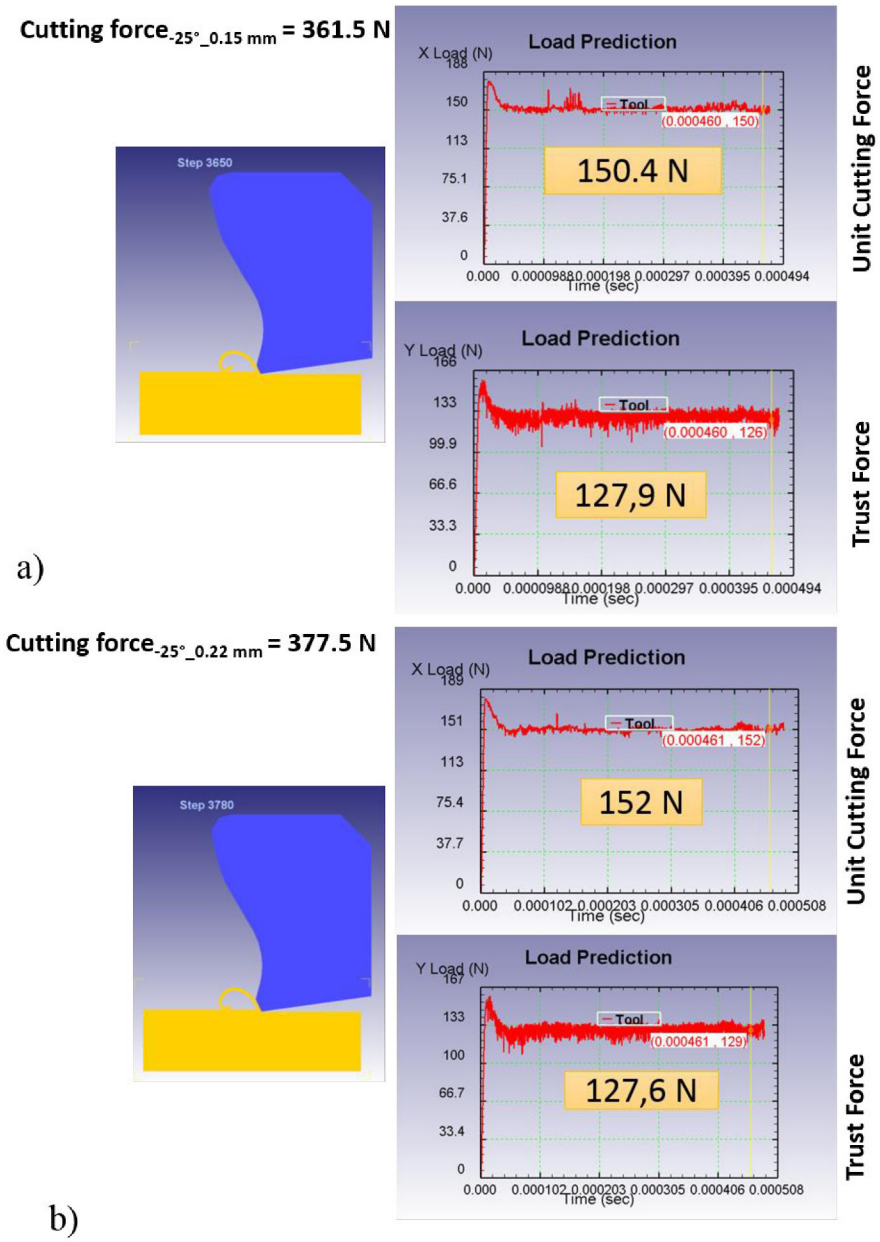


**Figure 84.** Cutting forces for -25° rake angle and a) 0.15 mm rake height and b) 0.22 mm rake height.

From the observation of simulated temperatures in the cutting area some useful information can be drawn to design the new cutting tool (Figure 85). The lowest temperature is associated to the -15° rake angle and 0.15 mm rake height. Due to the chip shape, this is the only one among the 0.15 mm rake height simulated inserts where the chip – rake contact is minimized. On the other side a higher rake face such as the 0.22 mm is more robust for employing different cutting parameters and being more conservative in cases of non optimal set up of the sawing machine. The cutting geometry with -15° rake angle and 0.22 mm rake height was chosen as the optimal geometry due to the minimum differences in temperature (Table 8) and cutting force with respect to the 0.15 mm with the same rake angle.

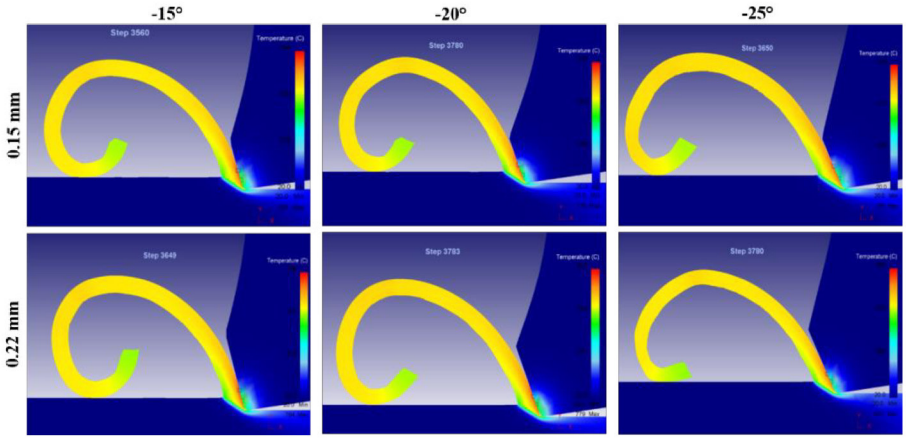


**Figure 85.** Temperature distribution in the cutting area (chip/rake face contact).

**Table 8.** Resumed results from FEM simulation of AISI 4140 orthogonal cutting process.

| Insert geometry (rake angle_rake height) | Cutting Force num [N] | Trust Force [N] | Max Tool Tip Temperature [°C] |
|---|---|---|---|
| **15_0,15** | 338,5 | 93,6 | 761 |
| **15_0,22** | 340 | 93,7 | 764 |
| **20_0,15** | 342,9 | 109,1 | 779 |
| **20_0,22** | 357,6 | 109,1 | 779 |
| **25_0,15** | 361,5 | 127,9 | 796 |
| **25_0,22** | 377 | 127,6 | 802 |

## 5.3 Cutting tests with optimized cutting geometries

The aim of this testing has been dual:

- Experimental validation of the numerical model calibrated with Cof = 0.6
- Tool wear mechanism identification and chip morphology characterization

### 5.3.1 Experimental validation of the numerical model

In order validate the numerical model the cutting forces were derived from conversion of cutting torques for the first 650 cuts. As for the benchmarking test, this last value of cutting force was isolated as the target cutting force after the run in period. Two sets of blades with 0.22 mm rake height were tested: one with -15° rake angle and the other with -25°. The unitary cutting force values were then calculated with the previously exposed procedure and then the average e standard

deviation values were plot against the number of cuts performed (Figure 86).

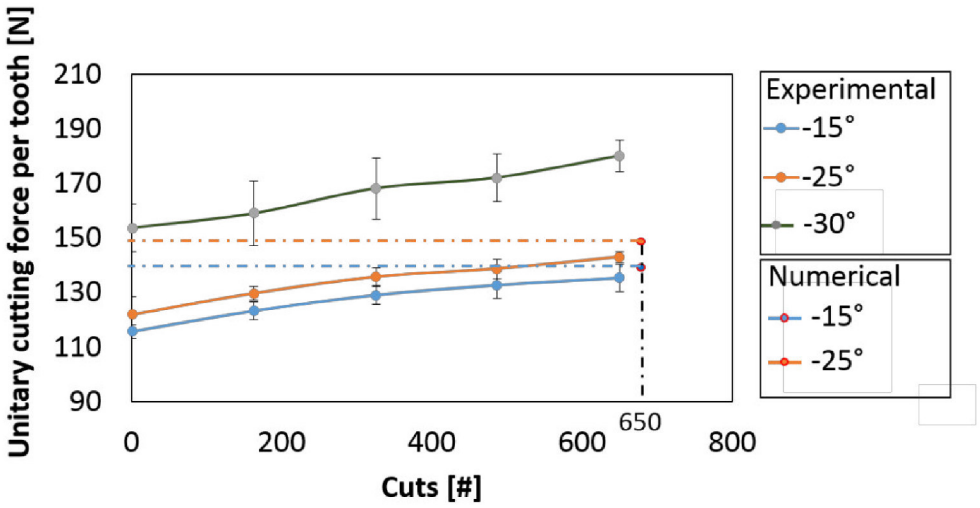


**Figure 86.** Unitary cutting force at 210 m/min as a function of the number of cuts.

From the analysis of cutting force after 650 cuts an experimental cutting force of 135 – 140 N (mean value 138.5 N) was calculated for the -15° rake angle tools versus a numerical estimate of 136 N, the numerical – experimental error is in this case below 2%. An experimental unitary cutting force of 136 – 149 N (mean value 142.2 N) was calculated for the -15° rake angle tools versus a numerical estimate of 150 N, the numerical – experimental error in this case is below 5%.

**Table 9**. Resume of the experimental and numerical data compared for model validation.

| Rake angle [°] | Unitary cutting force_num [N] | Unitary cutting force_exp [N] | Error |
|---|---|---|---|
| -25 | 150 | 136 – 149 | <5% |
| -15 | 136 | 135 – 140 | <2% |

The low numerical – experimental error (below 10%) and the good fit with two different simulated cutting geometries allows to accept the calibrated model as validated; moreover it gains predictive value for simulating other cutting geometries.

## 5.3.2 Quantification of wear on cutting tool surfaces

Two kind of assessments were made on worn tools: a macroscopic assessment of flank wear with a stereomicroscope after the ISO 8688-1:1989 standard to quantify the average $VB_C$ and a microscopic assessment of wear with SEM after proper preparation. For this second characterization two teeth were taken from

different blades after 650 and 3250 cuts respectively for both rake angles; tool surfaces after 3250 cuts were cleaned with Nital 2 (2% $HNO_3$ in ethanol) to eliminate the cutting material that covered the rake face. By adopting this strategy it was possible to put in evidence the cemented carbide substrate and identify the wear mechanisms acting on it. Uniform flank wear for both -15° and -25° rake angle is evidenced in (Figure 87), the -30° geometry is reported in figure for sake of comparison but wear has not been investigated further, this cutting geometry was just employed during the first cutting tests. If compared to the other two geometries it is evident how the tool wears earlier. Due to the fact that these tool are not coated, a built up edge of adhered workpiece is evident since the first 650 cuts, the cutting tool is stable until the built up edge does not remove the cemented carbide material. Flank wear is related to the progressive lowering of the cutting edge, cut after cut. The cutting edge is subjected to continuous sliding against the chip during its formation, thus it is the most solicited feature of the cutting geometry.

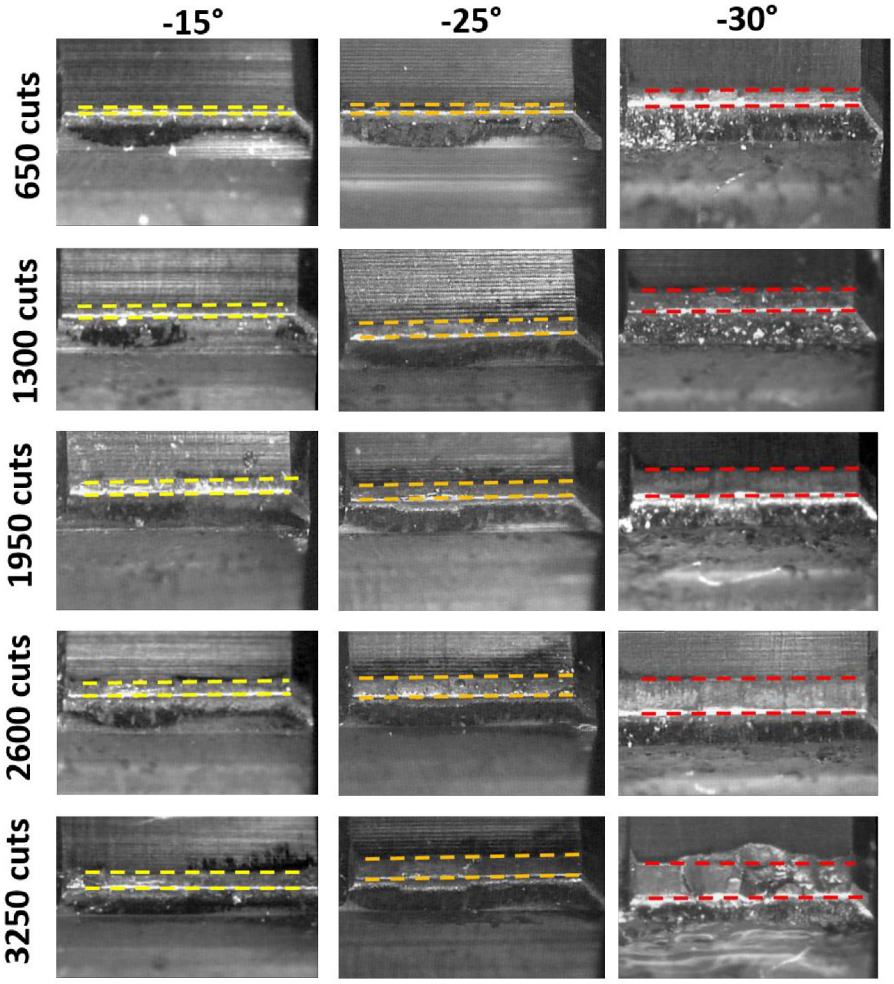


**Figure 87.** Flank wear on cutting tool surface during the whole test.

The usual flank wear value (VBc) to discard a tool and consider it worn out is 0.3 mm. During these cutting tests a more conservative 0.2 mm was adopted also to reduce the testing time. From the plotted data presented in (Figure 88) the -15° rake angle set of tools has not reached the threshold limit for discarding the tool due to flank wear, while both -30° and -25° did well before the end of the cutting test.

The wear curves have a classic shape that can be divided into three sections: a linear run in period up to 650 – 800 cuts, another linear sector characterized by constant wear rate and a final abrupt change of slope that characterizes the final part of tool life that usually end with breakage thus catastrophic failure.

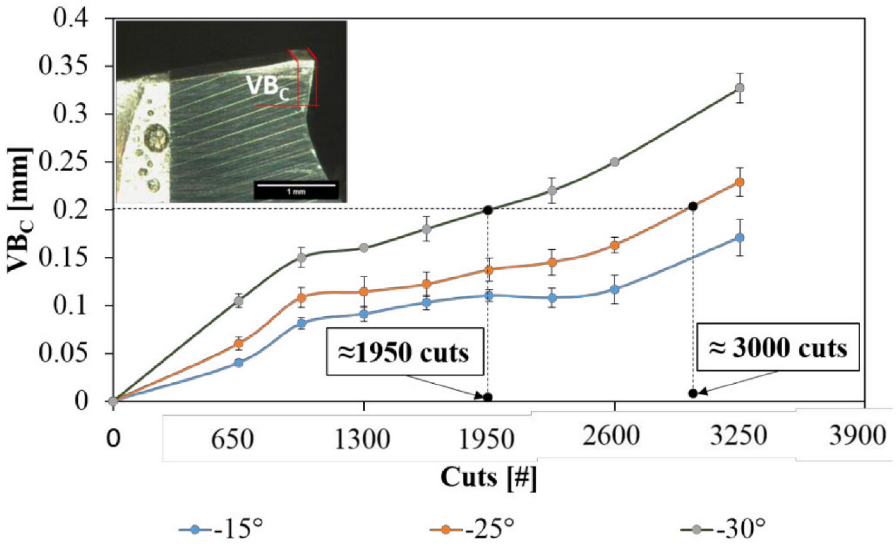


**Figure 88.** Wear curve for cutting tools tested, average wear is plotted against the number of cuts.

Worn volume on the cutting edge was quantified by 3D profilometry, from the analysis of 8 teeth per tool and then averaging the results. In Figure 89a a qualitative representation of the different severity of wear is given. The areas coloured in dark blue represent the most worn parts of the cutting edge. Wear in these plots has to be intended as depth from the surface so these results constitute an integration of conventional cutting wear curves. In Figure 89a the worn volume difference is quantified and plotted; despite a partial overlap in standard deviation uncertainty bars, the two populations differ substantially in terms of average value.

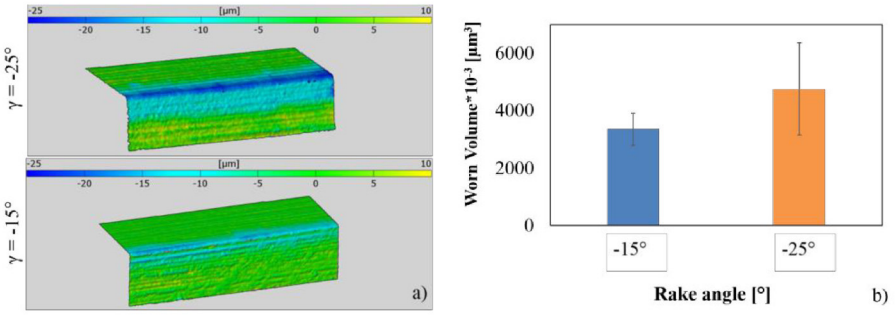


**Figure 89.** Worn volume on the cutting tool surface. a) 3D qualitative comparison between the two geometries, b) worn volume quantification from 3D measurements.

**Table 10.** Wear volume calculated from 3D profilometry, these data are those plotted in Figure 89b.

| | Worn Volume*$10^{-3}$ [$\mu m^3$] | | | |
|---|---|---|---|---|
| | -15° | | -25° | |
| | 4365.9 | 3955.5 | 5483.7 | 8577.9 |
| | 2859.3 | 3121.2 | 5483.7 | 8577.9 |
| | 2492.1 | 2324.7 | 3391.2 | 3917.7 |
| | 3426.3 | 3296.7 | 4031.1 | 4252.5 |
| | 3083.4 | 3339.9 | 4212 | 4014.9 |
| | 2929.5 | 3240 | 3917.7 | 3542.4 |
| | 3790.8 | 3906.9 | 3939.3 | 3728.7 |
| | 4012.2 | 3531.6 | 4433.4 | 4590 |
| | | | | |
| **Mean** | 3355 | | 4756 | |
| **St. Dev.** | 561 | | 1602 | |

## 5.3.3 Tool wear mechanism

Wear on the rake face is already visible after 650 cuts, the built up edge covers the lower part of the area where the chip slides (orange shaded area) while on the top part of the rake face (cutting edge, light blue shaded area) a clear band without adhered material is visible. Another experimental confirmation of the results obtained from the simulations comes from the length of the two red lines present in Figure 90. These lines represent the length of the tool – chip contact and good correspondence is found between experimental data and numerical analysis. The -15° rake angle is characterized by a shorter chip contact along its surface and this reduces the distance that every chip slides during each cut.

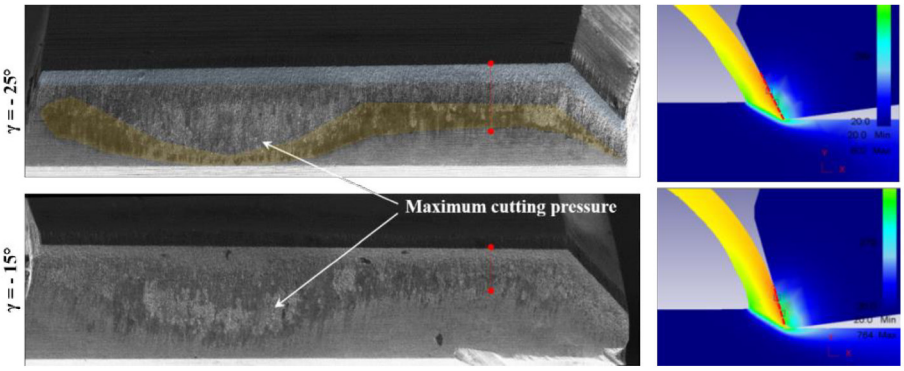


**Figure 90.** SEM images of the rake face of the cutting tools after 650 cuts. The tool was etched with Nital for removal of BUE.

The area denoted as maximum contact pressure is a distinctive feature of saw blades teeth: every tooth has a gullet on top of it named chip breaker deputy to divide the chip in two parts to reduce the total contact pressure acting on the tooth (Figure 91). The chip breaker is alternated sx/dx from one tooth to the subsequent

one so each a tooth cuts, it will have to cut also the portion of material that was not cut by the chipbreaker gullet of the previous tooth, each tooth in that area cuts approximately double the feed per tooth set on the sawing machine. The maximum contact pressure is located in that specific area and will be the most solicited part of the rake face.

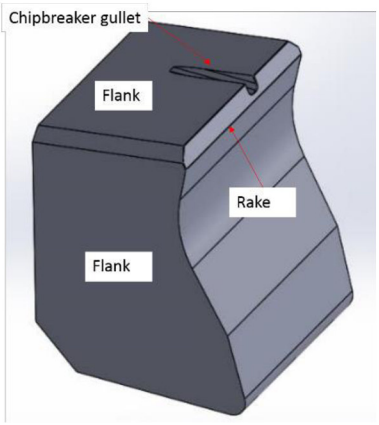


**Figure 91.** Schematic of a cemented carbide tooth for TCT saw blades.

At higher magnification deep grooves are evident on the rake face of the -25° tool indicating that locally severe abrasive wear originate. The groove observed in Figure 92 after 650 cuts for the -25° tool is located on the rake face so it is more likely to be a groove caused by abrasive/adhesive wear and not a fatigue crack.

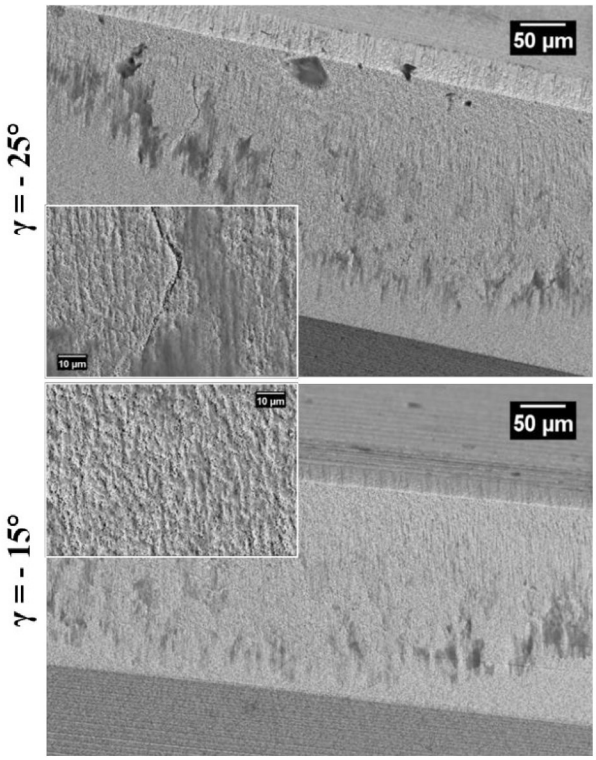


**Figure 92.** SEM-BSE images of the rake face of the cutting tools after 650 cuts.

The surface of the -15° tool on the contrary is rather intact, abrasive grooves are present on its surface too but they have a more uniform appearance and no deep

grooves were detected. The tools surfaces were finally observed at the end of the cutting test after 3250 cuts (Figure 93), flank wear emphasized the difference in wear behavior of the two geometries. Diffused comb cracking on the cutting edge become visible for -25° rake angle tool at low magnifications (white arrows) while abrasive wear grooves are primarily located in the maximum contact pressure area (included between the two red lines) for both rake angle geometries.

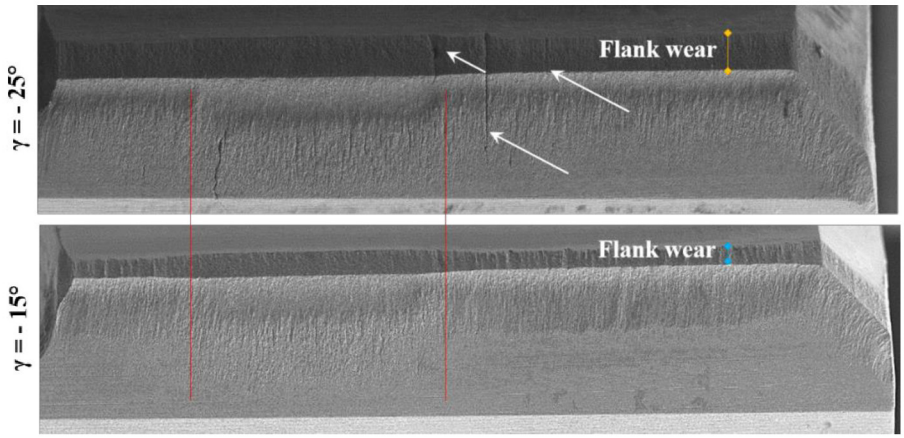


**Figure 93.** SEM images of the rake face of the cutting tools after 3250 cuts.

Wear acting on the rake face was analyzed at higher magnifications (Figure 94) scanning through its whole height. It was evidenced that different wear mechanisms act on its surface despite adhesive/abrasive wear is predominant. The morphology of the tool cutting edge (red shadowed square in Figure 94 b) is characterized by a granular aspect, with carbides in relief, no grooves are evident on this upper part of the rake face. The cutting edge is the part of geometry that forms the chip by cutting, locally it is subjected to high pressure and intimate contact with the chip, this area is the most prone to plastic deformation during cutting. If plastic deformation occurs on the cutting edge, the cobalt matrix is progressively squeezed out and removed one cut after the other leaving the carbides in relief. The sliding speed of the chip on the tool surface increases while descending along the rake face (4) (light blue shadowed square in Figure 94d), furthermore eventual carbides removed from the tool are incorporated in the built up edge that is continuously formed and removed and act as abrasive. This behavior is evident in the lower part of the rake face where deep and narrow abrasive grooves are present. Cracks due to thermo mechanical fatigue mechanisms nucleate on the cutting edge, their progressive growth is influenced by the presence of abrasive grooves on the lower part of the rake face. Abrasive grooves progressively expand towards the upper part of the rake face with the final result that complete cracking of the tooth is observed (-25° in Figure 93). The region in between the plastic deformation dominated area and the abrasive wear dominated area exhibits a transition behavior (yellow shaded square in Figure 94 c), progressively abrasion extends along the rake face.

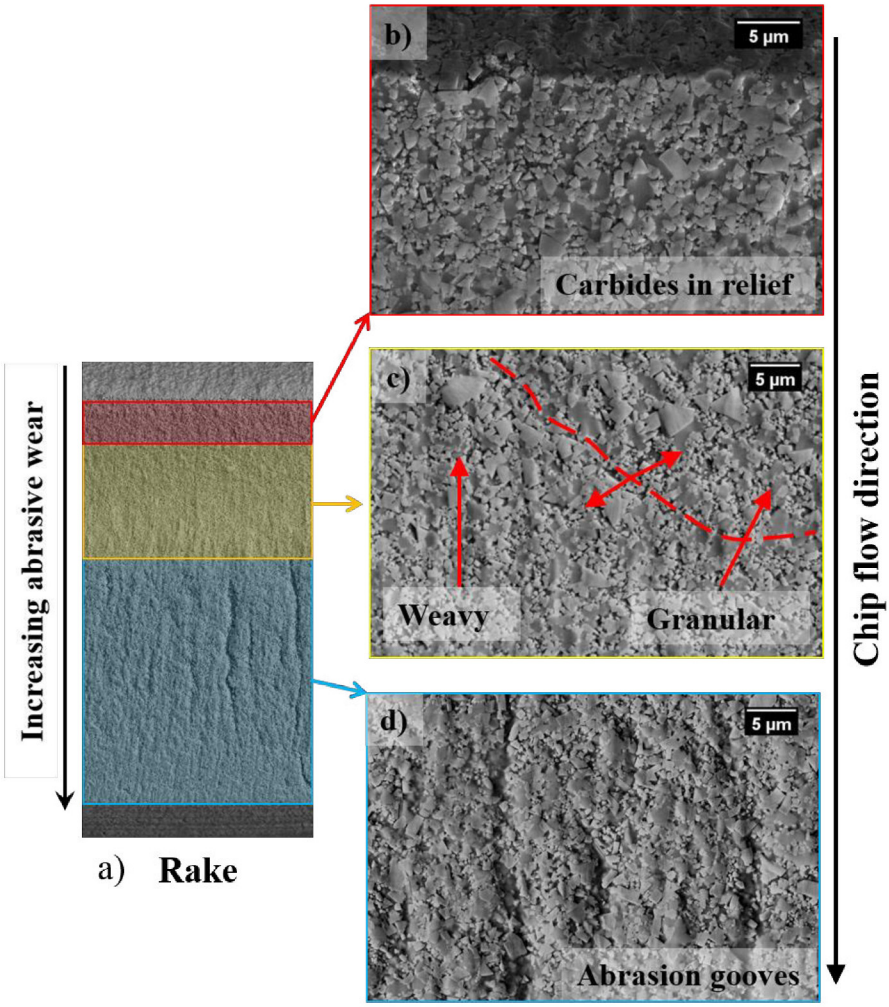


**Figure 94.** Composition of several SEM images at different magnifications, proposed as an interpretation of wear mechanisms on the rake face of TCT saw blades for cutting of metallic alloys. a) merge of SEM images of the rake face, b) cutting edge, c) and d) maximum pressure area.

The wear mechanisms acting on the surface of TCT saw blades are a mix of adhesion/abrasion and are common to all the tested geometries. The main differences observed for tools with different cutting angle is related to the delay of the onset of wear mechanisms acting on the rake surface. Adopting a less negative -15° rake angle for cutting AISI 4140 gave positive results with respect to tool life enhancement. The simulated geometries found experimental validation in terms of both cutting forces and tool/chip contact length, the calibrated numerical model was validated and has predictive value. Cutting tests allowed to verify that -15° rake angle is enough negative to toughen the cutting geometry but not too negative to develop high cutting forces or temperatures. The adoption of too negative rake angles in fact can involve a steep rise in cutting forces and in the tool/chip contact length; both these aspects are responsible for high wear and early failure of cutting tools (Figure 95).

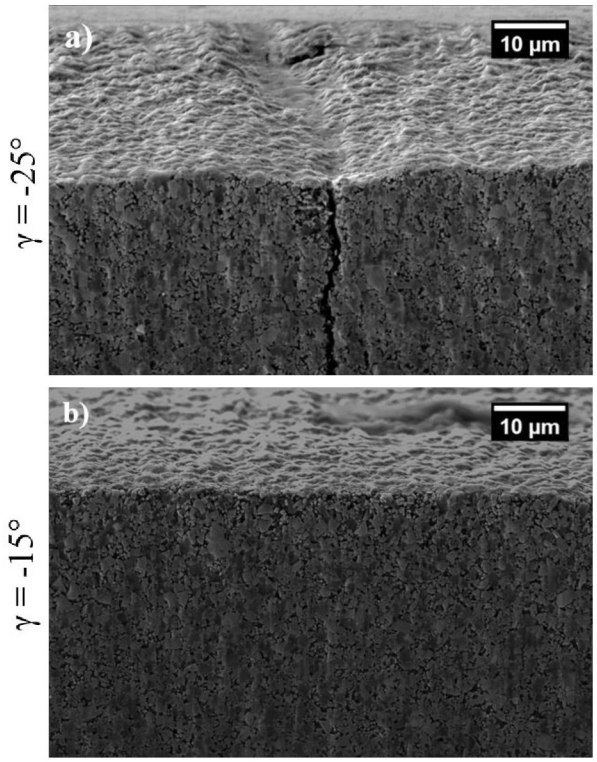


**Figure 95.** SEM images of the cutting edges of two tested tools. a) more negative rake angle, b) less negative rake angle is still undamaged.

## 5.3.4 Chip morphology

During the cutting tests some chips of AISI 4140 were collected for further analysis, mounted in resin, polished and the etched with Nital 2. Etching without burning the microstructure is not easy due to the very high degree of plasticity of each chip (Figure 96).

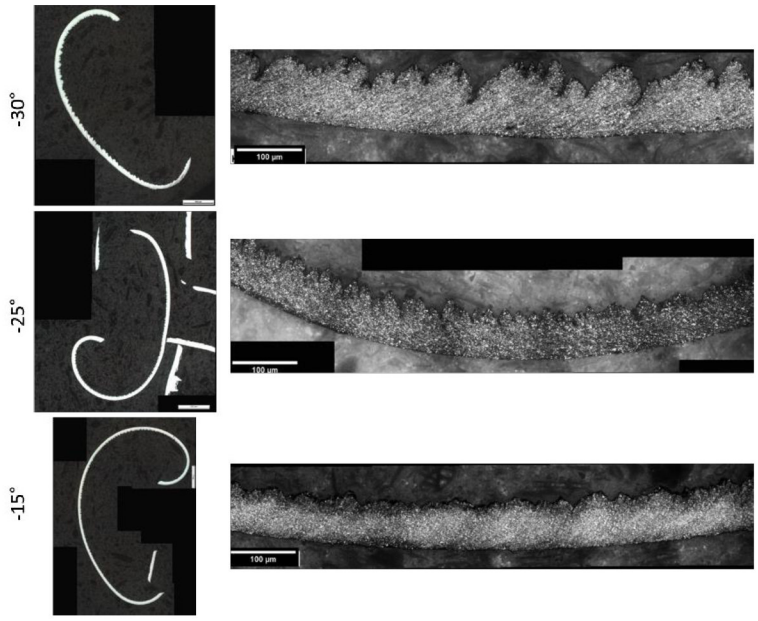


**Figure 96.** Micrographs of the chips, on the left are merged images of the chips while on the right the merged image show the etched chips microstructure.

Despite some common characteristics these chips exhibit different morphologies one from the other due to variations in the cutting mechanism from one geometry (rake angle) to the other. All chips have a segmented morphology typical when cutting ductile materials but the height of the lamellae (deck of cards model) is different among them, in particular an increase in the height of lamellae is observe passing from -15° to -30°. As observed from FEM analysis a more negative rake angle leads to a greater heat generation during the cutting and a larger chip/tool contact that increases the tendency of the chip to stick on the tooth's rake and therefore with the advance of the cut a very jagged shape is created (4). From SEM images of the free internal surface of the chips, the one not in contact with the tool during cutting, it is even more evident the so – called "deck of cards" morphology (Figure 97). The spacing between a lamella and the next one is very regular in chips generated from a -15° rake angle Figure 97 c; the decrease of the rake angle to -25° (Figure 97 b) affects the chip morphology in fact the lamellae change their distribution and become divided in small blocks of lamellae with periodical interruptions. A further decrease of the rake angle to -30° (Figure 97 a) produce a variable distribution in the length of the packages of lamellae: this mechanism can be ascribed to sticking/adhesion of the chip to the rake face that causes a non uniform flow of the chip that is continuously stick and released during its formation.

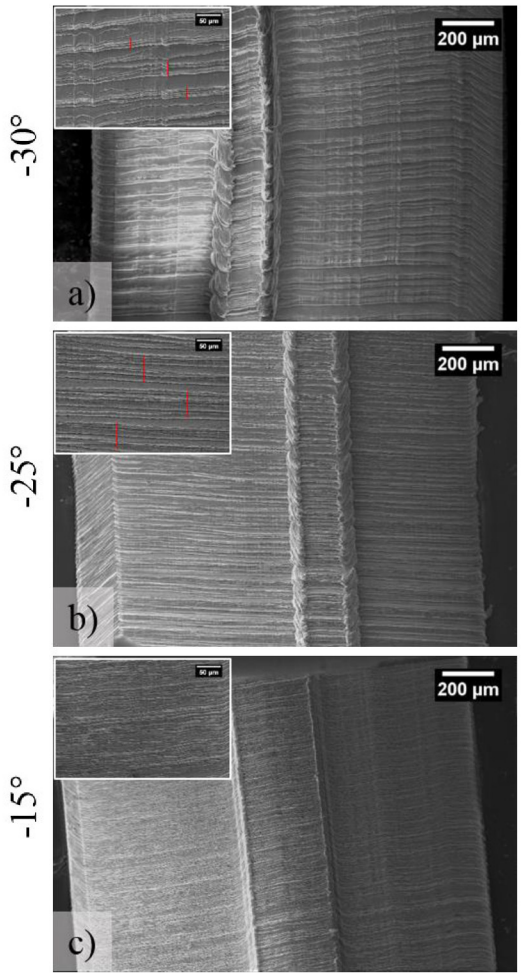


**Figure 97.** SEM images of AISI 4140 chips morphology.

# Chapter 6

# Coating characterization

## 6.1 Surface roughness and droplets quantification

From the roughness measurement of coated samples (Figure 98) a first general information about surface irregularity is appreciable. The substrate was prepared with mechanical polishing, surface roughness ($R_a$) was reduced below 0.1 µm and allow an optimal adhesion of the coating.

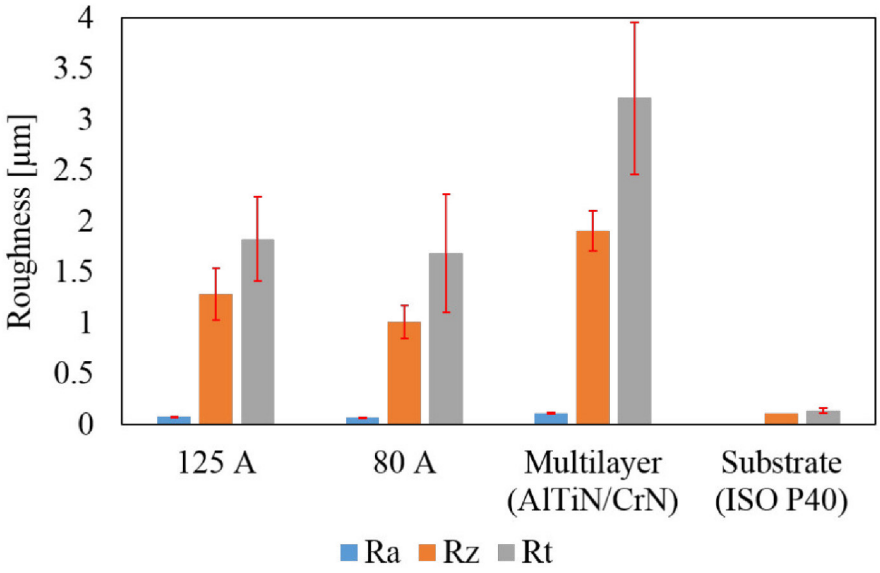


**Figure 98.** Measured roughness parameters for cemented carbide substrate and deposited coatings.

The roughness of the three coatings appear different, in Rz is considered as the most sensitive parameter for an average assessment of surface morphology it is clear that Multilayer coating has higher roughness with respect to the monolayers. No difference is appreciable instead between the two monolayer coatings. A higher surface roughness indicates that surface irregularities have different heights among the samples but from this analysis no further infers can be drawn, for example these data are not enough to give any information about the density of defects on the coated surface.

**Table 11.** Roughness values plotted in the histogram above.

| Roughness parameter | Substrate (ISO - P40) | | AlTiN 125 A | | AlTiN 80 A | | Multilayer AlTiN/CrN | |
|---|---|---|---|---|---|---|---|---|
| | *Av [µm]* | *σ [µm]* | *Av [µm]* | *σ [µm]* | *Av [µm]* | *σ [µm]* | *Av [µm]* | *σ [µm]* |
| **Ra** | 0,0133 | 0,0057 | 0,076 | 0,0054 | 0,068 | 0,0044 | 0,112 | 0,0083 |
| **Rz** | 0,1133 | 0,0115 | 1,284 | 0,2570 | 1,012 | 0,1646 | 1,908 | 0,1942 |
| **Rt** | 0,14 | 0,0264 | 1,826 | 0,4165 | 1,686 | 0,5795 | 3,214 | 0,7468 |

From a qualitative observation the surface of the coatings (Figure 99) a more marked difference in the level of defectiveness (density of droplets on the surface) is appreciable: the low current monolayer in particular seems to have a lower density of defects if compared to the 125 A monolayer and the Multilayer (both deposited with 125 A cathode current).

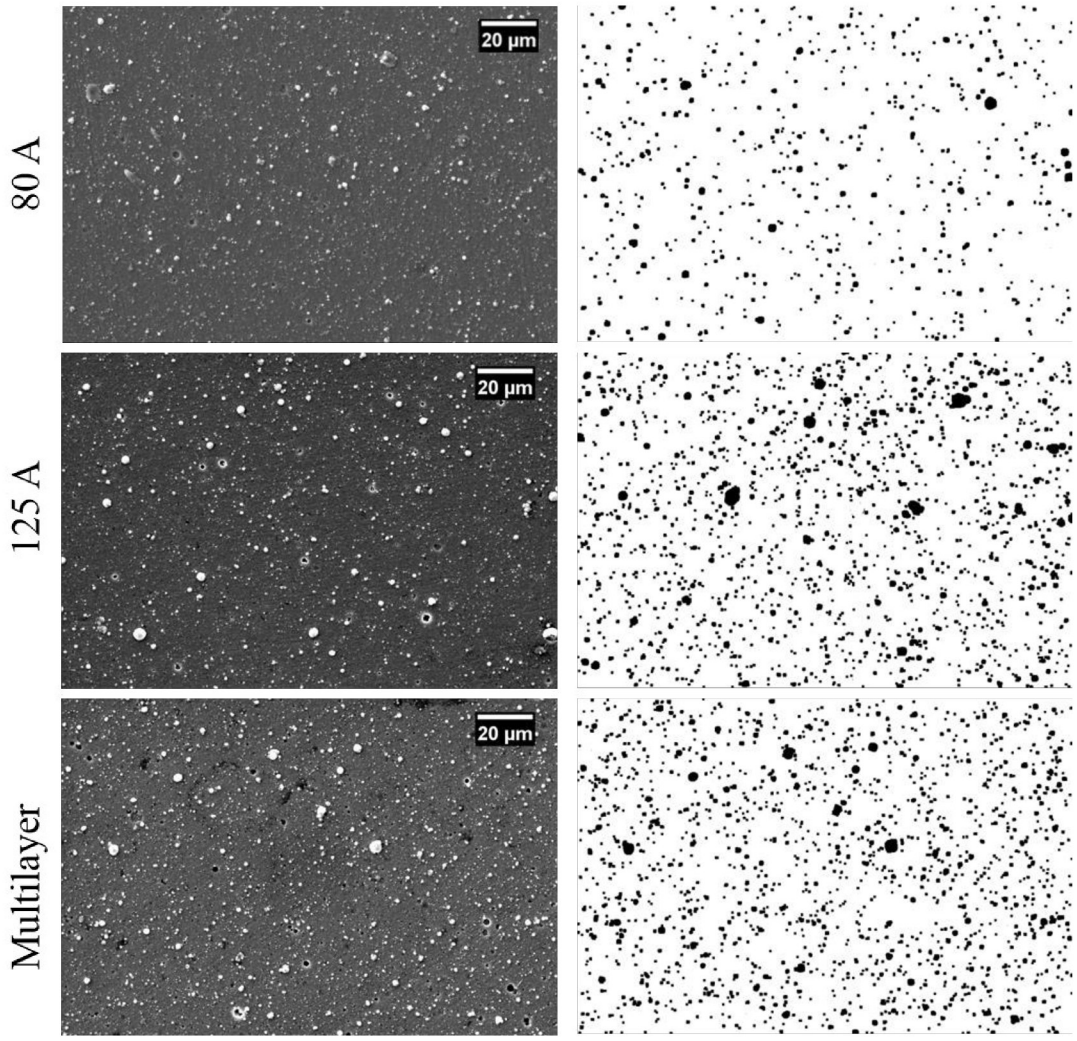


**Figure 99.** SEM images of coated surface. The binarization of the image is presented aside.

The quantitative evaluation of defects density on the coated surfaces gives more information about the surface state of samples. The average dimension of the defects is the same for the three coatings (approx. 1.7 µm from Table 12) but the substantial difference lies in the number of defects (Figure 100). The 80 A monolayer coating has less defects as confirmed by the defect density bars. The other two coatings were deposited with the same cathode current, this parameter influences the amount of droplets emitted, typically a higher current reduces coating process time at the expenses of surface quality.

**Table 12.** Quantification of surface defects density and average defect area from image analysis.

| Coating | Defects density [µm$^{-2}$] | Average area [µm$^2$] |
|---|---|---|
| **125 A** | 0.04 | 1.7 ± 0.4 |
| **80 A** | 0.02 | 1.7 ± 0.3 |
| **Multilayer AlTiN/CrN** | 0.05 | 1.7 ± 0.6 |

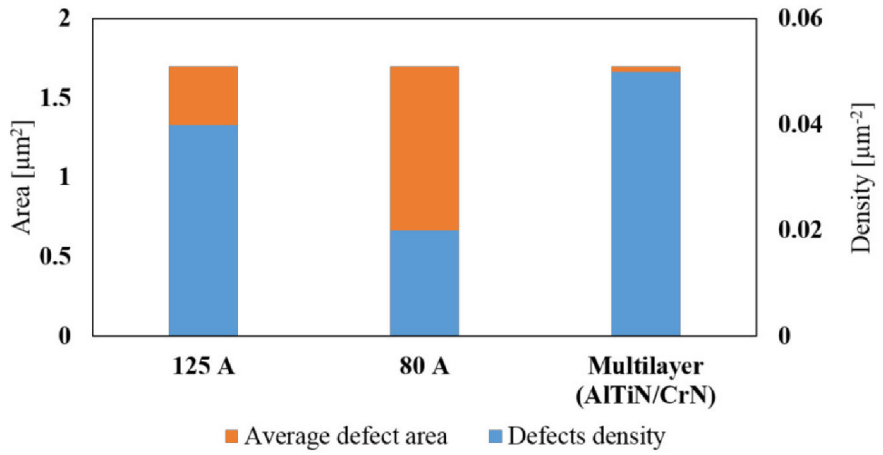


**Figure 100.** Surface density of defects and average area of droplets for each coating.

The dimensional distribution of the measured defect represented in Figure 101 is in accordance with the defects measured average dimensions, in fact the three distributions all have the same tendency. The bars indicating the dimensional classes of defects do not have the same height due to the fact that a different number of defects was observed for each coating. In particular the 80 A monolayer is confirmed to be the less defective among the three. During the deposition of the multilayer coating all four cathodes (Cr, AlTi 50/50 and AlTi 63/37) were contemporary turned on during the deposition of the inner layers while the top layer was pure AlTiN with just three cathodes on. The defects counted are those present on the surface so it is reasonable that both 125 A monolayer and the corresponding current multilayer have a comparable level of surface defectiveness.

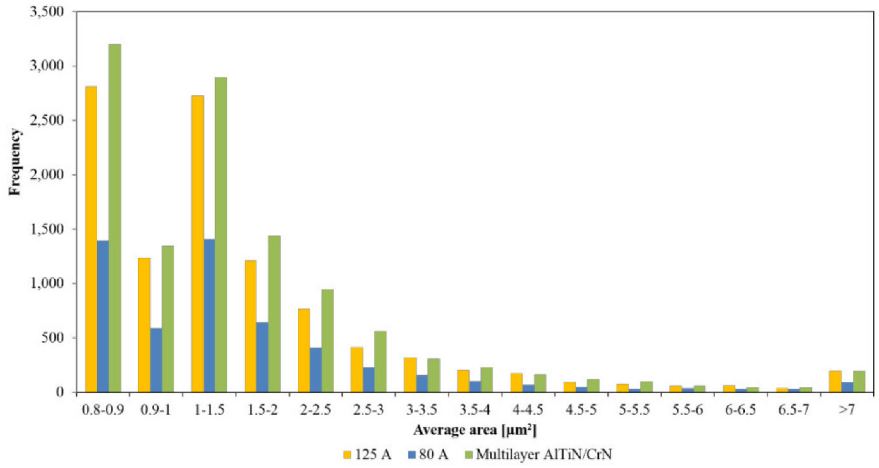


**Figure 101.** Dimensional distribution of droplets on the surface of coated samples.

From the analysis of defective area and average size of the two monolayer at different size intervals (d> 0.35 µm, d> 0.5 µm, d> 1 µm) comes the definitive confirmation that operating at lower cathode currents reduces the number of defects, not the average dimension. This effect can be due to the intrinsic chemical nature of cathodes that tend to emit particles with fixed dimension depending on their composition. Typically, low melting point elements (such as Aluminum) have higher tendency to emit particles during phase vapour deposition while high melting point elements such as Chromium have a lower tendence, this is the reason why CrN coatings are smoother (71).

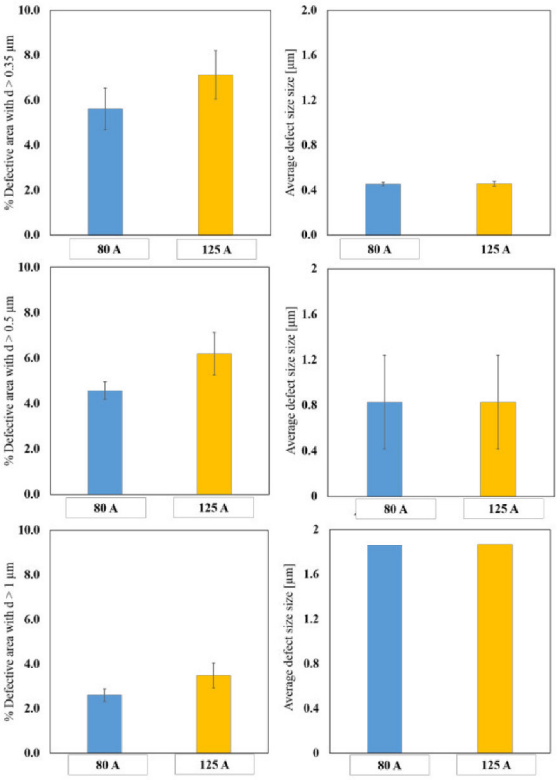


**Figure 102.** Analysis of defect dimension and defective area considering different dimensional intervals.

## 6.2 Composition and morphology

The surface and the cross sections of platelets samples were analyzed by SEM and FESEM; surface and cross section morphologies were observed, semi quantitative EDS analysis were made on both the surface and the cross – section.

### 6.2.1 Surface morphology and composition

From previous trials and indications given by the coating plant producer it was assessed that the composition of the surface layer of the coating deposited at 125 A using that current parameters and that specifica cathode configuration is $Al_{0.55}Ti_{0.45}N$. From EDS analysis it is not possible to determine the precise stoichiometric composition of coatings but some interesting conclusions can be drawn (Figure 103).

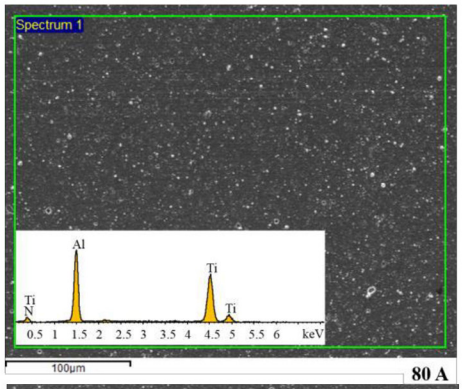


| Element | Weight% | Atomic% |
|---|---|---|
| N | 15.84 ± 2.09 | 32.61 |
| Al | 35.76 ± 0.96 | 38.24 |
| Ti | 48.4 ± 1.26 | 29.15 |
| Totals | 100 | |

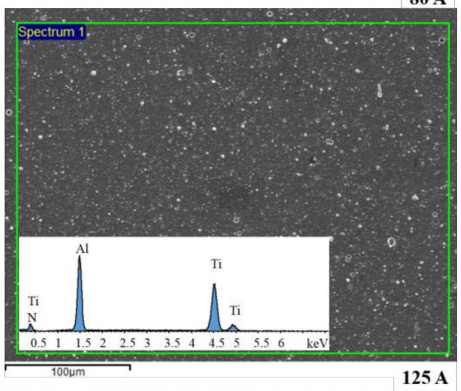


| Element | Weight% | Atomic% |
|---|---|---|
| N | 11.31 ± 2.51 | 24.81 |
| Al | 36.75 ± 1.13 | 41.86 |
| Ti | 51.95 ± 1.54 | 33.33 |
| Totals | 100 | |

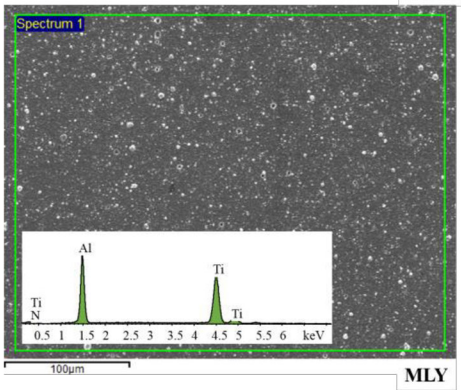


| Element | Weight% | Atomic% |
|---|---|---|
| N | 10.4 ± 1.89 | 23.14 |
| Al | 36.75 ± 0.84 | 42.46 |
| Ti | 52.85 ± 1.16 | 34.4 |
| Totals | 100 | 100 |

**Figure 103.** EDS semi-quantitative analysis of the surface composition of coatings.

The surface of 125 A monolayer coating and that of the Multilayer have in fact the same composition; the 80A coating instead appears to be deployed in the content of Titanium. Lower cathode current decreases the deposition rate of the coating and thus reduces the number of metallic atoms that would form the coating on the substrate but also the number of evaporated metallic particles that would deposit as droplet decreases. The matter extracted from the cathode in the unit of time is decreased so the process reactive gas present in the deposition chamber (Nitrogen) increases his poisoning power towards the cathode that is covered on the surface by a layer of reacted species that will not be deposited as droplets. The enrichment in Nitrogen is then found in the coating itself.

### 6.2.2 Cross section assessment

The observation of the cross section was done on fragile fractured surfaces, samples were immersed in liquid nitrogen and then fractured in air, FESEM observation was done immediately after in order to preserve the fracture surface. By this method it is possible to observe the microstructure of the coating through its thickness, this is not possible by conventional metallographic preparation: artifacts and the complete polishing of the surface completely destroy the morphological contrast given by the microstructure. From the observation of fractured surface (Figure 104) all three coatings appear intact and characterized by a good adhesion. At a lower magnification the fracture surfaces of the high current coatings (125 A and Multilayer) appear smoother, more dense and characterized by fine microstructure. The 80 A AlTiN in the other side has a rougher fracture surface.

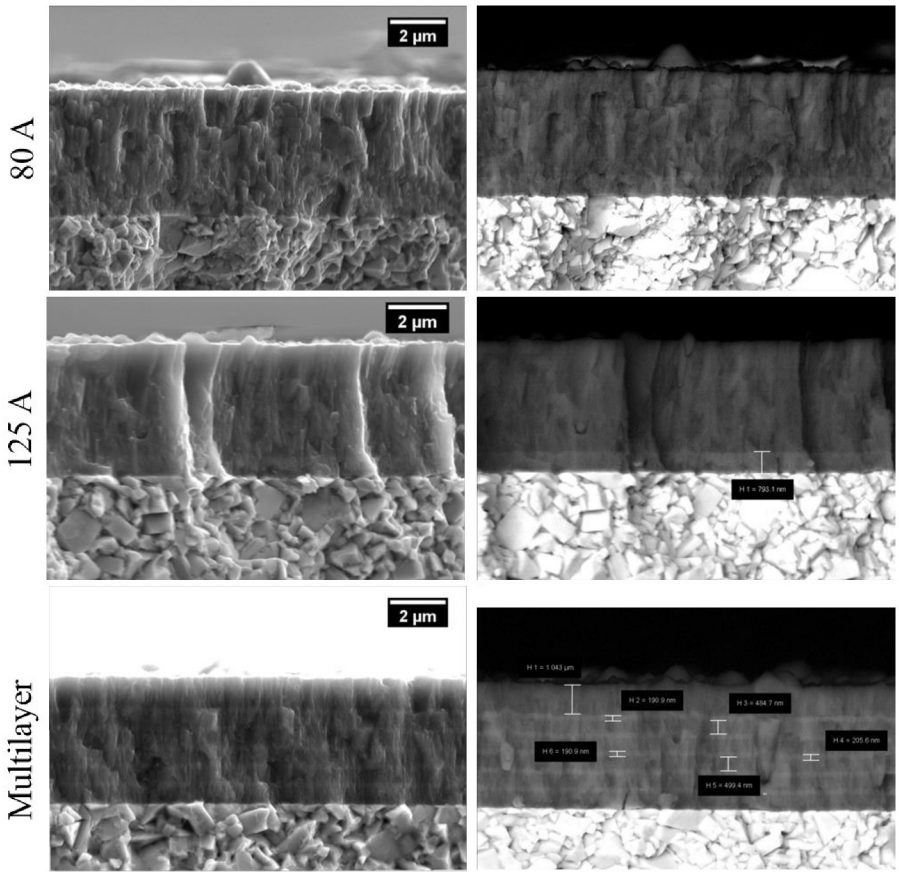


**Figure 104.** FESEM images of cross sections fractured in liquid nitrogen.On the left morphologic images (SE), on the right compositional images (BSE).

The explanation to this observation has to be searched in the current parameter adopted: higher current means a higher deposition rate and thus a higher density. The adhesion layer enriched in CrN is evident at a higher magnification (Figure 105), after the deposition of such layer a gradient is done by contemporary switching on all the cathodes, the deposition of a gradient layer between adhesion and work layer is beneficial in order to reduce residual stress/strains at the adhesion/working layer interface that might induce premature delamination of the coating. This feature is common to the 80 A and the 125 A coating while the multilayer is characterized by continuous gradients.

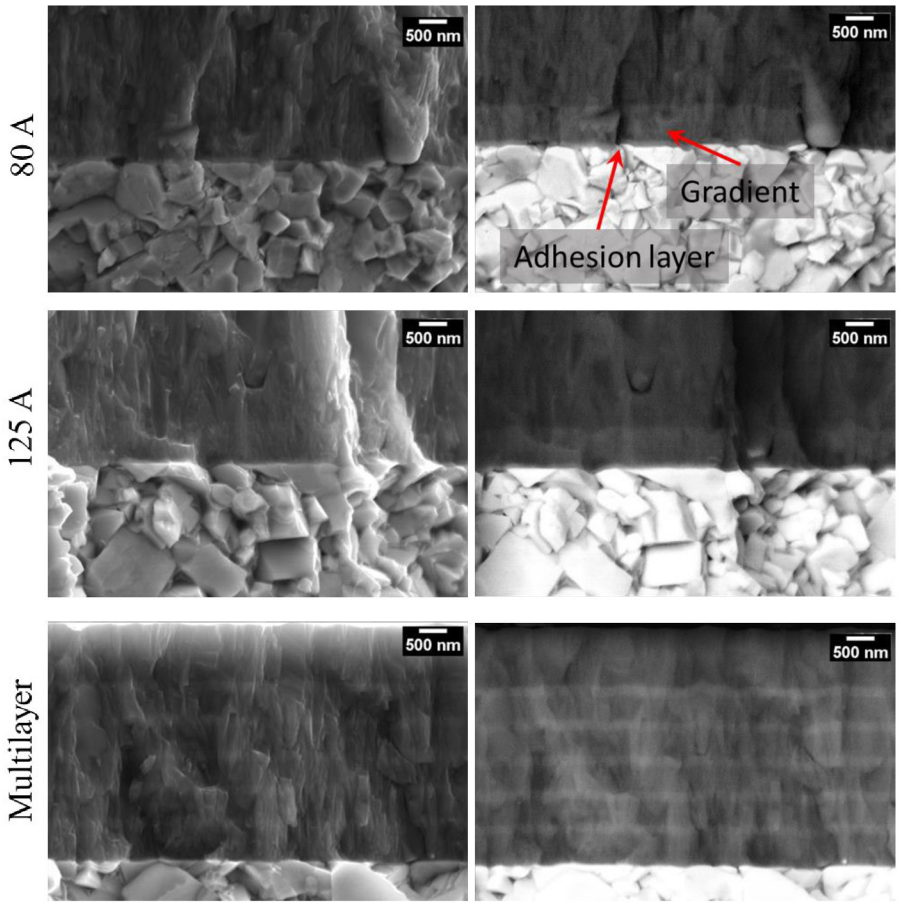


**Figure 105.** FESEM images of cross sections fractured in liquid nitrogen, higher magnification On the left morphologic images (SE), on the right compositional images (BSE).

In Table 13 the summarization of thickness measurements is presented.

**Table 13.** Summarization of the measured coating thickness.

| Coating | Thickness [µm] | Adhesion [µm] | Gradient [µm] | Cr enriched – Interlayer [µm] | Al enriched – interlayer [µm] |
|---|---|---|---|---|---|
| **80 A** | ≈ 4.2 | 200 nm | 0.8 | - | - |
| **125 A** | ≈ 4.1 | 200 nm | 0.8 | - | - |
| **Multilayer AlTN/CrN** | ≈ 4.5 | 200 nm | 0.5 | 0.5 | 0.2 |

After metallographic preparation of cross sections obtained through cutting, an EDS line scan was performed on the section of one of the monolayer coating (125 A) and on the multilayer to give a qualitative evidence of the elemental chemical variation in composition through the thickness of the two architectures (Figure 106). The monolayer coating has a constant ratio between Al and Ti through the whole thickness, furthermore it is evident the peak related to the chromium adhesion layer and its subsequent decrease do to the enrichment in Al and Ti. On the opposite the multilayer coating is characterized by a continuous gradient in Chromium that reaches the maximum in correspondence of the light grey interlayer

and then decreases through the thickness of the AlTiN rich layer. The surface layer, as observed previously is just pure AlTiN.

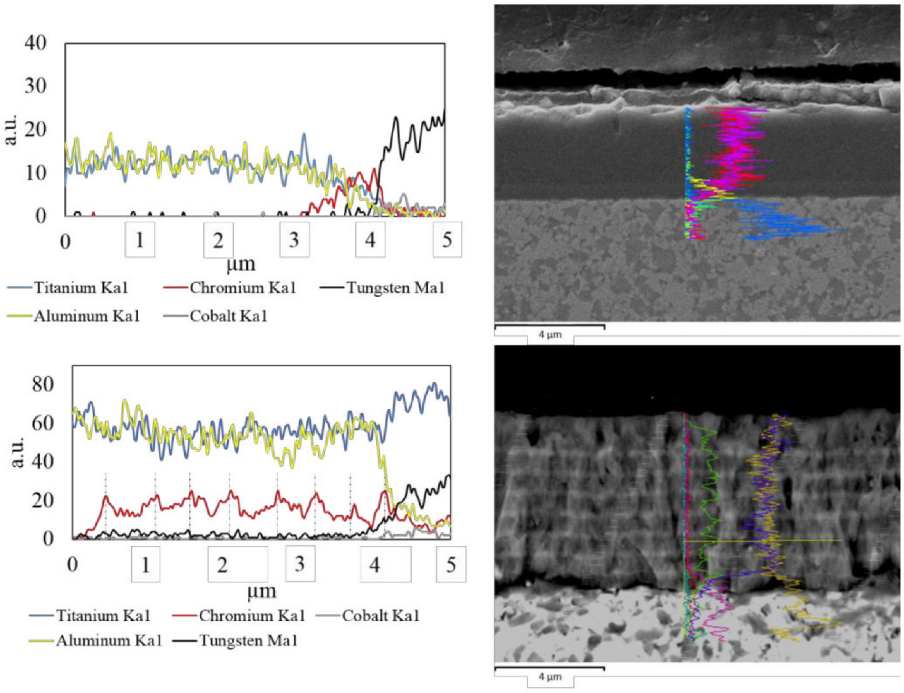


**Figure 106.** EDS linescan through the coatings thickness. On top a 125A monolayer coating, on bottom the multilayer.

# 6.3 Mechanical properties

## 6.3.1 HRC Adhesion

After indenting with Rockwell penetrator the observation of the coating surface lead to classify all coatings as HF1 in the Mercedes – Rockwell. The 80 A monolayer might be borderline between HF1 and HF2 due to those long cracks observable in Figure 107. Despite this the adhesion level tested by HRC was satisfactory for all three coatings.

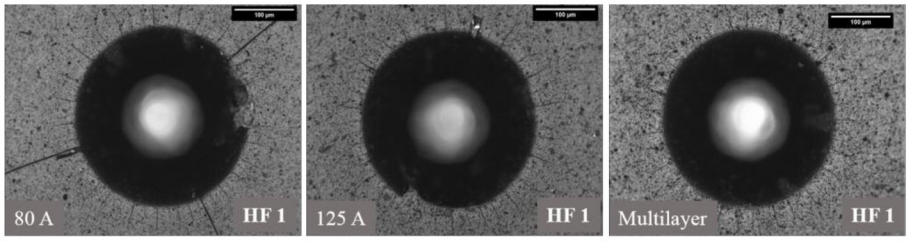


**Figure 107.** Mercedes Rockwell (HRC) adhesion results.

### 6.3.2 Nanohardness – nanomodulus

Nanoindentation tests gave interesting results with regard to mechanical properties that are reported in Figure 108. The multilayer architecture is characterized by a higher hardness if compared to the other two monolayers. No current effect can be inferred, in fact both monolayer coatings despite having been deposited at different cathode currents have similar values of hardness and elastic modulus. The increase in mechanical properties of the multilayer is caused by two different interacting mechanisms. On one hand the coating multilayer architecture favors the formation of a dense coating with fine microstructure, the continuous variation in composition through the coating thickness in fact causes recrystallization to occur producing thus a finer microstructure. On the other hand the introduction of Cr in the through thickness of the coating causes a variation in the chemical composition of the coating that passes from AlTiN for the monolayer to $Al_xTi_yCr_zN$, the addition of Cr to AlTiN enhances Al solubility in the TiN crystal lattice as a result lattice strains raises and hardness consequently.

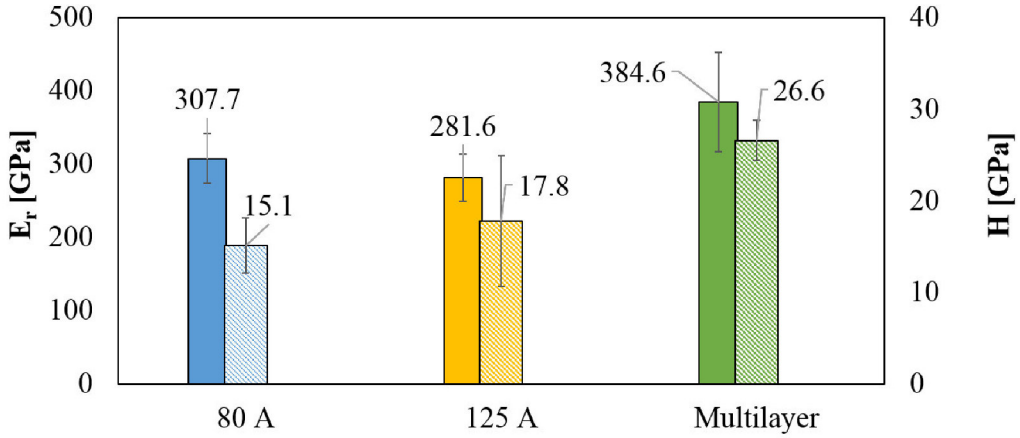


**Figure 108.** Nanohardness on the right and nanomodulus on the left for each sample as measured by nanoindentation tests.

### 6.3.3 Scratch resistance

Nanoscratch results confirmed the good adhesion of all three coatings, the coefficient of friction of the diamond stylus scratching the coatings surface was registered (Figure 109). From this data it is evident a difference in the coefficient of friction between test made at 1000 mN and 5000 mN, this is due to the testing procedure itself. By applying a higher load the penetrator will indent at a higher depth and if the scratch speed is kept constant this will mean that the penetrator will encounter far more material on its trajectory. Apart from this consideration all 1000 mN scratches are characterized by a higher fluctuation which is supposed to be due to a higher interaction with surface asperities, on the contrary for the 5000 mN scratches these fluctuations are limited and present only at the beginning of the scratch. From these plots it is assumed that no delamination occurred in fact the

coefficient of friction increases constantly without any abrupt change that would be the sign of a change of the scratched material.

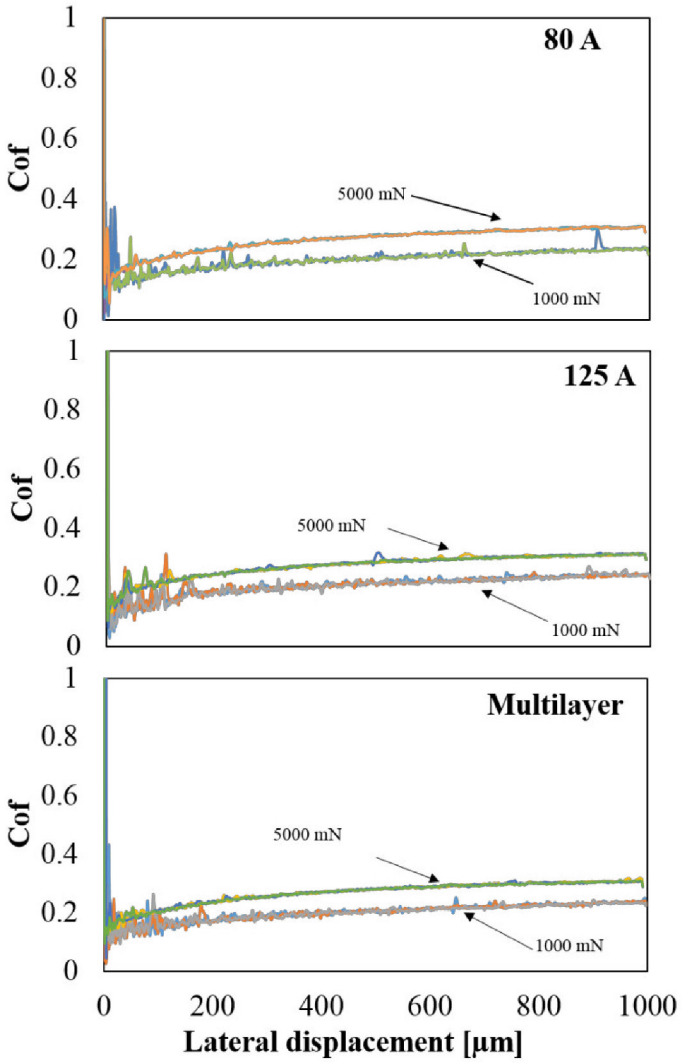


**Figure 109.** Friction coefficient variation during nanoscratch tests at 1000 mN and 5000 mN.

The optical images of the scratches confirmed the hypothesis made on the basis of the coefficient of friction (Figure 110). The scratches made at 1000 mN maximum load are very thin, no delamination occurred on these scratches. The scratches made at 5000 mN on the contrary are larger and even though no delamination is evident from optical microscope images a certain level of debris was produced. The substrate is cemented carbide so if any delamination occurred it would have appeared as a bright spot along the scratch. The debris content is higher for the coatings deposited at 125 A. Because of this result it is not possible to determine the $LC_2$ value.

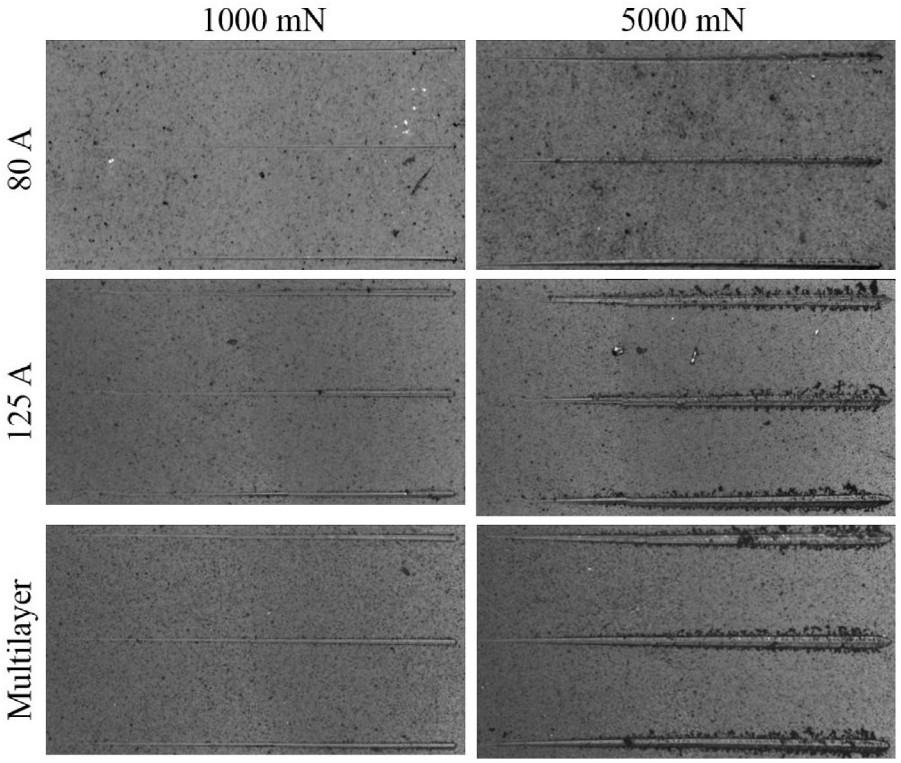


**Figure 110.** Micrograph of the nanoscratches at different loads.

Some observations made from the optical micrograph were analyzed more in depth by observing the scratches at a higher magnification with SEM (Figure 111). What is common to all three coatings is that in neither case the delamination occurred showing the uncovered substrate, anyway different scratch morphologies were observed.

- At 1000 mN the three scratches are similar, they do not present cracks at the edges but for 125 A sample and for the multilayer a relevant presence of wear debris is observed
- At 2500 mN all three scratches show the presence of cracks due to plastic deformation and subsequent local failure of the topmost layers of the coatings. The debris content for 125 A and multilayer has increased, debris accumulated at the edges of the scratch.
- At 4000 mN some sign of delamination are manifested but no substrate is visible, this is due to the fact that delamination occurred on the surface and did not reach the substrate. Differently from the previous loads discussed, in this case the scratches from the two monolayers have a similar morphology with a large piece of coating detached. The Multilayer on the contrary exhibits a fragmentation of the damaged layer that can be ascribed to the fragmentation of just one superficial layer. Debris present in 125 A and multilayer coating are supposed to be related with defects, these two coatings in fact have an higher fraction of surface droplets compared to the 80 A.

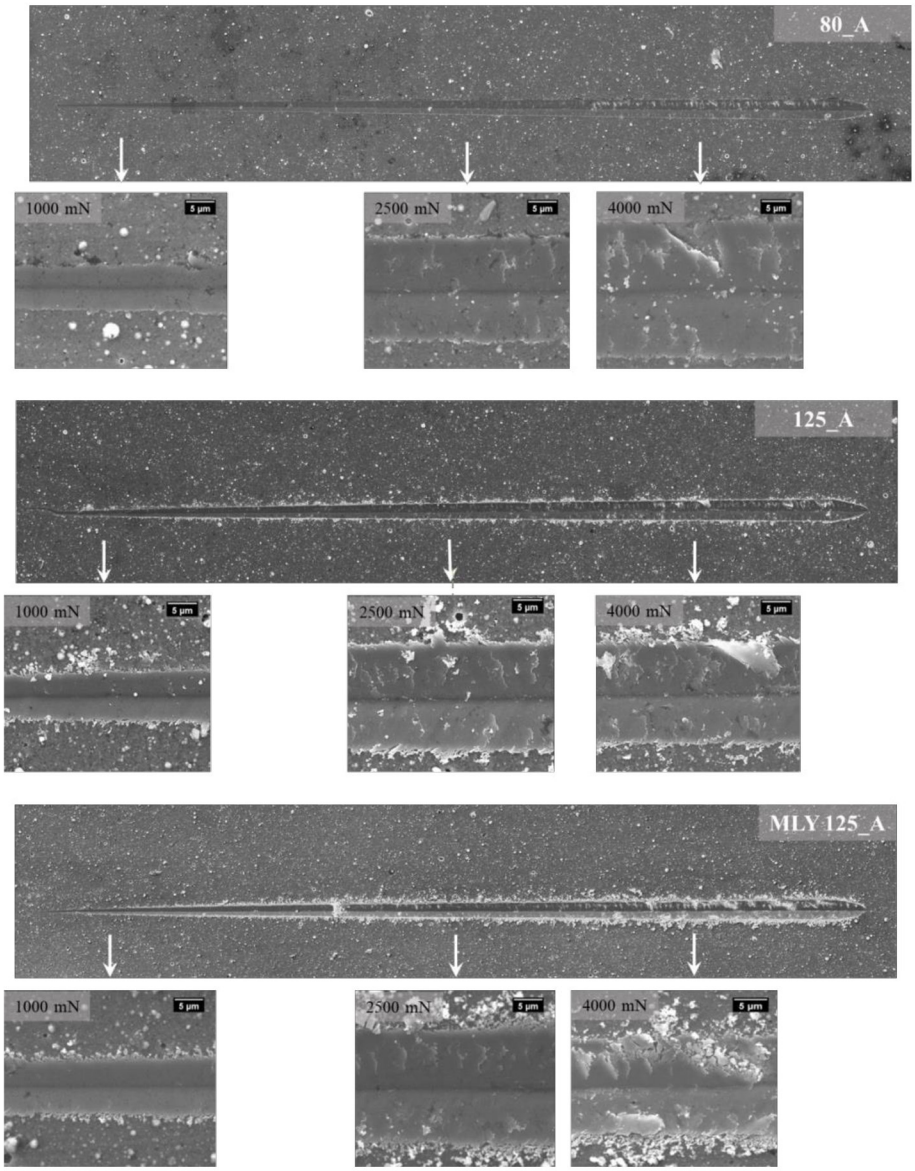


**Figure 111.** SEM images of the nanoscratches at 5000 mN with local magnifications at 1000, 2500 and 4000 mN.

# Chapter 7

# Conclusions

The goal of this doctoral thesis was the development of an innovative multipoint machining tool for cutting – off operations, performed at high cutting speed. Conventional TCT saw blades for steel cutting, work at low speed, the objective of this work was to double up the production rate of these tools; in order to reach this goal the cutting tool was re conceived starting from the choice of the most suitable grade of cemented carbide to the optimization of the cutting geometry. Cathodic arc PVD coatings of the Al – Ti – Cr – N system were characterized and a tailored coating for this application was conceived. Based on the obtained results the following conclusions are presented for each of the subject studied.

- Three mixed grades of cemented carbides with micrometric grain size and a plain grade with sub micrometric grain size were studied and their morphological and mechanical properties were characterized. From the evaluation of hardness and toughness using the Palmqvist method it was confirmed that toughness in cemented carbides is influenced both by the volume fraction of binder and by the carbide grain size. If the volume fraction of binder is the same, a larger grain size confers higher toughness to the cemented carbide due to a higher binder free mean path. Tribological testing of cemented carbide discs with a pin on disc configuration was done to simulate wear acting on a tool flank where a conformal continuous contact is present during cutting. From the results obtained against pins made of both ferritic AISI 4140 and austenitic AISI 660 steel, wear was characterized on the surface of the discs. Adhesive/abrasive wear mechanisms acted on the surfaces of all cemented carbides but also mechanisms spalling and surface fatigue-like damaging was observed for low toughness grades. Based on these observations the grade characterized by the highest toughness was chosen for the subsequent cutting tests.
- Cutting tests with AISI 4140 were performed for cutting forces benchmarking and building a numerical model using Oxley modelization of the flow stress. Two rake angle geometries were tested to validate the model: -15° and -25°. From experimental results the model set with 0.6 coefficient of friction was validated with a total experimental – numerical error below 5%. Tool wear was characterized and according to standards: -15° rake angle ensures the longest tool life due to reduced cuttings forces (simulated numerically and confirmed experimentally) and reduced chip – tool contact length (simulated numerically and confirmed experimentally), after completion of the cutting test (3250 cuts) the average wear of the tools with -15° rake was below the acceptance limit set for the test while -25°

passed it after 3000 cuts. Wear mechanisms acting on the tool surface were characterized by observation of the rake face of small cemented carbides inserts removed from the cutting tool after testing. After removing the steel sticked to the cutting geometries (built up edge), the wear scars were revealed. Abrasive/adhesive wear is the main cause of wear and eventually leads to failure of the cutting tool. Nevertheless the cutting edge is more prone to a mixed wear mechanism with a component of plastic deformation that favours the depletion of binder.

- Three coatings were deposited with a Platit CAE – PVD coating unit designed for coating saw blades. Two monolayer AlTiN coatings with CrN adhesion layer and a multilayer were deposited on cemented carbide samples and then characterized in morphology and mechanical properties. The two monolayered coatings were deposited varying the cathode current from 125A for the first sample to 80 A for the second one. The objective was to obtain a less defective surface. From the quantitative characterization of surface defects we can conclude that decreasing the cathode current is a valid method to reduce the overall quantity of defect, the droplet dimensional distribution instead remains inaltered. The multilayer architecture resulted to be the most dense and compact among the three coatings from the observation of the fractured cross section surfaces. Mechanical properties measured through nano indentations confirmed that the multilayer architecture is also the hardest (26 GPa) and has the highest elastic modulus (384 GPa). The developed coating showed good scratch resistance and adhesion, at 4000 mN debris from the scratch track evidence a progressive frantumation of the top – layer of the multilayer coating while for the monolayer thicker and solid portions of coating detached. In the future works the properties of the multilayer and monolayer coating will be tested on cutting tools so as to demonstrate the actual benefits of the multilayer in the specific application for which it was designed.

# References


1. *Modal Filter for a Disk and Its Application to the evaluation of the Tensioning Effect on Circular Saw.* **Kuratani, F.** 2011, Journal of System Design and Dynamics, p. 332 - 343.
2. *North American techniques for circular saw tensioning and leveling: practical measurement.* **Schajer, G. S.** 1992, Holz als Roh- und Werkstoff, p. 111 - 116.
3. *Tool wear mechanism of WC–5TiC–10Co ultrafine cemented carbide during AISI 1045 carbon steel cutting process.* **Guo, Zhixing.** 2012, International Journal of Refractory Metals and Hard Materials, p. 262 - 269.
4. **Astakhov, Viktor P.** *Tribology of Metal Cutting* . s.l. : Springer , 2006.
5. **Santochi, G.** *Tecnologia meccanica e studi di progettazione.* Milano : Casa Editrice Ambrosiana, 2000.
6. **Davis, R.** *ASM Metal handbook Vol 16. Machining Processes.* Materials Park, OH : ASM International, 1989.
7. **Evers, D.** *Interrupted Turning: innovations in turning toolingcombat the challenges in interrupted turning.* Toronto : Canadian industrial machinery, 2009.
8. *A comparison of the performance and wear characteristic of HSS saw blades machining Nimonic PK31, AISI O1 Tool Steel, Inconel 600 and AISI 1018 Carbon Steel.* **Bradbury, S.** 2000, Journal of Materials Science, p. 1511 - 1524.
9. **Sandvik.** www.sandvik.com. [Online] [Riportato: 02 02 2018.] http://www2.sandvik.com/sandvik/0130/HI/SE03411.nsf/88c2e87d81e31fe5c1256ae80035acba/651f6e334db04c46c125707600562c88/$FILE/Cemented%20Carbide.pdf.
10. *Application of Fine Grained Tungsten Carbide Based.* **Prakash, L. J.** 1995, Journal of refractory metals and hard materials, p. 257 - 264.
11. *Properties of Cemented Carbides – An Overview.* **Raihanuzzaman, R.** 2014, Powder Technology.
12. *Effect of cubic carbide composition and sintering parameters on the formation of wear resistant surfaces on cemented carbides.* **Garcia, J.** 2013, International Journal of Refractory Metals and Hard Materials, p. 66 - 71.
13. **Huang.** *US 2006/0225553 A1* USA, 2006.
14. *Powder power.* **Johnson, J. L.** 2008, Cutting tool engineering magazine, p. 60 - 70.
15. *Effect of TaC and TiC on the friction and dry sliding wear of WC–6 wt.% Co cemented carbides against steel counterfaces.* **Merwe, R. v. d.** 2013, International Journal of Refractory Metals and Hard Materials, p. 94 - 102.
16. **Ndlovu, Siphilisiwe.** *The Wear Properties of Tungsten Carbide-Cobalt Hardmetals from the Nanoscale up to the Macroscopic Scale.* Erlangen : Der Technischen Fakultät der Universität Erlangen-Nürnberg zur Erlangung des Grades, 2009.
17. *A study of the Co-W-C system at liquidus temperatures5 (1976) 49-56.* **B. Uhrenius.** 1976, Scandanavian Journal of Metallurgy, p. 49 - 56.

18. *deformation and Compressive fracture in WC materials* . **Rowcliffe, D. J.** 1988, Materials Science and Engineering A, p. 299 - 303.
19. *Abrasion resistance of nanostructured and conventional cemented carbides, Wear 200 (1996) 206-214.* **K.Jia.** 1996, Wear, p. 206 - 214.
20. *Tribological Characteristics of WC-Ni and WC-Co Cemented Carbide in Dry Reciprocating Sliding Contact.* **Bonny, K.** 2009, Tribology transactions, p. 481 - 491.
21. *An overview of the machinability of aeroengine alloys.* **Ezugwu, E.** 2003, Journal of Materials Processing Technology, p. 233 - 253.
22. *Performance studies of multilayer hard surface coatings (TiN/TiCN/Al2O3/TiN) of indexable carbide inserts in hard machining: Part-II (RSM, grey relational and techno economical approach).* **Sahoo, A. K.** 2013, Measurement, p. 2868 - 2884.
23. *Performance studies of multilayer hard surface coatings (TiN/TiCN/Al2O3/TiN) of indexable carbide inserts in hard machining: Part-I (An experimental approach).* **Sahoo, A.K.** 2013, Measurement, p. 2854 - 2867.
24. *Cemented carbide phase diagrams: A review.* **Fernenades, C.** 2011, International Journal of Refractory Metals and Hard Materials, p. 405 - 418.
25. *Fracture Toughness Evaluation of WC-Co Alloys by indentation test.* **Spiegler, R.** 1990, JOURNAL OF HARD MATERIALS, p. 147 - 158.
26. *New results on the relationship between hardness and fracture toughness of WCCo hardmetal.* **O'Quicgley, D.** 1996, Materials Science and Engineering A, p. 228 - 230.
27. **Roebuck, B.** *Mechanical Tests for Hardmetals.* Teddington : National Physical Laboratory, 2009.
28. **Brookes, K. J.** *World directory and Handbook of Hardmetals and hard materials.* s.l. : INternational Carbide data, 1975.
29. *A review of parameters influencing some mechanical properties of tungsten carbide cobalt alloys.* **Exner, H.E.** 1970, Powder Metallurgy, p. 13 - 31.
30. *Intercarbide surface is the main obstacle to increase fracture toughness and strength of hardmetals.* **Laptev, J.V.** Paris : Les Editions de Physique, Les Ulis, France , 1994. Powder Metallurgy World Congress. p. 103 106.
31. *Friction and wear behaviour of cemented* . **Pirso, J.** 2004, Wear, p. 257 - 265.
32. *Tribofilm formation on cemented carbides in dry sliding conformal contact.* **Engqvist, H.** 2000, Wear, p. 219 - 228.
33. *Friction and dry sliding wear behaviour of cermets.* **Priso, J.** 2006, Wear, p. 815 - 824.
34. *Sliding wear of conventional and nanostructured cemented carbides.* **Jia, K.** 1997, Wear, p. 310 - 318.
35. *Abrasion of cemented carbides by small grits.* **Engqvist, H.** 1999, Tribology International, p. 527 - 534.
36. **Engqvist, H.** *Microstructural aspects on wear of cemented carbides. Ph.D. thesis.* Uppsala University, Sweden : s.n., 2000.
37. *Wear mechanisms in abrasion and erosion of WC/Co and related hardmetals.* **Gee, M.G.** 2007, Wear, p. 137 - 148.

38. *Effect of interfacial characteristics on toughness of nanocrystalline cemented carbides.* **Song, X.** 2013, Acta Materialia, p. 2154 - 2162.
39. *Coatings tribology – contact mechanisms and surface design.* **Holmberg, k.** 1998, Tribology International, p. 107 - 120.
40. *Single layer and multilayer wear resistant coatings of (Ti,Al)N: A review.* **PalDey, S.** 2003, Materials Science and Engineering, p. 58 - 79.
41. ***Jehn, H. A.*** *1999, Surface and Coatings Technology, p. 103 - 107.*
42. ***Bunshah, R. F.*** *Handbook of Deposition Technologies for films and coatings. Park Ridge, New Jersey, U.S.A : Noyes Publications, 1994.*
43. ***Boxman, R.*** *Handbook of Vacuum Arc Science and Technology: Fundamentals and Applications. s.l. : Noyes Publications, 1995.*
44. ***D. Mattox, The Fondation of Vacuum Coatings Technology.*** *The Fondation of Vacuum Coatings Technology. s.l. : New Jersey, 2003.*
45. ***Binner, J.G.P.*** *Advanced Ceramic Processing and Technology. New Jersey : William Andrew Publishing/Noyes, 1990.*
46. ***Thorton, J.*** *1974, Journal of Vacuum Science Technology, p. 666 - 702.*
47. ***Musil, J.*** *2000, Surface and Coatings Technology, p. 322 330.*
48. ***Callister, W.D.*** *Fundamentals of Materials Science and Engineering.*
49. ***Rhode, S.*** *Sputter Deposition in Advance Surface Coatings, A Handbook of Surface Engineering. New York : Chapman and Hall , 2001.*
50. ***Cekadaa, M.*** *2008, Vacuum, p. 252 - 256.*
51. ***Mitterer, C.*** *1997, Surface and coating technology, p. 223 - 230.*
52. ***Chen, R.*** *2011, Surface and CoatingsTechnology, p. 5228-5234.*
53. ***Vyskoil, J.*** *1990, Surface and Coatings Technology, p. 299 - 311.*
54. ***Galvan, D.*** *2006, Surface and Coating Technology, p. 590-598.*
55. ***Callister, W. D.*** *Materials Science and Engineering. Danvers, MA : John Wiley & Sons, Inc., 2007.*
56. ***Y., Sung.*** *2005, Thin Solid Films , p. 348 - 353.*
57. ***Chapman, B.*** *Glow Discharge Processes. s.l. : ,John Wiley and Sons, 1990.*
58. ***Munz, W.*** *1997, Vacuum, p. 473 - 481.*
59. ***I.Petrov.*** *1997, Thin solid films, p. 299 - 311.*
60. ***Lugscheider, E.*** *2002, Thin Solid Films, p. 318 - 323.*
61. ***Teixeira, V.*** *2001, Thin Solid Films, p. 276-281.*
62. *Influence of Eta-Phase on Wear Behavior of WC-Co Carbides.* ***Formisano, A.*** *2016, Advances in tribology.*
63. *Fracture toughness of cemented carbides: Testing method and microstructural effects.* ***Sheik, S.*** *2015, International Journal of Refractory Metals and Hard Materials, p. 153 - 160.*
64. *ImageJ2: ImageJ for the next generation of scientific image data.* ***Rueden, C.*** *2017, BMC Bioinformatics, p. 18 - 529.*
65. *Modeling Sawing of Metal Tubes Through FEM Simulation.* ***Bort, C.M.*** *2011. The 14th International ESAFORM Conference on Material Forming AIP Conf. Proc. p. 651-656.*
66. ***DEFORM, V11.*** *Scientific forming. DEFORM v. 11.*

*67. Mechanical properties of multilayer TiAlN/CrN coatings deposited by cathodic arc evaporation.* ***Warcholinski, B.*** *2011, Surface Engineering, p. 491 - 497.*

*68. Reducing the macroparticle content of cathodic arc evaporated TiN coatings.* ***S.G.Harris.*** *2004, Surface and Coatings Technology, p. 283 - 294.*

*69.* ***Moa, J.L.*** *2007, Wear, p. 1423 - 1429.*

*70. An improved technique for determining hardness and elastic modulus using load and displacement sensing indentation experiments.* ***W.C. Oliver, G.M. Pharr,.*** *1992, Journal of Material Research, p. 1564 - 1583.*

*71. Development of PVD coatings for the field of Al alloys forming from liquid state.* ***Lorusso, M.*** *2013, PhD Thesis, p. Torino, February 2013.*

*72. Reading in preparation for writing a PhD thesis: Case studies of experiences.* ***Kwan, Becky S.C.*** *2009, Journal of English for Academic Purposes, p. pages 180-191.*

*73.* ***Bunton, D.*** *Generic moves in PhD thesis introductions. [aut. libro] J. Flowerdew. Academic discourse. London : Pearson Education Limited, 2002, p. 57-75.*

*74. Hardmetals — Palmqvist toughness test.* ***28079-2009, ISO.***